Modeling and Measurement of the Cosmic Muon Flux at Underground Sites

Evan T. Guarnaccia

Dissertation submitted to the Faculty of the
Virginia Polytechnic Institute and State University
in partial fulfillment of the requirements for the degree of

Doctor of Philosophy
in
Physics

Camillo Mariani, Chair
Jonathan M. Link
Patrick Huber
Eric Sharpe

June 17, 2014
Blacksburg, Virginia

Modeling and Measurement of the Cosmic Muon Flux at Underground Sites

Evan T. Guarnaccia

(ABSTRACT)

Modeling the Cosmic Muon Flux is very important for quantifying the backgrounds present for underground experiments. We measure the flux at various locations in the Kimballton Underground Research Facility (KURF) and compare these measurements with our model.

To Juthika
and
To my Family

Acknowledgments

The journey to this PhD has been both very difficult and very rewarding and I owe thanks to many people. I would first like to thank Dr. Jonathan Link for taking me as his student. He started me on the project that would ultimately comprise a significant part of the analysis in this dissertation and he connected me with the people that would ultimately help me get it done. Since he joined the Physics Department at Virginia Tech during my fourth year, Dr. Camillo Mariani has worked very hard to help me achieve my goals. I will always be grateful to him for his kind attention to my needs and for his reassuring manner. I would also like to thank Dr. Leonidas Kalousis for his time, patience, for taking his time to answer my questions, and for frequently checking on me to see if everything was ok. I would also like to thank the other members of my committee, Dr. Eric Sharpe and Dr. Patrick Huber, for their support during my time at Virginia Tech. Thanks to Dr. Linda Olafsen and Dr. Jeff Olafsen for their support. Thanks to Dr. Chang Kee Jung for his support. Thanks to Dr. Danny Marfatia for his support. Thanks to Betty Wilkins for her efforts and for always being willing and available to help. Thanks to Dr. Bruce Vogelaar for his support and guidance. Thanks to Dr. Royce Zia for his support. Special thanks to Dr. Beate Schmittmann for kindly letting me use her office to tutor my students.

Sadly, Chris Thomas passed away the day before I defended my dissertation. Although she will never read these lines, she knew how much her caring and support meant to me from the day she first called me to tell me that my application was accepted by the Physics Department to the day I told her that I would be graduating in 2014. She always reminded me to focus on the job that I know needs to be done and not to worry about what others are thinking. I thank her from the bottom of my heart and I would not have made it if it weren't for her.

I owe a great deal to my family for their support and encouragement throughout the years. My father has always wanted the best for me and has never wavered in his quest to do everything he could to help make that happen. No matter how much I resisted, he never stopped believing that I could achieve things that even I never dreamed were possible. He understands what it takes to be successful and I am so lucky to have him as an example to follow. I can never thank him enough for his guidance and support. The thanks that I owe my mother and the sincere gratitude I have for her and her ways can never be overstated. She has been the wind in my sails and no matter where it seemed my life was heading she

never stopped supporting me and always encouraged me believing that I could realize the potential that she saw in the eyes of her baby boy. I also owe a great deal of thanks to Elizabeth Guarnaccia and Charlie LoParrino. Since they became part of my family over a decade ago, they have been an invaluable source of support, friendship, and love for all of us. I want to thank my sister, Kristy. She has always been a source of laughter and fun and I cannot thank her enough for all of the memorable times through the years. Special thanks to Heidi Ruggiero for her kind love and support. Thanks to Frank Naccari and his family for being a second family to me through the years. I also dedicate this dissertation to my grandparents Mafalda and Matthew, and Josephine and Vincent. They made my parents who they are and also helped shape the person I have become. I thank my cousins, uncles and aunts for all of the support and kindness they have shown me. Thanks to Uncle Matt and Aunt Rina for their support and especially for the golf clubs. My sincere thanks to the Morris family: Aunt Lucille, Uncle Dan, Mitch and Lauren. You all have always been there for me and my family with love and support and you will always have a special place in my heart. Special thanks to my Aunt Joan. She had an inner light as bright or perhaps brighter than anyone I've ever known. I would not be the person I am today without her.

There are so many friends that I would like to thank who have helped in some way and have brought joy to my life in their own unique way during my journey to this PhD. Thanks to Dyanis Popova and Greg Guilman for being my first friends in Blacksburg. Thanks to Jere Brunson, Winston Mathews, Mike Bordens and Rudy Walters Jr. for so many great times. Thanks to Jamie Tsai for some great golf memories. Thanks to Nate Chapman and Dave Plaxco for all the fun. Thanks to Dr. Debabrata Mohapatra and Dr. Manpreet Kaur for their frienship, support, and encouragement. Thanks to Dr. Chun-Min Jen for her friendship and support. Thanks to Moataz Bellah Khalifa for his friendship and encouragement. Thanks to Dr. Yao Zhang and Wenchun Wu for their hospitality and for introducing me to other friends. Thanks to Dr. Adam Bowman for many fun times. Thanks to Dr. Renzun Zhao and his family for their kind hospitality and for great times past and future. Thanks to Swapnil Jawkar and Aaron Dalton for their invaluable help with my thesis. Thanks to Dr. Devdeep Sarkar and Dr. Sriharsha Pothapragada for many memorable times. Thanks to Dr. Ting Lung for visiting me in Blacksburg. Thanks to Dr. Constantinos Constantinou for his friendship. Thanks to Dr. Ting Yan, Dr. Jixia Dai, and Dr. Lisa Winter for all of their support and for many fun times. Thanks to Dr. Bithika Khargharia and Dr. Amarpreet Chawla for all of their support and encouragement. Thanks to Shantanu Dikshit and Priyanka Saxena for the great memories. Thanks to Carolyn Weeramantry for her friendship. Thanks to Mitchell Kaufman for his friendship and support. Thanks to Shahir Mowlaei for his kind friendship and understanding. Thanks to Claire Lee, Eric Christensen, Filiz Keles, and Yasamin Khorramzadeh for the fun memories and for being great classmates. Thanks to Brian Zabrocki for our many billiards adventures. Thanks to Dustin McDonald, Jerry Mitchell, Dewey Wilder, and Wit Tree for so many fun times. Thanks to Dr. Manish Jadhav for his friendship. Thanks to Bryan Redhair for his support, friendship and kindness. Thanks to Nandini Mehta for her friendship and matchmaking skills. Thanks to Sandeep Kakarla for being true blue through and through. Thanks to Dipen Shah for fun times

and for his hospitality. Thanks to Dr. Bharath Prithiviraj and Dr. Anjali Krishnan for their friendship, hospitality, and amazing kindness. Thanks to John Chuba, Greg Gunther, and Patrick Murray for so many great times. Thanks to Matt Bubelnik for his friendship. Thanks to John Yonehara for his friendship and support. Thanks to Jiann Lee for taking me skydiving. Thanks to Munjal Subodh for his friendship. Thanks to Yusuke Wada for being the best roommate. Thanks to Jean Skarke for her friendship and for visiting me along the way. Thanks to Melanie Kann for her contagious energy and encouragement. Thanks to Jody Folster for her support and friendship. Thanks to Alfredo Aguilar and Rashed Al-Abdulghafoor for their business and friendship. Thanks to Jack Barringer and Kyle Mack for the fun memories. A big thanks to all of my many students who supported me through the years. Thanks to Li Gui and Wenjia Liu for the fun memories. Thanks to Erika Hanson and Ryan Aberle for many great times. Thanks to Tom and Tia Van Scoyoc for their friendship and for being there for my thesis defense. Thanks to Capt. Kenneth R. Force, USMS for reminding me to play the game. Thanks to my first Physics teacher, Mr. Tom Cleary. Thanks to Dr. Fred Pasqua for believing in me. Thanks to Dr. Benoit Borguet for the many golf memories. Thanks to Joseph Hor for his friendship, hospitality, and for many fun days and nights. Thanks to everyone who I have not mentioned who has supported me through the years. If I missed you here, I will thank you in person.

Special thanks goes to Richard Wong. I met him shortly before I started my journey through the world of Physics and he has been by my side every step of the way. He is perhaps the hardest-working person I know and yet he still found time to visit me and chat with me every week for more than the last 10 years. Every time I visited my home in New York, he always took the time to fix my car, cook special dishes for me, and take me out to one restaurant after another for great late night eating. He has been an endless source of advice and friendship and I can never thank him enough for what he has done for me.

I owe the most thanks to my best friend and partner, Dr. Juthika Khargharia. She was among the first people I met when I started graduate school and she has been a constant source of encouragement, humor, inspiration, and love. Our travels took us far apart through the years and thanks to her hard work and dedication we have made it through our degree programs to finally be together. She is the light of my life and my dream come true. Thanks to her for the amazing memories we have made and continue to make. More than any other, this dissertation is dedicated to her.

Contents

List of Figures

List of Tables

Chapter 1

Introduction

The Standard Model (SM) is a quantum field theory that was developed in the latter part of the 20^{th} century to describe the properties of the known elementary particles and their interactions [10, 11, 12]. Of the four known fundamental forces in nature the SM contains descriptions of the electromagnetic force and the strong and weak nuclear forces, but does not include gravity. While it is known to be incomplete, predictions made by the SM have been consistently verified by experiment to unprecedented levels [13, 14]. The search for physics beyond the SM has captured the interest of researchers for at least the last 30 years. The idea of adding the gravitational interaction to the SM has led to the development of subjects like String Theory [15, 16, 17]. Unfortunately, the relative weakness of the gravitiational coupling compared to those of the other three forces makes testing String Theory predictions notoriously difficult. The unification of the fundamental forces is not the only path to new physics. Dark Matter [18, 19], which is thought to be composed of non-baryonic particles that hold galaxies and galaxy clusters together, and Dark Energy [20, 21], which is a vacuum energy density with a negative pressure thought to be responsible for the accelerating expansion of the Universe, are both outside of the scope of the SM and offer the prospect of being tested with means that are currently available [22, 23, 24, 25]. Perhaps the most accesible path to physics beyond the SM at the present time comes from investigations of phenomena associated with the neutrino sector, namely neutrino oscillation [26], which requires that neutrinos have non-zero masses. This is an effect that is not predicted by the SM. The neutrino sector is relatively easy to probe because of the abundance of neutrinos in nature and the variety of neutrino sources which are readily available.

1.1 Proposal of the Neutrino

The neutrino was proposed to exist in 1930 by Wolfgang Pauli [27] to address the problems associated with the emission of electrons in a nuclear reaction which came to be known as

beta decay.

Beta decay [28] is a process mediated by the weak nuclear force during which a neutron is turned into a proton, and an electron and an electron type antineutrino are spontaneously created and emitted from a nucleus. The opposite process, in which a proton is struck by an antineutrino, turns the proton into a neutron and a positron is released. This process is referred to as inverse beta decay (IBD).

When measurements of the energy of the electron emitted in beta decay were first taken in the 1920's [29], 11 years before the neutrino was proposed by Pauli, scientists were puzzled by the observation of a continuous spectrum of electron energies. Conservation of energy dictated that if only an electron is emitted in beta decay, then its energy should always be equal to the difference in rest mass of a neutron and a proton. They assumed beta decay would be similar to alpha decay in which alpha particles are emitted with very well-defined energies.

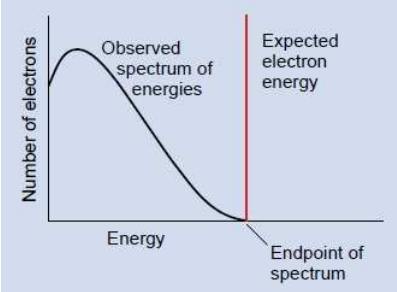

Figure 1.1: A qualitative look at the expected and actual electron energy spectra. Figure from Ref. [1]

Consider the beta decay process

$$n \rightarrow p + e^{-} + \bar{\nu} \tag{1.1}$$

The Q value, which is the energy available for the process, is given by the difference between the rest masses of the initial and final states:

$$Q = (m_n - m_p - m_e - m_{\bar{\nu}})c^2 \tag{1.2}$$

To derive the electron energy spectrum, we start with the number of states for the electron and neutrino, which are given by

$$dn_e = \frac{4\pi p^2 dp V}{h^3} \tag{1.3}$$

$$dn_\nu = \frac{4\pi q^2 dq V}{h^3} \tag{1.4}$$

in the range p to p + dp assuming that there is no dependence on the direction of p or q, making the total number of final states:

$$d^2n = \frac{(4\pi)^2 q^2 dq p^2 dp V^2}{h^6} \tag{1.5}$$

We can absorb all factors that don't depend on p into a constant, C, and the resulting distribution is

$$N(p)dp = Cp^2q^2dp \tag{1.6}$$

where q is given by

$$q = \frac{Q - \sqrt{p^2c^2 + m_e^2c^4} + m_ec^2}{c} \tag{1.7}$$

ultimately giving

$$N(p) = \frac{C}{c^2}p^2\left[Q - \sqrt{p^2c^2 + m_e^2c^4} + m_ec^2\right]^2 \tag{1.8}$$

The predicted spectrum is in good agreement with theory, but it does not account for higher order effects such as coulomb repulsion or a non-zero neutrino mass.

1.2 Discovery of the Neutrino

Neutrino interactions were first conclusively observed in what came to be known as the Reines and Cowan experiment [1, 30]. It was originally conceived of by Fred Reines at Los Alamos Scientific Laboratory in 1951. Reines joined the Manhattan Project at Los Alamos in 1944 as a member of the theoretical division. It was there that many fruitful interactions took place between himself and his colleagues not only about ambitious projects, but also about making use of the physics potential inherent in a nuclear detonation. Reines and his colleagues knew that the weak force mediates interactions in the decay chains of the parent nuclei and that antineutrinos are released and are involved in the changing of an atom's atomic number. Because of this, it seemed appropriate to use an atomic bomb explosion to measure a flux of antineutrinos. Though nobody knew exactly how to build a detector at the time, all agreed that the atomic bomb would be a very promising source of information about neutrinos. In 1951, Reines met Clyde L. Cowan, Jr., who joined the Los Alamos Scientific Laboratory in 1949. Reines managed to interest Cowan in his work, and near the end of 1951, the world's first neutrino experiment, called "Project Poltergeist," was born [31].

The team led by Reines and Cowan decided that the reaction they were looking for was the inverse beta decay process, which turns a proton and an antineutrino into a neutron and a positron. Knowing that a nuclear fission bomb would provide a brief but intense neutrino source, the team set out to design a detector that could be near enough to ground zero to get a reasonable flux without being destroyed by the blast in the process. The detector would be deployed underground to shield it from the atomic blast and outside radiation.

The initial incarnation of the experiment would involve a vertical shaft dug into the ground to a depth of 40 meters. The lower half of the shaft would house an evacuated tube inside which the detector would hang from the top. Since a shock wave accompanies a nuclear blast, the team would have the suspended detector drop from the ceiling of the evacuated tube as the bomb exploded in order to protect the detector and reduce error as much as possible. There would also be foam rubber padding at the bottom of the tube to safely catch the falling detector. Inside the detector would be transparent organic liquid scintillator and photomultiplier tubes[1] on the inner boundaries. Organic scintillator is a liquid which produces small flashes of visible light when irradiated with gamma rays.

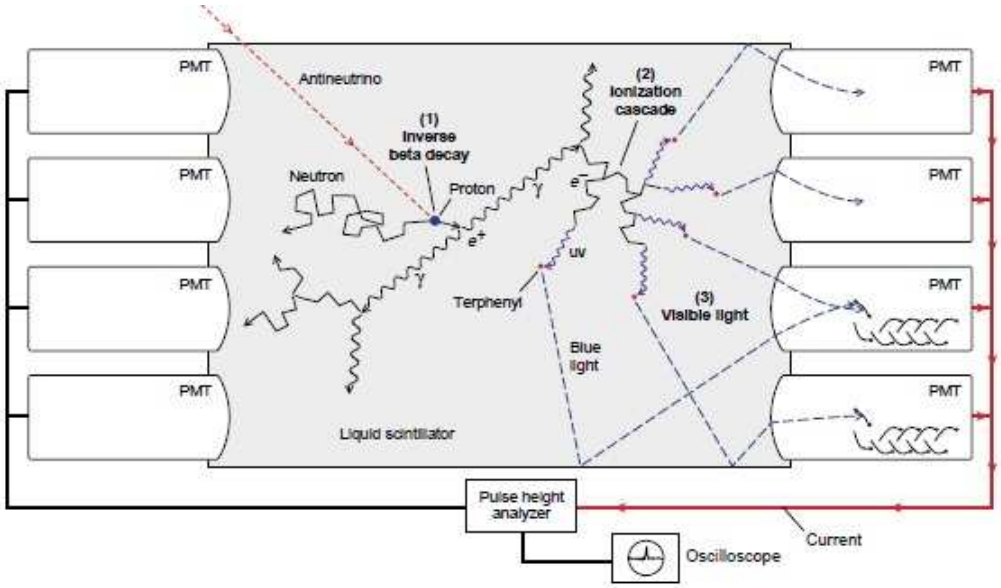

Figure 1.2: A diagram of a detector. Figure from Ref. [1]

Not long after work commenced in late 1952, the project would suddenly take an almost different course entirely. The suggestion of detecting neutrinos emitted by nuclear reactors rather than using a bomb got the attention of the leader of the Physics Division, who in turn strongly influenced Reines and Cowan to take their experiment in this new direction. They would now place a detector undergroud near a nuclear reactor [32], leave it there for extended periods of time, and count the events as they come in. Although the explosion of a bomb would offer a much greater luminosity of neutrinos, the background was found to be roughly the same in both cases, making the nuclear reactor plan the clear choice.

While the orginial plan was to measure only the two gamma rays produced by the electron-positron annihilation, the new detector would also look for the signature of neutron capture. When the neutron is captured by a nucleus, approximately 9 MeV of energy is released, and

[1]Photomultiplier tubes collect light and convert it to an amplified electrical signal that is proportional to the incident number of photons.

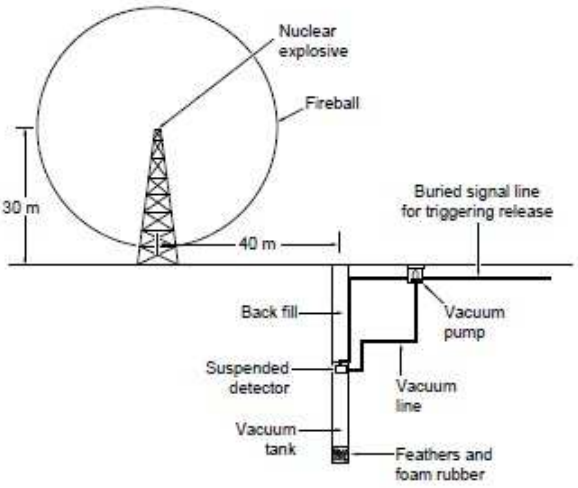

Figure 1.3: The first incarnation of the Reines and Cowan experiment. Figure from Ref. [1]

the timing of this event will be within microseconds of the two prompt gamma rays. To increase the efficiency of detection and reduce neutron capture time, cadmium chloride was added to the organic liquid scintillator, as the cadmium nuclei will readily accept neutrons.

The furious development and testing of the various detector components led the team to realize that they had built a detector of unprecedented sensitivity. This meant not only more precise measurements of the inverse beta decay signal, but also accurate measurements of the radioactivity of the materials surrounding the detector, and even of the detector components themselves, which all together comprise a significant amount of background. Interestingly, a detector was built that had enough room for a human to fit inside, and the natural radioactivity of the ^{40}K in the human body was easily detected. This later found much use for scientists studying the effects of radiation exposure to the human body.

Once the team had finished testing the detector and its components, they headed to Hanford, Washington where the country's newest and biggest nuclear reactor was located. Instead of burying the detector, it was placed inside the reactor building and covered in shielding that was homemade by the experiment team to block outside radiation [33].

They expected an event rate of 0.1-0.3 counts per minute, and tried various combinations of shielding configurations and mixtures of liquid scintillator over the course of months. Unfortunately, the background measured by the detector was about 5 counts per minute, which is significantly higher than the signal rate they expected. This rendered the results of the experiment inconclusive in its present form. It was thought that cosmic rays were providing the majority of the background, and after much testing of the count rate with the reactor on and off, it was determined that cosmic rays were responsible for the background count

rate. Although the count rate was slightly higher with the nuclear ractor on, consistent with predictions, the statistics were still not good enough to confirm the detection of neutrinos.

Having come so close to success, the team set out to completely redesign the experiment in such a way that it would be easier to distinguish a cosmic ray event from a reactor neutrino event [34]. This was accomplished by having a layered setup composed of two target tanks filled with liquid scintillator, and three detector tanks, as shown in Figures 1.4 and 1.5. When an antineutrino interacts with a proton in tank A, for example, the positron that is emitted will annihilate with an electron in the tank and release two .511 MeV photons that travel in opposite directions in he same plane. These photons will not have enough energy to pass through one detector into another, so the adjacent detectors, I and II, will each register a photon with around .5 MeV within 2μs of each other. A cosmic ray passing through the unit would more than likely pass through all three detectors, and in such a case the computer would reject this event. In this way, they can be sure that it is e^-e^+ annihilation rather than other processes with coincidental timing. Once both photons have been detected, the neutron prompt-coincidence circuit will switch on for 30μs allowing the gamma rays from the neutron capture to be observed, although the actual time between the positron and neutron signal is around $3\mu s$. With this more elaborate setup, the team was able to achieve a signal to background ratio of 4:1 which was a great improvement over their last effort.

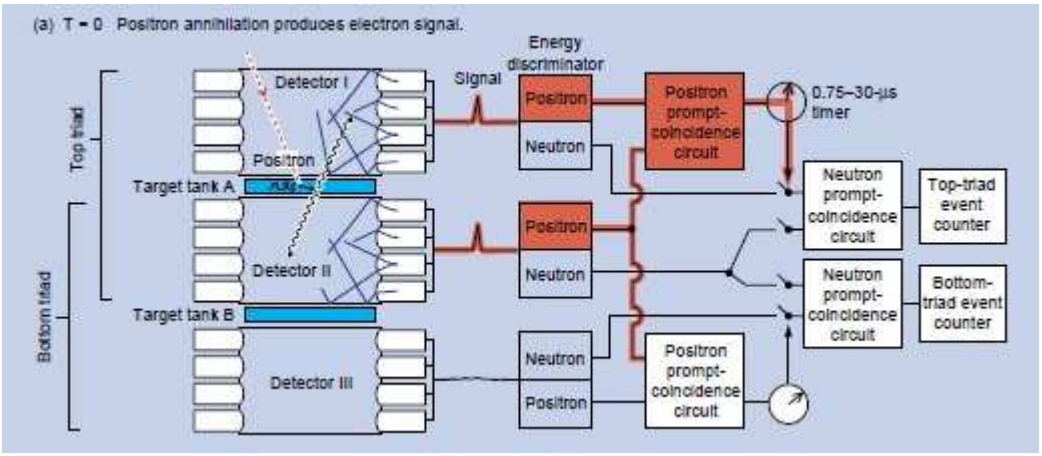

Figure 1.4: The detection of a positron signal. Figure from Ref. [1]

Though everyone working on Project Poltergeist knew that they had finally discovered the signature of the elusive neutrino, they had to perform some internal consistency checks so that there would be no doubt about their result. As a check of their ability to correctly identify a positron signal, they dissolved ^{64}Cu, a known source of positrons, in the water. Knowing that the delay between the positron signal and the neutron capture would be a function of the number of cadmium nuclei present, they doubled the amount of cadmium in the water and looked for a corresponding change in the delay time. The signal should also be proportional to the number of target nuclei, so they took data with a mix of half D_2O and

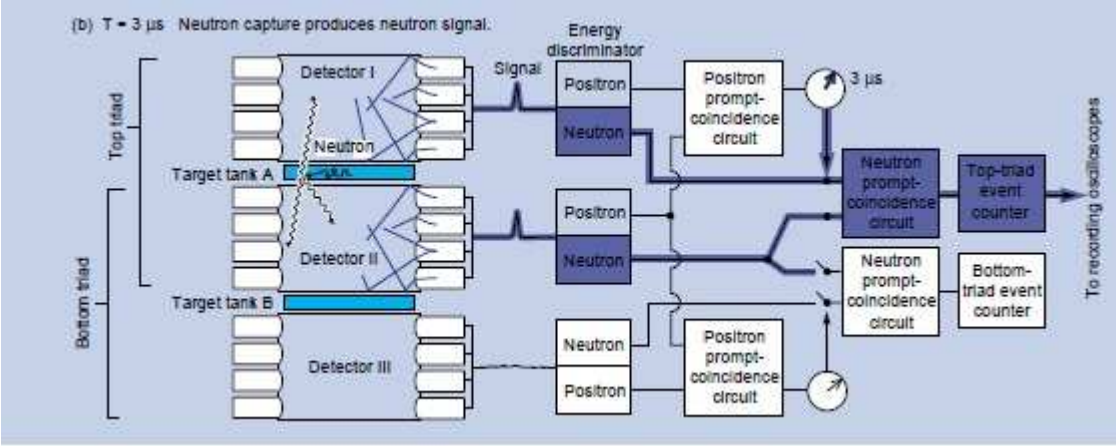

Figure 1.5: The detection of a neutron signal roughly 3μs after detection of a positron signal. Figure from Ref. [1]

H_2O thus reducing the number of isolated proton targets. Their last test was to determine if the signal was due to stray gamma rays and neutrons from the detector. They increased the shielding around the detector and measured a decrease in the rate of accidental reactor events but no decrease in signal.

In the years following the success of the experiment, theorists were hard at work trying to determine the correct predicted cross section for the inverse beta decay reaction. Prediction and experiment were finally in agreement once the parity violation of the weak force was taken into account. Despite the significance of their experiment, it was not until 1995 that the Nobel Prize was awarded [35]. Sadly, Clyde Cowan passed away in 1974, and Fred Reines accepted the award on his behalf.

1.3 Neutrinos in the Standard Model and Beyond

It has been observed [36, 37, 38] that neutrinos (antineutrinos) are always produced in a left-handed (right-handed) state. The experiments by Wu *et al.* and Goldhaber *et al.* proved that the weak nuclear force is parity violating and that the parity violation is nearly maximal. This fact led to a massless chiral neutrino state being introduced into the SM. In the SM the left-handed lepton and left-handed neutrino flavor states form a weak isospin doublet, while the right-handed lepton states are isospin singlets with no corresponding right-handed neutrino state. Similarly, right-handed antilepton and right-handed antineutrino states form a weak isospin doublet, while the left-handed antilepton states are isospin singlets with no corresponding left-handed antineutrino state. Charged leptons and neutrinos are assigned a lepton number $L = 1$ while charged antileptons and antineutrinos are assigned a lepton

number $L = -1$. The SM assumes that neutrinos are massless and do not oscillate and thus that lepton number is conserved in the weak interaction.

Experiments conducted by Ray Davis, Jr. [39, 40, 41] at the Homestake Mine in Lead, SD showed a deficit of solar neutrinos and gave the first hint that neutrinos oscillate. Tanks of carbon tetrachloride were used to detect the $^{37}\mathrm{Cl} + \nu_e \rightarrow \mathrm{e}^- + ^{37}\mathrm{Ar}$ reaction in which a neutrino turns a neutron into a proton through the exchange of a W^- and an electron is released. This experiment was only sensitive to electron neutrinos because of the energetics involved in the reaction. Electron neutrinos produced by the sun have energies around 1 MeV which can produce real electrons after exchanging a virtual W^- with a neutron. Muon or tau neutrinos from the sun resulting from the oscillation of electron neutrinos will not have enough energy to produce real muons or tauons. The results of these experiments suggest that neutrinos oscillate and thus have non-zero masses and that the masses must be different, as will be shown in the following sections.

Experiments that can resolve the small masses of the neutrinos are beginning [42], which use the endpoint of the beta decay spectrum, but cosmological observations have put an upper bound on the sum of the masses of the neutrino states [43]. Combining supernova type Ia (SNIa) data, cosmic microwave backround (CMB), and the Lyman-α forest have yielded an upper bound on the sum of the neutrino masses which is less than 1 eV.

1.4 Neutrinos Come in Different Flavors

Beams of neutrinos can be produced by particle accelerators and these neutrinos can reach energies in the GeV range. It was shown that neutrinos of different flavors are distinct from one another using a proton beam from the Brookhaven AGS in the early 60s [44]. This experiment confirmed the existence of the muon neutrino and the 1988 Nobel Prize in Physics was shared by Leon Lederman, Melvin Schwartz and Jack Steinberger.

The proton beam produced by the AGS had an energy of 15 GeV and was directed to strike a Beryllium target to ultimately produce a beam of muon neutrinos. Beryllium was chosen because protons will lose less energy before interacting in targets with low Z. Pions are produced when the protons interact with the target nuclei. Pions, which are the lightest mesons, are composed of two quarks and come in three varieties: π^0, π^+, and π^-. They are made up of only up and down quarks and are commonly produced in hadronic interactions. The π^0 is a superposition of two states since a neutral meson can be made with $u\bar{u}$ or $d\bar{d}$ and is written as $\frac{1}{\sqrt{2}}(u\bar{u} - d\bar{d})$. The quark contents of the π^+, and π^- are $u\bar{d}$ and $\bar{u}d$, respectively. Charged pions decay through the weak interaction into muons and muon neutrinos much more often than into electrons and electron neutrinos. At first glance, this seems counterintuitive since more phase space is available if the pion decays to e and ν_e. An interesting effect known as helicity suppression[2] makes charged pions decay into μ and ν_μ

[2]In the ultra relativistic limit only left handed chiral particle states and right handed chiral antiparticle

approximately 1,000 times more often than to e and ν_e and thus makes a beam of purely muon neutrinos relatively easy to produce.

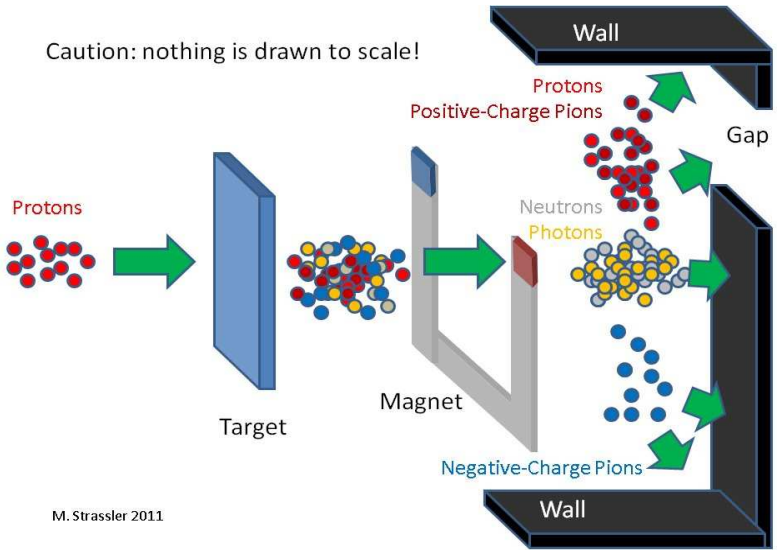

Figure 1.6: How to make a beam of muon neutrinos. The pions produced in this process decay into muons and muon neutrinos. The muons will be stopped by shielding and the neutrinos will continue on. To get an antineutrino beam, the polarity of the magnet is reversed. Figure from Ref. [2]

Knowing that pion decay produces mostly muon neutrinos and that neutrinos have very small interaction cross sections, a detector placed behind the shield that absorbed the protons and pions should only record signal events in which a muon is created in the detector through a weak interaction involving the muon neutrino. This was what indeed happened, and the cross section of the interaction was in agreement with the SM prediction, and thus the muon neutrino was discovered.

---

states participate in the weak interaction because of its parity violating V-A structure. Pions have spin 0 and thus, in the rest frame of the pion, the leptons into which it decays must have opposite spins. In the case of $\pi^- \to \bar{\nu_\mu} + \mu^-$ in the rest frame of the pion, the antineutrino will have a right handed helicity and so will the muon to conserve angular momentum. This is allowed because the muon has non-zero mass and thus its right handed helicity state has a small, but non-zero, left handed chiral component. A right handed helicity state, for example, can be written as the sum of left handed chiral and right handed chiral states. At ultrarelativistic energies the amplitude of the left handed chiral state goes to zero, making helicity and chirality the same in the ultrarelativistic or massless limits. The matrix element for the charged pion decay in the rest frame of the pion becomes propotional to $\frac{m_l}{m_\pi + m_l}$ thus heavily suppressing the decay into an electron.

1.5 Neutrino Oscillation

1.5.1 Two Neutrino Oscillation

Neutrinos are now known to come in 3 active flavors [45, 46] which are defined by the different decay modes of the W boson. The neutrino produced in the decay of a W is always the same flavor as the accompanying lepton. If we assume that neutrinos have non-degenerate masses and that the flavor eigenstates are not the same as the mass eigenstates for neutrinos, we find that it is possible for the flavor of the neutrino to oscillate, which is the case in the quark sector where the strong eigenstates are not the same as the weak eigenstates.

For simplicity, we will derive the oscillation probability assuming that there are just two flavors of neutrinos and that they are related to the two mass states by a unitary transformation

$$\begin{pmatrix}\nu_\alpha\\ \nu_\beta\end{pmatrix} = \begin{pmatrix}\cos\theta & \sin\theta\\ -\sin\theta & \cos\theta\end{pmatrix}\begin{pmatrix}\nu_1\\ \nu_2\end{pmatrix} \tag{1.9}$$

which we can invert to get

$$\begin{pmatrix}\nu_1\\ \nu_2\end{pmatrix} = \begin{pmatrix}\cos\theta & -\sin\theta\\ \sin\theta & \cos\theta\end{pmatrix}\begin{pmatrix}\nu_\alpha\\ \nu_\beta\end{pmatrix} \tag{1.10}$$

Since the mass states are eigenstates of the Hamiltonian, we can express their time evolution in this way

$$\begin{pmatrix}|\nu_1(x,t)>\\ |\nu_2(x,t)>\end{pmatrix} = \begin{pmatrix}e^{-i\phi_1} & 0\\ 0 & e^{-i\phi_2}\end{pmatrix}\begin{pmatrix}|\nu_1(0,0)>\\ |\nu_2(0,0)>\end{pmatrix} \tag{1.11}$$

where $\phi = p\cdot x$. We can then write

$$\begin{pmatrix}|\nu_\alpha(x,t)>\\ |\nu_\beta(x,t)>\end{pmatrix} = \begin{pmatrix}\cos\theta & \sin\theta\\ -\sin\theta & \cos\theta\end{pmatrix}\begin{pmatrix}e^{-i\phi_1} & 0\\ 0 & e^{-i\phi_2}\end{pmatrix}\begin{pmatrix}\cos\theta & -\sin\theta\\ \sin\theta & \cos\theta\end{pmatrix}\begin{pmatrix}|\nu_\alpha(0,0)>\\ |\nu_\beta(0,0)>\end{pmatrix} \tag{1.12}$$

which becomes when the matrix multiplication is carried out

$$\begin{pmatrix}|\nu_\alpha(x,t)>\\ |\nu_\beta(x,t)>\end{pmatrix} = \begin{pmatrix}e^{-i\phi_1}\cos^2\theta + e^{-i\phi_2}\sin^2\theta & \sin\theta\cos\theta(e^{-i\phi_2}-e^{-i\phi_1})\\ \sin\theta\cos\theta(e^{-i\phi_2}-e^{-i\phi_1}) & e^{-i\phi_1}\sin^2\theta + e^{-i\phi_2}\cos^2\theta\end{pmatrix}\begin{pmatrix}|\nu_\alpha(0,0)>\\ |\nu_\beta(0,0)>\end{pmatrix}$$

If we want the proability that a neutrino created in flavor state α is detected in flavor state β somewhere down the line, we find

$$|<\nu_\beta(x,t)|\nu_\alpha(0,0)>|^2 = \sin^2\theta\cos^2\theta|(e^{i\phi_2}-e^{i\phi_1})|^2 \tag{1.13}$$

where the exponents have changed sign because they came from a bra instead of a ket, and we assume that

$$<\nu_\alpha(0,0)|\nu_\alpha(0,0)> = 1 \tag{1.14}$$

and

$$< \nu_\beta(0,0)|\nu_\alpha(0,0) > = 0 \tag{1.15}$$

if we expand the exponential term and use the identities $e^x = \cos x + i\sin x$, $2\sin\theta\cos\theta = \sin 2\theta$, and $2\sin^2\theta = 1 - \cos 2\theta$, the oscillation probability becomes

$$P(\nu_\alpha \to \nu_\beta) = \sin^2(2\theta)\sin^2\left(\frac{\phi_2 - \phi_1}{2}\right) \tag{1.16}$$

where $\phi_2 - \phi_1 = (E_2 - E_1)t - (p_2 - p_1)x$. This can be written as $(E_2 - E_1)L - (p_2 - p_1)L$, where $c = 1$ and L is the distance traveled by the neutrino. If we consider relativistic neutrinos where $E \gg m$, we can write

$$p = \sqrt{E^2 - m^2} = E\sqrt{1 - \frac{m^2}{E^2}} \approx E(1 - \frac{m^2}{2E^2}) \tag{1.17}$$

Plugging this result into our expression for the oscillation probability and assuming both states have the same energy, we get

$$P(\nu_\alpha \to \nu_\beta) = \sin^2(2\theta)\sin^2\left(\frac{\Delta m^2_{21} L}{4E}\right) \tag{1.18}$$

where $\Delta m^2_{21} = m^2_2 - m^2_1$. If we reintroduce factors of c and $\hbar$ and express L in km and E in GeV, we arrive at

$$P(\nu_\alpha \to \nu_\beta) = \sin^2(2\theta)\sin^2\left(1.27\Delta m^2_{21}\frac{L}{E}\right) \tag{1.19}$$

While this formula was derived in the case of two flavor oscillation, it turns out to be very useful in determining the mixing angles in the case of three neutrino oscillations.

1.5.2 Three Neutrino Oscillation

Proceeding in the same way as for the case of two flavor oscillation, we assume that the three neutrino flavors are related to the three mass eigenstates by a unitary transformation.

$$\begin{pmatrix} \nu_e \\ \nu_\mu \\ \nu_\tau \end{pmatrix} = \begin{pmatrix} U_{e1} & U_{e2} & U_{e3} \\ U_{\mu 1} & U_{\mu 2} & U_{\mu 3} \\ U_{\tau 1} & U_{\tau 2} & U_{\tau 3} \end{pmatrix} \begin{pmatrix} \nu_1 \\ \nu_2 \\ \nu_3 \end{pmatrix} \tag{1.20}$$

We can write a unitary matrix in 3 dimensions as the product of three rotation matrices, one for each dimension, as

$$\begin{pmatrix} \nu_e \\ \nu_\mu \\ \nu_\tau \end{pmatrix} = \begin{pmatrix} 1 & 0 & 0 \\ 0 & \cos\theta_{23} & \sin\theta_{23} \\ 0 & -\sin\theta_{23} & \cos\theta_{23} \end{pmatrix} \begin{pmatrix} \cos\theta_{13} & 0 & e^{-i\delta_{CP}}\sin\theta_{13} \\ 0 & 1 & 0 \\ -e^{i\delta_{CP}}\sin\theta_{13} & 0 & \cos\theta_{13} \end{pmatrix} \begin{pmatrix} \cos\theta_{12} & \sin\theta_{12} & 0 \\ -\sin\theta_{12} & \cos\theta_{12} & 0 \\ 0 & 0 & 1 \end{pmatrix} \begin{pmatrix} \nu_1 \\ \nu_2 \\ \nu_3 \end{pmatrix}$$

where δ_{CP} is a CP violating phase.

As the matrix algebra is carried out to determine oscillation probabilities, we can make some simplifying assumptions. We can assume that $\delta_{CP} = 0$, that $\Delta m^2_{21} \ll \Delta m^2_{23}$ and that $\Delta m^2_{23} \approx \Delta m^2_{13}$. As in the two flavor oscillation case, the only two parameters of the oscillation probability equation that can be changed to a large degree are L and E_ν. We can find approximate expressions for the oscillation probabilities for two cases, small and large $\frac{L}{E}$. Small values of $\frac{L}{E}$ correspond to distances on the order of the diameter of the Earth or less and neutrinos with GeV energies, whereas large values $\frac{L}{E}$ correspond to distances on the order of 1 Astronomical Unit (A.U.), which is the mean distance from the Earth to the Sun, and neutrinos with MeV energies.

When $\frac{L}{E}$ is small, $\sin^2\left(1.27\Delta m^2_{12}\frac{L}{E}\right) \to 0$, and we can write the following oscillation probabilities

$$P(\nu_\mu \to \nu_\tau) = \cos^2(\theta_{13})\sin^2(2\theta_{23})\sin^2\left(1.27\Delta m^2_{23}\frac{L}{E}\right) \tag{1.21}$$

$$P(\nu_e \to \nu_\mu) = \sin^2(2\theta_{13})\sin^2(\theta_{23})\sin^2\left(1.27\Delta m^2_{23}\frac{L}{E}\right) \tag{1.22}$$

$$P(\nu_e \to \nu_\tau) = \sin^2(2\theta_{13})\cos^2(\theta_{23})\sin^2\left(1.27\Delta m^2_{23}\frac{L}{E}\right) \tag{1.23}$$

Assuming that θ_{13} is small, the oscillation probabilities reduce to

$$P(\nu_\mu \to \nu_\tau) = \sin^2(2\theta_{23})\sin^2\left(1.27\Delta m^2_{23}\frac{L}{E}\right) \tag{1.24}$$

$$P(\nu_e \to \nu_\mu) = 0 \tag{1.25}$$

$$P(\nu_e \to \nu_\tau) = 0 \tag{1.26}$$

In the case where $\frac{L}{E}$ is large, we have

$$P(\nu_e \to \nu_{\mu,\tau}) = \cos^2(\theta_{13})\sin^2(2\theta_{12})\sin^2\left(1.27\Delta m^2_{12}\frac{L}{E}\right) + \frac{1}{2}\sin^2(\theta_{13}) \tag{1.27}$$

Assuming again that θ_{13} is small, this reduces to

$$P(\nu_e \to \nu_{\mu,\tau}) = \sin^2(2\theta_{12})\sin^2\left(1.27\Delta m^2_{12}\frac{L}{E}\right) \tag{1.28}$$

Solar neutrinos satisfy the condition that $\frac{L}{E}$

A measurement of θ_{13} can be made with a reactor experiment with $\sim$1 MeV neutrinos and a baseline of approximately 1 km. In this case, the survival probability of ν_e can be approximated as

$$P(\nu_e \to \nu_e) \approx 1 - \sin^2(2\theta_{13})\sin^2\left(1.27\Delta m^2_{23}\frac{L}{E}\right) \tag{1.29}$$

I will show that the θ_{12} mixing angle is associated with the solar neutrino problem, the θ_{23} mixing angle is associated with the atmospheric neutrino problem, and how the θ_{13} sector is associated with reactor neutrinos.

1.5.3 Atmospheric Neutrino Anomaly

Atmospheric neutrinos are produced high in the Earth's atmosphere from the collisions of cosmic rays with particles in the atmosphere [47]. Cosmic rays are known to be made up of mostly protons and helium nuclei of extremely high energies [48]. They originate from some of the most energetic processes in the known Universe, such as: active galactic nuclei, gamma ray bursts, and supernova explosions [49, 50]. Pions and kaons are produced in great number when cosmic rays strike particles in the atmosphere. Cosmic rays are of such high energy that thousands of secondary particles are produced from just one collision. Neutrinos are produced when cosmic muons decay, as well as when pions and kaons decay via weak processes. Interestingly, this leads to the prediction that the number of muon neutrinos produced in the atmosphere is twice the number of electron neutrinos produced. When pions decay, they mostly decay into a muon and a muon antineutrino, and the muon subsequently decays into another muon neutrino, an electron, and an electron neutrino, thus giving the expected approximate 2:1 ratio.

Atmospheric neutrinos have energies in the GeV range and thus can be detected by the Super-Kamiokande [51] (Super-K) experiment located in the Japanese Alps. It is a 50 kton water Čerenkov detector in the shape of a 40 m square cylinder. Čerenkov radiation is emitted whenever a charged particle is moving faster than the speed of light in the medium in which it is moving. It consists of an inner detector and an outer detector and the inner fiducial volume is 22.5 kton of ultrapure water [52]. Before the accident [53] at Super-K in 2001 there were over 11,000 PMTs in the inner detector each with a diameter of 20 inch, and almost 2,000 PMTs in the outer detector each with a diameter of 8 inch. The accident reduced the PMT coverage of the inner detector from 40% to 19%.

Super-K can detect and differentiate between ν_e and ν_μ events [54], but ν_τ events are more difficult to identify. In e-like events the ring pattern made by the Čerenkov light is not as tightly circular as the ring pattern in μ-like events. The reconstructed opening angle of the Čerenkov light is given by

$$\cos\theta = \frac{1}{n\beta} \tag{1.30}$$

where θ is the opening angle, n is the index of refraction of the medium, and β is the speed of the particle relative to the speed of light. It is also used to separate e-like events from μ-like events. τ-like events are difficult to identify because neutrinos with energies high enough to produce τ leptons are rare and because they quickly decay to a variety of final states which include muons, electrons, and pions [55]. These events are typically multi-ring events which decreases the likelihood of identifying the leading lepton. Super-K cannot detect neutral

current (NC) events, which can be initiated by neutrinos of any flavor, since there is no relativistic final state lepton.

Cosmic muons are an important source of background events because they can cause spallations in the material around the detector which are a primary source of background for neutrino events. Cosmic muons that penetrate the inner detector can be identified by coincidences in a sufficient number of PMTs in the outer detector [56]. Cosmic muon induced spallations will be discussed in greater detail in the next chapter.

Since neutrinos can travel vast distances through matter, atmospheric neutrinos can be detected coming from all polar angles. Super-K measured [57] the flux of ν_e to be in agreement with theory over all polar angles and energy ranges from sub-GeV to multi-GeV. The problem was with the flux of ν_μ. Low energy ν_μ events showed a consistent deficit over all polar angles while higher energy ν_μ were in agreement with expectations at small polar angles but showed a significant deviation for muons that traveled through most of the earth before being detected.

These results indicated that atmospheric ν_e apparently do not significantly oscillate, while atmospheric ν_μ oscillate almost exclusively to ν_τ. Thus, we can use Eq.(1.21) to describe these oscillations. A typical energy for atmospheric neutrinos is 1 GeV. Neutrinos coming to the detector from the zenith have a baseline of about 15 km. Using an approximate value of $\Delta m^2_{23} = 1{\times}10^{-3}$, the oscillation probability becomes negligibly small. In the case of upward travelling atmospheric ν_μ, we have a typical energy of 1 GeV with a baseline of about 13,000 km. With these values $\sin^2\left(1.27\Delta m^2_{23}\frac{L}{E}\right)$ oscillates very rapidly and this factor will average out to 0.5. The oscillation probability for upward going ν_μ can be approximated as

$$P(\nu_\mu \rightarrow \nu_\tau) \approx 0.5 \sin^2(2\theta_{23}) \tag{1.31}$$

Since the deficit of upward going ν_μ is approximately 50%, this suggests a maximal mixing angle. Super-K reported best fit values[58] $\Delta m^2_{23} = 2.5{\times}10^{-3} eV^2$ and $\sin^2(2\theta_{23}) = 1.00$.

These results were confirmed by T2K [59] recently which made use of a ν_μ beam from J-PARC aimed at the Super-K detector but off axis[3] by 2.5°. T2K was looking for the disappearance of ν_μ and obtained results in agreement with the Super-K atmospheric data with best fit results of $\Delta m^2_{23} = 2.51{\pm}0.10{\times}10^{-3} eV^2$ and $\sin^2(\theta_{23}) = 0.514^{+0.055}_{-0.056}$.

1.5.4 Solar Neutrino Problem

An extremely important source of astrophysical neutrinos is the sun. A process that is known at the pp chain is responsible for the vast majority of neutrino production by the sun [60, 61]. The pp-I reaction contributes around 86% of the total neutrino flux. This process is

$$p + p \rightarrow d + e^+ + \nu_e \tag{1.32}$$

[3]The beam was not aimed directly at Super-K.

where the neutrino energy can be up to .42MeV

$$p + e^- + p \rightarrow d + \nu_e \tag{1.33}$$

where the neutrino energy can be as much as 1.44MeV

$$d + p \rightarrow \gamma + {}^3He \tag{1.34}$$

$${}^3He + {}^3He \rightarrow {}^4He + p + p \tag{1.35}$$

The production of ${}^3He$ in the pp-I chain leads to what is known as the "hep" chain and the pp-II chain. The hep chain is given by:

$${}^3He + p \rightarrow {}^4He + e^+ + \nu_e (\leq 18.77 MeV) \tag{1.36}$$

The pp-II chain is:

$${}^3He + {}^4He \rightarrow {}^7Be + \gamma \tag{1.37}$$

$${}^7Be + e^- \rightarrow {}^7Li + \nu_e (\leq .861 MeV) \tag{1.38}$$

$${}^7Li + p \rightarrow {}^4He + {}^4He \tag{1.39}$$

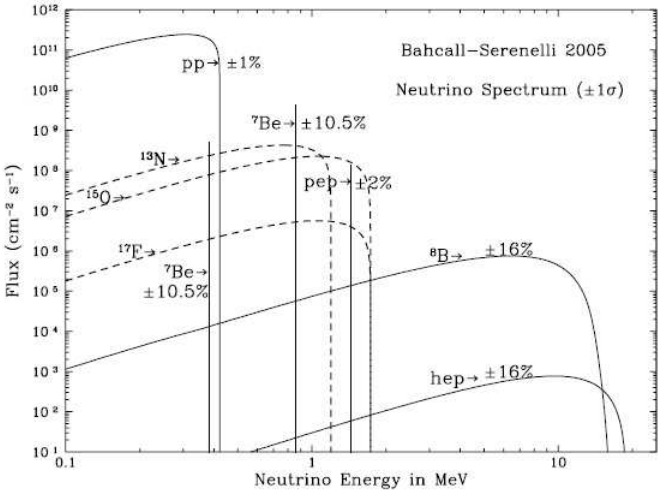

Figure 1.7: Neutrino spectra coming from different processes within the sun. Figure from Ref. [3]

The hep chain contributes a negligible amount to the flux, whereas the pp-II chain is responsible for about 14%. The pp-III chain is:

$${}^7Be + p \rightarrow {}^8B + \gamma \tag{1.40}$$

$$^8B \rightarrow ^8Be^* + e^+ + \nu_e (\leq 14.06 MeV) \tag{1.41}$$

$$^8Be^* \rightarrow ^4He + ^4He \tag{1.42}$$

and it is responsible for a fraction 1.5×10^{-4} of the total flux. Although it contributes only minutely, it is the neutrinos from this process that are detected at Super-Kamiokande because the threshold for detection is approximately 5 MeV. Super-K uses the elastic scattering (ES) channel

$$\nu + e^- \rightarrow \nu + e^- \tag{1.43}$$

to identify neutrino interactions which occurs significantly more often for ν_e than ν_μ and ν_τ because ν_e can interact via the charged current and the neutral current, whereas ν_μ and ν_τ can only scatter off of electrons with a neutral current. It is the final state lepton from the charged current process that produces the Čerenkov light that is picked up by the detector. Super-K uses the ES channel because the directionality of the final state lepton is nearly colinear with the incoming neutrino, aiding in background rejection.

The problem was that the number of ν_e events was significantly lower than what was predicted by Bahcall's widely accepted Standard Solar Model (SSM) [62]. To confirm that the total neutrino flux from the Sun is in agreement with the SSM, an experiment was needed that was sensitive to all three neutrino flavors to demonstrate that the missing ν_μ oscillated to ν_τ. This required being able to detect neutrinos through neutral current (NC) and charged current (CC) interactions. The SNO experiment[63, 64, 65] located near Sudbury, Ontario, Canada was capable of measuring neutrino interactions in multiple channels by using D_20 rather than H_20. SNO is a water Čerenkov detector with a spherical target volume of 10^6 kg of ultrapure D_20 which is contained in an acrylic vessel surrounded by ultrapure light water for shielding and support and the vertical overburden of the detector is approximately 6000 m.w.e.

The channels for neutrino detection at SNO are

$$\nu_e + d \rightarrow p + p + e^- \qquad (CC) \tag{1.44}$$

$$\nu_x + d \rightarrow p + n + \nu_x \qquad (NC) \tag{1.45}$$

$$\nu_x + e^- \rightarrow \nu_x + e^- \qquad (ES) \tag{1.46}$$

where d is a deuteron and ν_x is a neutrino of any flavor.

The CC interaction can only happen with ν_e for solar neutrinos because the neutrino energy is much less than the rest masses of the μ and τ leptons. The e^- produced in the CC and ES interactions emits Čerenkov light which is detected by the PMTs [66]. The protons from this reaction are not identified. The most important detection channel is the NC since all three flavors participate in this interaction. The n produced in the NC interaction gets captured and produces a gamma ray which will compton scatter off an e^- and cause the e^- to emit Čerenkov light with a delay of tens of milliseconds. Background events can come from cosmic muon induced neutrons and can be rejected within a 20 s coincidence time window of the

intial muon. Cosmic muons can also mimic through-going muons produced in CC events that occur outside the detector in which a ν_μ produces a μ through an interaction with the surrounding rock [67]. The total flux of solar neutrinos as measured by SNO was found to be in great agreement with the SSM [68].

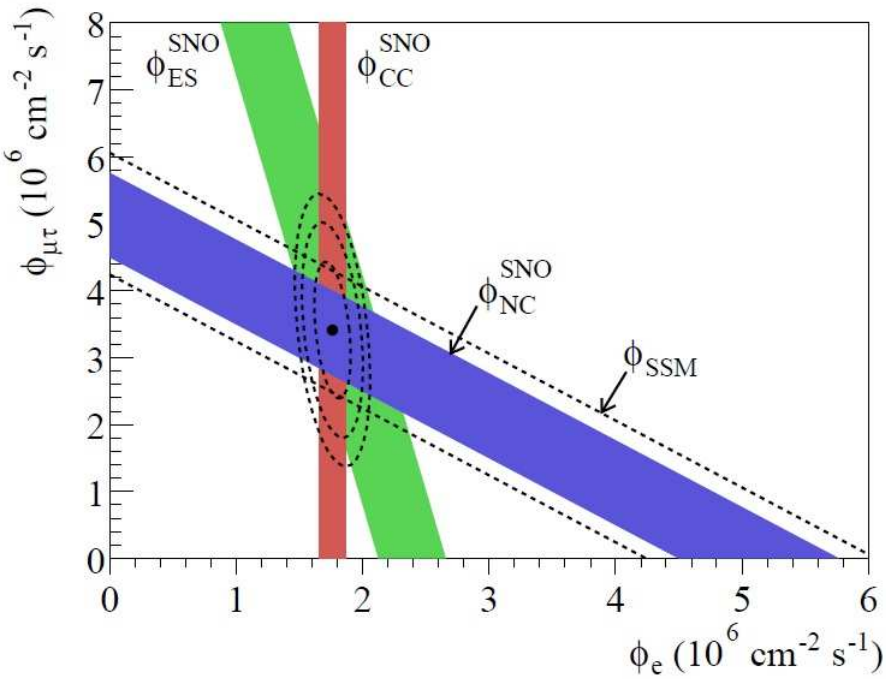

Figure 1.8: Plot of the allowed regions for the neutrino flux for vaious detection channels. Figure from Ref. [4]

In Fig. 1.8 we can see that the flux from the CC channel is independent of the ν_μ and ν_τ fluxes since only ν_e can participate in this interaction. The ES channel has a contribution from the ν_μ and ν_τ fluxes, but the flux from this channel is dominated by ν_e since ν_e can interact with an e^- through W^- and Z exchange while ν_μ and ν_τ can only elastically scatter through Z exchange. We can see that the NC channel is equally sensitive to all 3 flavors and is thus the most important. The allowed region for the neutral current fluxes is in good agreement with the prediction of the SSM.

With a baseline of 10^8 km, a typical neutrino energy of 10 MeV, and a small value of θ_{13} we can use Eq.(1.27) to approximate the oscillation probability of solar neutrinos. Using the measured fluxes of ν_e, ν_μ, and ν_τ events from the SNO experiment in Eq.(1.27) would yield a value of Δm^2 that is too small. This is because the oscillation probability of ν_e changes significantly as they propagate from the core of the sun to its surface. This phenomenon is known as the MSW effect [69, 70], after Mikheyev, Smirnov, and Wolfenstein. The essence of this effect in this case is that as electron neutrinos travel through matter they experience a

potential which is proportional to the energy of the neutrino and the electron density of the medium. The potential experienced by ν_μ and ν_τ as they travel through matter is less than the potential experienced by ν_e because ν_μ and ν_τ cannot participate in CC interactions with electrons. The interaction potential results in an effective Δm^2_m that is equal to the vacuum value of Δm^2 multiplied by a factor proportional to $\Delta V/\Delta m^2$ and an effective mixing angle which becomes

$$\sin(2\theta_m) = \frac{\sin(2\theta)}{\sqrt{(\Delta V/\Delta m^2 - \cos 2\theta)^2 + \sin^2(2\theta)}} \tag{1.47}$$

The value of ΔV is highest in the core of the sun where the probability of oscillation is effectively zero. At some point along the way, the value of $\Delta V/\Delta m^2 = \cos 2\theta$ which makes the probability of oscillation close to 1. It is this effect that causes a portion of ν_e to oscillate to ν_μ while propagating through the Sun. Accounting for the MSW effect, the solar oscillation parameters are measured by Super-K [71] to be $\Delta m^2_{21} = 7.6 \pm 0.2 \times 10^{-5} eV^2$ and $\sin^2(\theta_{12}) = 0.31 \pm 0.01$

This result was confirmed by the KamLAND [72] (Kamioka Liquid AntiNeutrino Detector) collaboration. The KamLAND detector [73] is a liquid scintillator (LS) detector located in the same mine as Super-K but at a different location. It is designed to look at reactor neutrinos from all of the reactors in Japan. The survival probability for reactor neutrinos is given by

$$P(\bar{\nu}_e \to \bar{\nu}_e) \approx 1 - \sin^2(2\theta_{13}) \sin^2\left(1.27\Delta m^2_{23}\frac{L}{E}\right) - \sin^2(2\theta_{12}) \sin^2\left(1.27\Delta m^2_{12}\frac{L}{E}\right) \tag{1.48}$$

where the last term is dominant for the KamLAND baseline. The detector has a spherical target volume filled with liquid scintillator enclosed in a balloon which is 13 m in diameter. Outside of that is a layer of non-scintillating buffer oil which acts like a shield to outside radiation. These are enclosed in a cylindrical WC detector fitted with PMTs that can tag cosmic muons and absorb neutrons and gamma rays from the material surrounding the detector. The experiment required a baseline of about 100 km to be sensitive to a $\Delta m^2_{12} \approx 1 \times 10^{-5} eV^2$ with neutrino energies of around 5 MeV. Assuming that neutrino interactions are invariant under CPT, the disappearance of reactor antineutrinos provides an independent check of the the Super-K solar neutrino results. KamLAND reported best fit values of $\Delta m^2_{12} = 7.9^{-0.5}_{+0.6} \times 10^{-5} eV^2$ and $\tan^2(\theta_{12}) = 0.40^{+0.10}_{-0.07}$ which are in agreement with the results from Super-K.

1.5.5 Reactor Neutrinos

Terrestrial sources of neutrinos include those from the natural radioactivity of rocks, people, and other objects. The biggest sources of terrestrial neutrinos are nuclear fission reactors [74]. The three most common sources of reactor neutrinos are from the fission fragments of ^{235}U, ^{238}U, ^{239}Pu, and ^{241}Pu [74] of which ^{235}U is the most important source for many reactors.

Reactor neutrinos typically have energies less than 10 MeV. The formula derived above for the survival probability of ν_e can be used for $\bar{\nu}_e$ providing that neutrino interactions are invariant under CPT. Reactor experiements are designed to look for the disappearance of $\bar{\nu}_e$.

The Reactor Neutrino Experiment at Daya Bay [75] consists of identical anti-neutrino detectors (ADs) placed at 360 m, 500 m, and 1700 m from three sets of nuclear reactor cores. Each AD is designed tocount the number of neutrino events that lead to inverse beta-decay inside its fiducial volume.

$$\bar{\nu}_e + p \rightarrow n + e^+. \tag{1.49}$$

The Daya Bay experiment [75] consists of 8 identical ADs placed in three seperate water pools that are at various distances from the three sets of nuclear reactor cores. There are two ADs in each of the near pools, and four in the far pool, and each AD has three zones. The central region of an AD is called the target zone [76]. The target zone is filled with Gd-loaded liquid scintillator (Gd-LS) [77], and has the highest density of photomultiplier tubes. The actual target volume has both a height and diameter of 3.2 m and a mass of 20 t. The next layer outward is filled with undoped LS, and is designed to detect photons that accidentally escape the target area. The outermost layer of an AD is filled with mineral oil (MO). The MO does not scintillate, and therefore functions as a shield to any outside radiation. The pools containing the ADs are filled with ultra-pure water with no less than 2.5 m of water surrounding any AD, and the ADs are separated by 1 m.

When an antineutrino enters the active volume of the detector and causes an inverse beta decay (IBD), a neutron and a positron result from the interaction. This positron is quickly thermalized and annihilates upon meeting an e^- and produces a prompt signal of just over 1 MeV. The neutron is then soon absorbed by the Gd-LS producing an $\sim$8 MeV signal that is delayed approximately 30μs from the prompt signal. The timing of the delayed signal is very important, because a larger delay time means that less events can be recorded overall. Adding Gd to the LS greatly reduces the neutron capture time and increases the capture probability. PMTs must be capable of ns time resolution to detect this signal.

Cosmic muon interactions inside and near the detector contribute to the three main sources of background in the Daya Bay experiment [78, 79]. The collision of a cosmic muon with a nucleus can mimic a signal event. The recoil of the protons in the nucleus can mimic the prompt signal and the fast neutron released in the collision can be captured to mimic the delayed signal. Cosmic muons can also produce isotopes such as ^{8}He and ^{9}Li which undergo beta decay followed by the emission of a neutron. The beta decay can mimic the prompt signal, while the cature of the neutron can mimic the delayed signal. Also, neutrons produced from cosmic muons that enter the detector can be captured with the right timing after an accidental prompt signal, due to natural radioactivity, to mimic a signal event.

Precise measurements of baseline distances, as well as accurate counting of events are of

primary importance. To achieve a measurement with the desired sensitivity the measured power level of each core should be known to 2%. Since all ADs are identical, if the baseline distances are known very well, there will be a cancelation of correlated uncertainties when taking the ratio of events from near and far ADs.

Daya Bay [80] recorded deficits of $\bar{\nu}_e$ that dependend on the baseline, confirming that the deficits arose from the oscillations of $\bar{\nu}_e$. They report a measurement of $\sin^2(2\theta_{13}) = 0.089 \pm 0.010$. This result was also obtained by the reactor neutrino experiments RENO [81] and Double Chooz [82].

The Reactor Experiment for Neutrino Oscillation [83] (RENO) is based in South Korea measures the disappearance of $\bar{\nu}_e$ from the nuclear reactor at Yonggwang. Like Daya Bay, RENO uses Gd-loaded liquid scintillator. The experiment consists of two identical 16 ton Gd-LS detectors located at baselines of 290 m and 1.4 km away from the reactor. RENO reported a best fit measurement of $\sin^2(2\theta_{13}) = 0.113 \pm 0.013(stat.) \pm 0.019(syst.)$.

The Double Chooz experiment [84] also uses Gd-loaded liquid scintillator. There is a near detector that is under construction at a baseline of 300 m and a far detector at a baseline of 1050 m from the reactor cores at the Chooz nuclear power plant in France. The far detector has a 10.3 m^3 fiducial volume. Double Chooz reported a best fit measurement of $\sin^2(2\theta_{13}) = 0.086 \pm 0.041(stat.) \pm 0.030(syst.)$.

Chapter 2

Cosmic Rays

One of the important sources of background in most neutrino experiments are cosmic muons [85]. A muon is a charged lepton that is identical to an electron in every way except for three very important differences. It has a mass of 105.7 MeV which makes it approximately 200 times heavier than an electron. It is unstable with a lifetime of approximately 2.2 μs, whereas the electron is known to be stable [86]. Interestingly, the lifetime of the muon is the longest of any unstable elementary particle. Finally, the muon and the muon neutrino form a weak isospin doublet, and the muon does not couple to other active neutrino flavors. This means that in interactions mediated by the weak force the muon only couples to the muon flavor eigenstate of the neutrino sector, whereas the electron only couples to the electron neutrino. Likewise for the tau lepton and the associated tau neutrino [87]. The muon decays into a virtual W and a muon neutrino, and the W decays into an electron and an electron neutrino [88]. The W boson produced in muon decay will always be virtual since the mass of the W boson [89] is approximately 80 GeV and this would violate the conservation of energy in the rest frame of the muon.

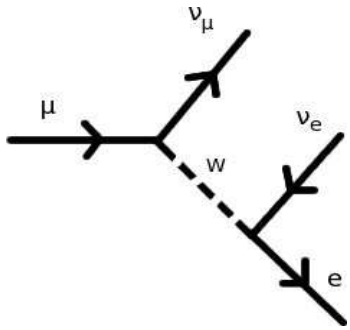

Figure 2.1: Feynman diagram of muon decay.

Muons that are produced through the interactions of cosmic rays with the Earth's atmosphere are known as cosmic muons [9]. In the early 20^{th} century it was discovered that the Earth

is immersed in what can be described as a thin cosmic rain of very high energy particles that have their origins in astrophysical sources, called cosmic rays [90]. They were first discovered by Victor Hess in 1912 [91]. Using a hot air balloon, he brought an electrometer up to an altitude of 5300 m and noticed a four-fold increase in the ionization rate from the rate measured at ground level. To eliminate the sun as the source for the majority of cosmic rays, he duplicated his experiment during a solar eclipse. For this discovery, he was awarded the Nobel Prize in Physics [92] in 1936.

Cosmic rays have been measured to have energies up to 10^{20} eV, but cosmic rays with these energies are rare [93]. This is millions of times higher than the energies attainable at terrestrial particle accelerators such as the LHC. Although there was never much doubt that supernovae are responsible for the production of the majority of primary cosmic rays, this remained unsubstantiated until recently. One major difficulty in locating the point of origin of cosmic rays is that most of them are charged, and thus follow a curved path when passing through magnetic fields.

Cosmic rays can be separated into two categories, primary and secondary [9]. Primary cosmic rays consist of particles produced and accelerated at the astrophysical source. Secondary cosmic rays consist of particles produced as primary cosmic rays encounter interstellar matter along the way.

Primary cosmic rays consist mostly of nuclei that are produced in the normal life cycle of stars which are ejected when the star undergoes a supernova explosion [94]. These include Hydrogen (protons), Helium (alpha particles), Carbon, Oxygen, and others in much less abundance. As shown in Table 2.1 protons make up the majority of primary cosmic ray particles. Secondary cosmic rays consist of elements that are not produced in abundance during stellar life cycles.

One of the mechanisms responsible for the acceleration of primary cosmic rays at their source is known as Diffusive Shock Acceleration [95] (DSA) which is a type of Fermi acceleration. Fermi acceleration [96] is a process through which a charged particle gains energy through repeated magnetic reflection [97]. DSA is a process in which charged particles gain energy through interactions with a magnetic field with moving inhomogeneities, such as within the expanding shock wave created by a supernova explosion. On a basic level, the process is similar to that of a charge inside a magnetic bottle [98]. A magnetic bottle is an arrangement of current loops that produce a magnetic field whose field lines are more dense at the ends of the bottle than they are in the middle. As a charged particle moves inside the bottle it spirals along the field lines due to the lorentz force. As it makes its way to a region of more dense field lines a repulsive force is generated that reflects the charge back to the other side of the bottle where the process is repeated at the other end. In an expanding shock wave a charged particle will gain energy time it repeats this cycle. For this process to begin a particle must have an energy significantly above the thermal energy of the environment of the shock. It is currently not well understood what mechanism is responsible for a significant fraction of particles to attain non-thermal energies and this is known as the *injection problem*. Another

Table 2.1: Relative abundaces of nuclei in primary cosmic rays taking the abundance of ^{8}O to be 1. Table from Ref. [9]

Z	Element	Relative Abundance
1	H	540
2	He	26
3-5	Li-B	0.40
6-8	C-O	2.20
9-10	F-Ne	0.30
11-12	Na-Mg	0.22
13-14	Al-Si	0.19
15-16	P-S	0.03
17-18	Cl-Ar	0.01
19-20	K-Ca	0.02
21-25	Se-Mn	0.05
26-28	Fe-Ni	0.12

critical component of this process is that the shock must be collisionless. Frequent collisions between particles in a shock will tend to thermalize them and thus disallow them from participating in the DSA process. DSA is understood to be a first-order Fermi acceleration in which the energy gained by the particle each time it repeats the reflection process is proportional to β which is the familiar $\frac{v}{c}$. This process continues until the particle has enough energy to escape the magnetic field and propagate freely as a cosmic ray.

It has been recently confirmed by observations of supernova remnants (SNR) that DSA is a mechanism that accelerates primary cosmic rays [99]. The observed gamma ray spectrum from the vicinity of the SNR exhibits a tell-tale feature of pions created by the collision of high energy protons. This is known as the "pion-decay bump" and it roughly follows the energy distribution of the parent protons at energies above a few GeV. High energy protons interacting with the interstellar medium surrounding the SNR produce neutral pions which quickly decay into 2 gamma rays with characteristic energies of 67.5 MeV in the rest frame of the pion. The spectrum becomes smeared when transformed to the lab frame but retains its symmetry with respect to 67.5 MeV when plotting $\frac{dN}{dE}$ vs. E. The characteristic bump is created [5] when the secondary π^0 spectrum is plotted against T_π, which is the kinetic energy of the pion. The observation of the pion-decay bump is complicated by the fact that high-energy electrons can also prouduce gamma rays through inverse compton scattering and bremsstrahlung.

Cosmic rays with energies less than 10 GeV are heavily affected by the solar wind, and to a lesser degree by the geomagnetic field of Earth, and lose much of their energy before reaching Earth [100]. The sun undergoes a cycle of approximately 11 years in which its appearance

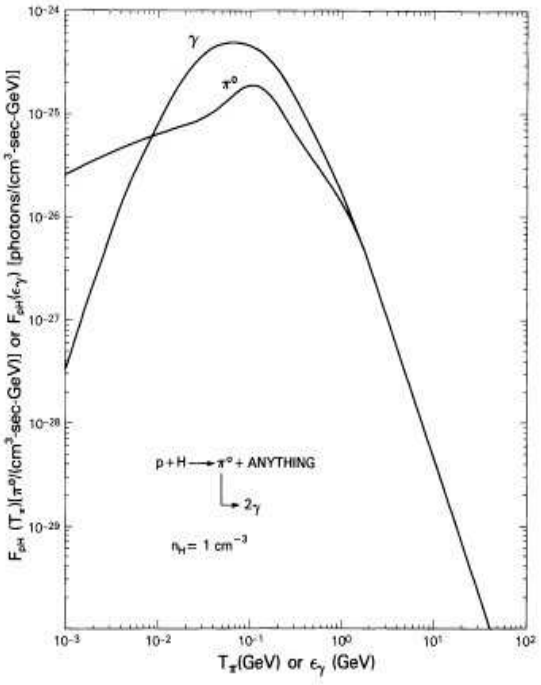

Figure 2.2: Pion flux spectrum showing the pion decay bump. Figure from Ref. [5].

changes and its activity rises and falls [101]. This includes the number of sunspots and also the ejection of plasma into the solar system. A strong anti-correlation between the solar cycle and the number of low energy cosmic rays has been observed, confirming the effect of the solar wind on these rays. Recently, observations made by the Voyager 1 probe [102], which is presently approximately 122 astronomical units (AU) from the sun, also confirm this. An AU is the average distance from the Earth to the Sun, which is approximately 96 million miles. The probe has observed a dramatic increase in the number of low energy cosmic rays as it penetrated a region which is depleted of heliospheric ions on the outskirts of the solar system. Because the magnetic field orientation measured by the probe has not changed direction during its transition into this region, it is not yet thought to be outside of the influence of the sun and into the interstellar medium.

When cosmic rays reach the atmosphere of the Earth they collide with particles in the air and create a shower of particles [103]. A typical scenario is the collision of a cosmic ray proton with a proton in the nucleus of an oxygen atom in the atmosphere. The particles emerging from this collision are mainly protons, neutrons, and mesons such as pions and kaons [104]. As these particles decay they produce muons, electrons, gamma rays, and neutrinos. The decay of charged pions mainly produce muons and anti-muon neutrinos directly. Electrons and positrons are produced when neutral mesons decay into gamma rays which decay through pair production. The particles produced in air showers are very tightly collimated in the direction of the cosmic ray that produced them with deviations of about 1°.

Although the particles in the showers created by cosmic rays are ultra-relativistic, the majority of unstable particles decay before reaching the ground. The exception is the muon, which is the most numerous charged particle from cosmic ray showers to reach the ground. Since high energy muons do not lose a great deal of energy to ionization as they travel through matter, their microsecond lifetime is long enough for them to make it kilometers underground before finally decaying [105], causing a spallation, or being captured by a nucleus.

2.1 Backgrounds in Underground Experiments

Some of the most exciting paths to new Physics have been, and continue to be, explored by experiments located in underground labs all around the world. These include measurements of atmospheric neutrinos [106], accelerator neutrinos [107], proton decay [108], neutrinoless double beta decay [109], and the search for dark matter [110]. These experiments require underground detectors of high sensitivity in order to detect faint signals that would be easily drowned out by cosmic rays and other radiation if they were located on the Earth's surface. Although these experiments vary significanly in their designs and the types of processes they observe, there are sources of backgrounds that are common problems for all of them, such as natural radioactivity in the surrounding rock, radioactive impurities in the components of the detector, activation of detector components due to exposure to radiation, and the interactions with cosmic ray particles in and around the detector. [85]

While cosmic ray showers consist of a wide variety of particles, the majority of them decay or are absorbed before reaching underground detectors, with the exceptions of neutrinos and muons [9]. Cosmic muons can become backgrounds to these experiments either through direct interaction with the detector, or through the production of secondary particles which interact with the detector. Understanding the energy and angular distributions of cosmic muons underground is critical for estimating the number of events that ultimately must be rejected.

Some underground experiments contain muon veto systems [111, 112, 113] with electronics similar to the detector used to collect data for this dissertation, while others can detect the passage of a muon through the detector directly by the Čerenkov and/or scintillation light they generate [114]. Events within the detector that have a time coincidence with the passing of a cosmic muon are rejected. These events are easily identified, but the time window associated with these events is counted as dead time. The dead time from cosmic muons is more of a concern at shallow sites since the rate of cosmic muons is higher there.

The two primary products of muon interactions that become backgrounds for underground experiments are neutrons and unstable isotopes. Neutrons produced underground come primarily from two sources, natural radioactivity in the rock surrounding the detector, and as secondary particles produced by cosmic muon interactions [115, 116]. Although the production of neutrons underground is dominated by natural radioactivity, the spectrum of

neutrons produced by cosmic muon interactions extends to higher energies, up to several GeV.

There are several ways that neutrons are produced by cosmic rays and these include negative muon capture on nuclei [117, 118], electromagnetic showers generated by muons [119], muon interactions with nuclei via the exchange of virtual photons, and quasi-elastic scattering of muons on nuclei [120].

When a muon travelling through matter loses enough energy it may become bound to an atom as an electron would. It quickly cascades down to a 1s orbital where it will either decay in the usual way or it will be captured by the nucleus. The muon capture process is mediated by weak interactions in the same way as electron capture. This rate of this process scales as Z^4 and is therefore much more significant for heavier surrounding material.

Muons can generate electromagnetic showers through bremsstrahlung and pair production [121], which can cause the production of secondary neutrons and unstable isotopes. Since muons primarily lose energy through the production of these showers, this is the dominant mechanism in the production of isotopes. The cross sections of these processes scale as Z^2 and are therefore more important for detectors surrounded by dense rock and detectors with targets made of heavier materials.

Cosmic muons can also generate neutrons produced by spallation in the material surrounding the detector through the exchange of real or virtual photons. Spallation is a process in which a material is struck by a projectile and small pieces of the material are ejected. This term does not originate in particle physics but was borrowed to describe the process of neutron emission by a target struck by accelerated particles. Spallation can also result in the creation of isotopes through a fission reaction in which the cosmic muon causes a larger nucleus to split into smaller nuclei through the exchange of virtual photons with the original nucleus.

The various mechanisms for neutron production through photon exchange are giant dipole resonance (GDR) absorption [122], quasi-deuteron photoabsorption, π-N resonance [123], and deep inelastic scattering. These are in order of increasing energy of the exchanged photon. [85]

GDR is a nuclear excitation in which the entire nucleus is excited into a dipole mode where the protons and neutrons are at opposite ends of the dipole. This excitation occurs for photon energies lower than 30 MeV. The decay of a GDR is primarily through the emission of a neutron.

At photon energies between 40 MeV and 140 MeV the cross section of photon absorption can be approximated by what is known as the quasideuteron model.[124] In this model the cross section is proportional to the photoabsorption cross section of a free deuteron.

At higher energies, above the pion mass of approximately 140 MeV, the exchange of a photon with a nucleon can produce a Δ resonance. A Δ particle is made of up and down quarks and can have a charge of -1, 0, +1, and +2. The 0 and +1 states can be thought of as excited

states of the neutron and proton, respectively. The Δ has a rest mass of 1232 MeV is short lived and the most common decay channels are πN or $\pi\pi$N. Additionally, a π^- produced in this way can be absorbed by a nucleus and release two neutrons through an interaction known as pseudo-deuteron capture. The nucleons involved in this process interact as a deuteron would, although they are part of a heavier nucleus.

$$\pi^- + d \rightarrow n + n \tag{2.1}$$

At energies above the Δ resonance interactions with individual nucleons begin to dominate, such as through quasi-elastic scattering in which a neutron is struck directly by a muon and knocked out of the nucleus.

In a Water Čerenkov (WC) detector, such as Super-Kamiokande (SK), a cosmic muon passing through the detector will produce Čerenkov radiation which is detected by the phototubes that line the walls of the detector. Čerenkov radiation [125] is light emitted by a particle that is travelling faster than the speed of light in a medium. It is produced in a cone shape as the particle propagates and in a detector like SK it is detected as a circular pattern by the phototubes on the wall. The showers created by the passage of the muon are composed mostly of gamma rays which will travel a short distance from the muon track before being absorbed and possibly producing an isotope. The vast majority of the isotopes produced in this way are stable or decay with a low enough energy as to be invisible to the detector. Despite this fact, the relatively small number of unstable isotopes produced in this way still constitute a significant background for the detector. The through-going muon rate at SK is approximately 2 Hz and one out of every 50 isotopes produced by a muon will be unstable. [126] The event rate measured by SK is less than 100 $\frac{events}{day}$ and therefore rejection of events faked by muons is very important. SK detects solar neutrinos from ^{8}B via elastic scattering on an electron after which the electron has enough energy to produce a cone of Čerenkov light. This signal can be mimicked by isotopes produced by cosmic muons interacting with the Oxygen nuclei in the water such as ^{16}N, ^{8}Li, ^{12}B among others. These isotopes most commonly decay through beta decay with lifetimes ranging from 0.02 s for ^{12}Be to 7.13 s for ^{16}N. There are isotopes with shorter lifetimes than ^{12}Be and longer lifetimes than ^{16}N but these isotopes are produced in relatively small numbers compared to the three mentioned above. Since it is still possible for the presence of a muon to be coincident with a neutrino event, a cut is made based on the location of the reconstructed muon track and the point of origin of the suspected neutrino event. Since SK measures neutrinos coming from the sun and cosmic muons mostly come from overhead, an additional cut can be made on events that do not appear to have come from the sun.

The KamLAND detector which is located in the same mine as the SK detector is a liquid scintillator (LS) detector designed to measure electron antineutrinos from nuclear reactors near the experiment site. This detector is also covered with phototubes like SK but is spherical in shape. The detector is surrounded by a layer of buffer oil (BO) to shield the inner detector from radioactivity in the PMT glass and to provide additional shielding from

outside radiation. The channel through which antineutrino events are observed is known as inverse beta decay. This is a process in which an electron antineutrino is captured on a proton and a positron and a neutron are created.

$$\bar{\nu_e} + p \rightarrow e^+ + n \tag{2.2}$$

This interaction gives rise to two signals that can be detected. The first of which is what is known as the prompt signal and it comes from the annihilation of the positron produced in the interaction. The light yield of the prompt signal is proportional to the energy of the antineutrino and the detector is sensitive to antineutrinos with energies above 1.8 MeV [72, 127]. What is known as the delayed signal results from the neutron being captured on a proton, forming a deuteron, and the release of a 2.2 MeV gamma ray, or a capture on a Gd nucleus releasing an 8 MeV gamma ray. The delay time between the prompt and delayed signals is approximately 200 μs with little variation. Muon induced spallation can produce a variety of unstable isotopes that can fake the prompt and/or the delayed signal. These events are identified and cut based on E_{vis} and ΔT, where E_{vis} is the measured light yield computed from the number of photoelectrons (PE) detected and ΔT is the time difference between the detected signal and the passage of the muon. The particular values of E_{vis} and ΔT on which cuts are made depends on the isotope thought to be responsible for the signal. ^{12}Be and ^{12}N undergo β^- and β^+ decay with lifetimes of 29.1 ms and 15.9 ms, respectively, and are identified by 4 MeV $\leq E_{vis} <$ 20 MeV and 2 ms $\leq \Delta T <$ 500 ms. ^{8}He and ^{9}Li both undergo β^- decay with lifetimes of 171.7 ms and 257.2 ms, respectively, but include the emission of a neutron following the β^- decay. These events are identified by using the cuts 1 MeV $\leq E_{vis} <$ 13 MeV and $\Delta T <$ 10 s. In addition, the gamma ray produced by the neutron capture must have originated within 200 cm and 1 ms of the β^- decay. ^{10}C undergoes β^+ decay with a lifetime of 27.8 s and is accompanied by a neutron. These events are identified by the triple coincidence of the cosmic muon, the β^+, and the 2.2 MeV gamma ray from the neutron.

Uncertainties in the muon flux correlate directly to uncertainties in isotope and neutron production and it is therefore important to be able to accurately model the flux of cosmic muons at underground sites.

2.2 Cosmic Muon Flux

When simulating the flux of cosmic muons at the Earth's surface to be propagated underground, there are two formulae that can be used. They are known as the Gaisser formula [9], and the Reyna parametrization [128].

Because of the spherical geometry of the Earth the overall muon flux at the surface has the form of a $\cos^2\theta$ distribution [9], where θ is the polar angle measured from the vertical which is taken to be 0°. The shape of this distribution is different for different muon energy ranges.

Muons with lower energies, in the GeV range, have a spectrum more sharply peaked at the vertical since these muons will mostly decay before they reach the ground. At higher energies, the muon distribution approaches a secθ shape. Because of this, the parametrizations for the muon flux listed above have been developed to take energy and angle into account.

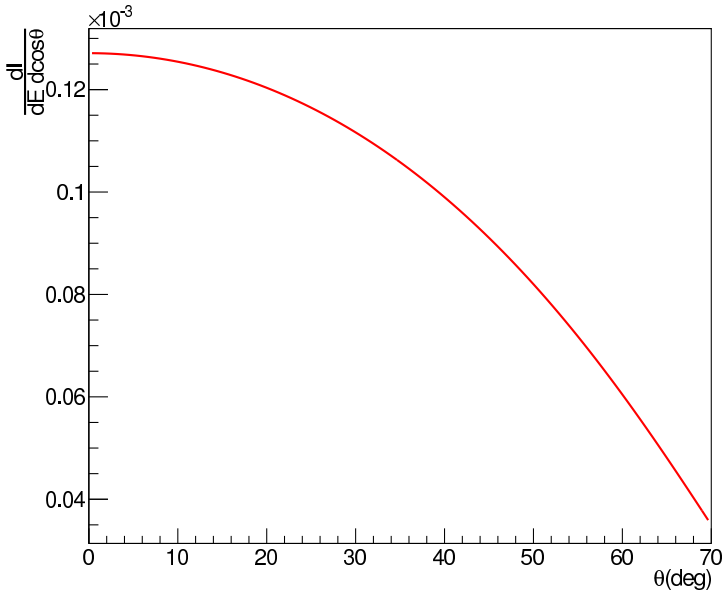

Figure 2.3: Angular distribution for 10 GeV muons (Reyna).

The Gaisser formula, which has been widely used with success, models the flux on the Earth's surface as a function of energy and angle and is valid for $E_\mu > \frac{100}{cos\theta}$ GeV, and for polar angles less than 70°. The formula is given as

$$\frac{dI}{dEdcos\theta} = \frac{0.14\, E_\mu^{-2.7}}{s\ cm^2\ sr\ GeV}\left[\frac{1}{1+\frac{1.1E_\mu cos\theta}{115GeV}} + \frac{0.054}{1+\frac{1.1E_\mu cos\theta}{800GeV}}\right] \tag{2.3}$$

The two terms in the brackets represent the contribution to the muon flux by pions and kaons, respectively. It has been observed by many experiments that the vertical muon flux rises to a plateau up to energies around 100 GeV and begins to fall after energies around 115 GeV. This is due to the fact that pions that would normally decay and produce muons will instead decay via strong interactions. This formula is adequate for deep experiments but a better parametrization is needed for more shallow sites where the minimum muon energy that makes it to that depth is less than 100 GeV.

D. Reyna has developed a parametrization that agrees with measurements of the muon flux in the range that is important for experiments located in shallow sites and is valid for all angles [128]. The form of this equation is

$$I(p_\mu, \theta) = cos^3(\theta) I_V(p_\mu cos\theta) \tag{2.4}$$

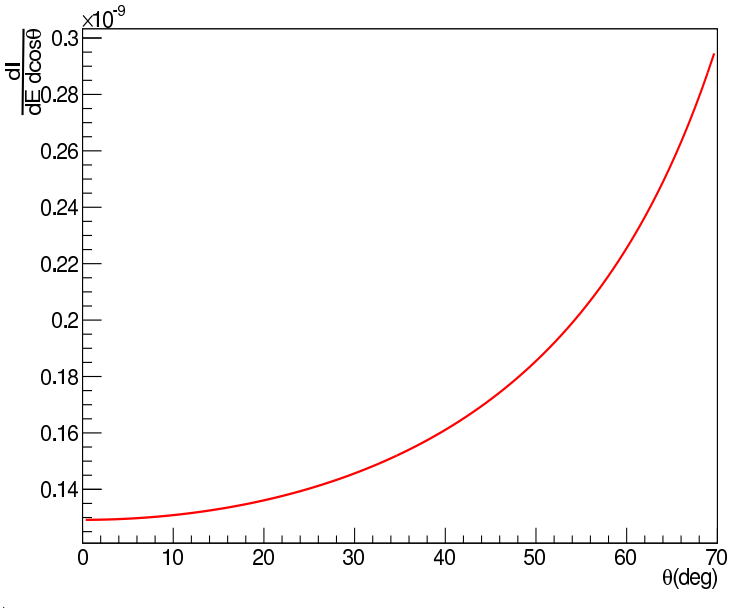

Figure 2.4: Angular distribution for 1 TeV muons (Gaisser).

and it is valid for muon momenta in the range $1\ GeV < p_\mu < \frac{2000}{cos\theta}\ GeV$

This parametrization is a modification to one developed by Bugaev to model the intensity of vertical muons as a function of momentum [129], given as

$$I_V(p_\mu) = c_1 p_\mu^{-(c_2 + c_3 log_{10}(p_\mu) + c_4 log_{10}^2(p_\mu) + c_5 log_{10}^3(p_\mu))} \tag{2.5}$$

where the original values of the coefficients were fit for different ranges of muon momentum, and where

$$c1 = 0.00253 \qquad c2 = 0.2455 \qquad c3 = 1.288 \qquad c4 = -0.2555 \qquad c5 = 0.0209 \tag{2.6}$$

There is currently no theoretical explanation as to why this formula is valid for such a wide range of angles and muon momenta. Despite the current lack of a theoretical foundation, the parameters of this formula have been derived from a best fit χ^2 of the available data and it can safely be used at sites shallow enough that muons with energies above 1 GeV survive to depth.

2.3 Simulation of Cosmic Muon Flux Underground

To model the flux of cosmic muons underground we make use of the MUSIC code, developed by Antonioli et al. [130] MUSIC, which stands for MUon SImulation Code, was developed

as an improvement to existing muon transport codes. It makes use of more accurate cross section calculations and employs a more detailed treatment of processes between muons and surrounding matter. The code considers energy loss processes on a continuous or stochastic basis depending on the process and the fractional energy transfer. Energy loss due to ionization as the muon travels through matter is well understood to be a continuous process and described by the Bethe-Bloch formula [131]. Relativistic muons, such as those generated in cosmic ray showers, are known as minimum ionizing particles (mip) since they lose minimal energy to ionization as they travel through matter.

The mean energy loss by a particle travelling through matter is commonly expressed as

$$-\langle\frac{dE}{dx}\rangle = \alpha(E) + \beta(E)E \tag{2.7}$$

where $\alpha(E)$ is the energy loss due to ionization and $\beta(E)$ is the relative energy loss from other processes.

Processes such as bremsstrahlung, inelastic scattering, pair production, and knock-on electron production cannot only be treated continuously because they can cause relatively large energy losses in single events. Knock-on electrons, also known as delta rays, are electrons that are knocked out of their orbitals and have enough energy to cause further ionization. Energy losses due to these processes are treated in the following way

$$\langle\frac{dE}{dx}\rangle = \langle\frac{dE}{dx}\rangle_{continuous} + \langle\frac{dE}{dx}\rangle_{stochastic} \tag{2.8}$$

$$= E\frac{N}{A}\int_0^{v_{cut}} v\frac{d\sigma}{dv}dv + E\frac{N}{A}\int_{v_{cut}}^1 v\frac{d\sigma}{dv}dv \tag{2.9}$$

where N is Avogadro's number, A is the atomic mass of the material, v is the fractional energy loss, and $\frac{d\sigma}{dv}$ is the cross section of the process. The time needed to perform these calculations is sensitive to the value of v_{cut} and a value of 10^{-3} was chosen to achieve a balance between computing time and accuracy. It is possible, but not recommended, for the user to change this cutoff value.

MUSIC is a 3-D simulation code in the sense that it is a modification to a 1-D muon transport code authored by V. Kudryavtsev *et al.* The inputs to the code effectively amount to the energy of the muon at the surface and the path length it will travel underground. It will output the energy, angular deviation and lateral displacement after transport. Other features of MUSIC include the fact that it takes into account the radiation length, average density, and composition of the rock through which the muons are propagated. The user can input information for up to 20 elements that characterize the rock which includes the A and Z values of the constituent elements as well as their fractions.

An accurate simulation of the cosmic muon flux at an underground site requires knowledge of the elevation of the land comprising the overburden. The simulations developed in this dissertation make use of the most precise elevation data avaiable from the National Elevation

Dataset [132] (NED). The sites for which simulations presented in this dissertation have been carried out utilize elevation data with a resolution of 1/3 arcsec. This translates to a distance of approximately 10 m between elevation data points. The elevation data is provided in the form (lat,lon,elevation) where latitude and longitude are given in degrees and elevation is given in meters above sea level. The simulation procedure outlined here requires the calculation of the path length between each elevation data point and a point chosen at the underground site. For this reason, the latitudes and longitudes of the elevation data points must be converted to units of meters. This is accomplished through a conversion from latitude and longitude to easting and northing, which are the coordinates used in the Universal Transverse Mercator (UTM) system.

The UTM system was developed in the 1940s by the United States Army Corps of Engineers as a 2 dimensional cartesian coordinate system that could be applied to the surface of the Earth which would be independent of altitude [133]. The surface of Earth is divided into 60 sections which are 6° wide in longitude. These sections, known as zones, range from 80° S to 84° N in latitude. The origin of the cartesian coordinate system in each zone is the intersection of the equator with the central meridian line within that zone. The easting value of this meridian is set to 500,000 m. Northing values are calculated separately for the northern and southern hemishperes. For points in the northern hemisphere, northings begin at 0 m at the equator and increase in the northward direction. Northing coordinates in the southern hemisphere are set at 10,000,000 m at the equator and decrease in the southward direction. These standards are used for all zones to make sure that there are no negative numbers in the UTM system. Each zone is divided into sections that have a range of latitude of 8° and each of these sections is assigned a letter. The letter "N" is assigned to the first section in the northern hemisphere in every zone, and the sections progress through the English alphabet in the northern direction.

The conversion from latitude and longitude to easting and northing was carried out using a conversion utility found online and maintained by Professor Steven Dutch of the Department of Applied and Natural Sciences at the University of Wisconsin, Green Bay [134]. An excel spreadsheet is available for use at this site and the conversion routine therein was adapted into a C++ code to facilitate the conversion and manipulation of a relatively large number of elevation data points required by the analyses presented in this dissertation.

A sample of muons consisting of their energy at the surface and path from the surface to the chosen underground point was generated in the following way. The distance from each elevation point to the chosen point underground are calculated using simple trigonometry, ignoring the curvature of the earth.

$$d = \sqrt{r^2 + z^2} \tag{2.10}$$

where r is the distance from the elevation data point in question to the point on the surface directly above the chosen underground point and z is the vertical distance to the surface from the chosen underground point, given by

$$r = \sqrt{(easting - x_0)^2 + (northing - y_0)^2} \qquad z = elevation - z_0 \tag{2.11}$$

where x_0 and y_0 are the coordinates of the point on the surface directly above the chosen underground point and z_0 is the elevation of the underground point with respect to sea level. The polar and azimuthal angles in degrees of each elevation data point with respect to the underground point are given by

$$\theta = \frac{180}{\pi} \arctan(\frac{r}{z}) \qquad \phi = \frac{180}{\pi} \arctan(\frac{northing - y_0}{easting - x_0}) \tag{2.12}$$

Once the angles and path lengths have been calculated for all of the elevation data points, they are separated by polar angle into groups of 1° from 0° to 70°.

The energy spectrum of cosmic muons has a differential spectral index of 2.7 which means that the number of incident cosmic muons of a certain energy decreases fairly rapidly as a function of energy.

$$\frac{dI}{dE} \propto E_\mu^{-2.7} \tag{2.13}$$

Using either the Gaisser formula or the Reyna parametrization as a weighting factor for the muons in the sample, it is clear that while higher energy muons cannot be ignored, they carry much less weight in a simulation than low energy muons. For this reason, the range of energies included in the simulation are divided up in a logarithmic way with equal number of muons per logarithmic division. It is a simple procedure to use the MUSIC code to find the minimum energy a muon must have on the surface to survive down to depth. For example, if the minimum energy a muon must have is 100 GeV to survive to depth at a certain site, 10^7 muons would be generated with energies given at random between 100 GeV and 1,000 GeV, and the same number of muons would be generated with random energies between 1,000 GeV and 10,000 GeV, and so on. To compensate for this, the weight calculated for the muon must be scaled by

$$\frac{\Delta N}{\Delta E_\mu} \tag{2.14}$$

where ΔN would be 10^7 in this case and ΔE_μ would be 900 GeV for a muon given an energy between 100 GeV and 1,000 GeV.

2.3.1 Simulation of Cosmic Muons at Homestake

The cosmic muon simulation codes used in analyzing the data in this dissertation were developed for a future portable cosmic muon telescope that would be deployed in the Homestake Mine in Lead, SD. The Homestake mine is a proposed location for a Deep Underground Science and Engineering Lab [135, 136] (DUSEL), with a depth of 4300 m.w.e., which would house a far detector for the Long Baseline Neutrino Experiment (LBNE) collaboration [107]. The proposal is to send a beam of muon neutrinos from Fermilab to be measured by a near detector and a far detector. The near detector would be used to characterize the neutrino beam and the far detector would be used to measure the neutrino beam after oscillations

have taken place. Cosmic muons will form a source of background for a detector at DUSEL and therefore it is essential to be able to model the integrated flux as well as the angular distributions.

The proposed telescope would consist of 4 layers of 15 scintillator strips that are 320 cm×30.5 cm each. To achieve an active volume with a square cross section we would have a "tiled in thirds" arrangement of the strips as shown. Simulations for various separations between the top two and bottom two layers were carried out and results shown here are for a 1.2 m separation between the pairs of layers.

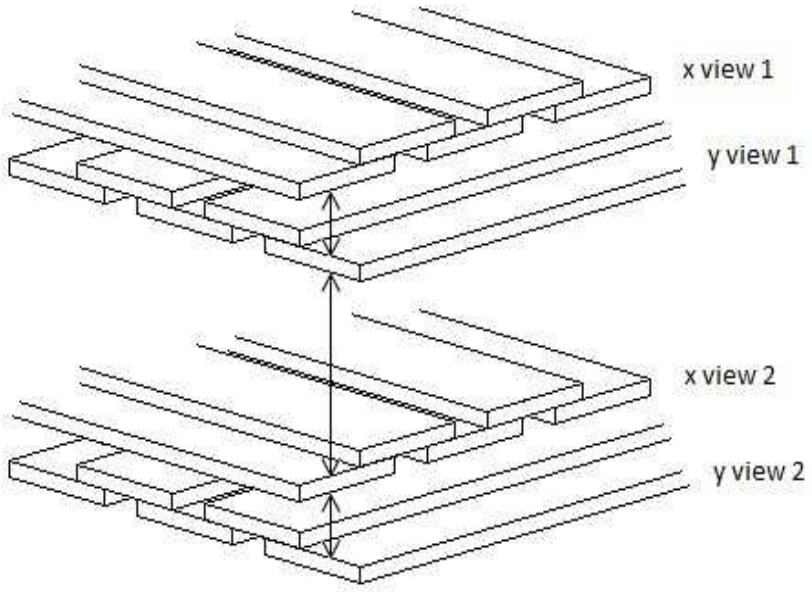

Figure 2.5: The "tiled in thirds" arrangement of the strips in the proposed detector.

The flux at the depth of the mine was simulated using the procedure described above for a flat surface above the mine and using the actual elevation data. A simple geometric simulation of the proposed detector was used to model the detector response in the case of flat land and using the actual elevation data.

2.3.2 Simulation of Cosmic Muons at KURF

Simulations have been performed at various locations within the limestone mine containing the Kimballton Underground Research Facility (KURF). KURF is an underground lab that is currently home to a number of experiments [137, 138, 139]. Field survey measurements were carried out to determine the vertical overburdens at the various locations underground where data was taken. Also, measurements of the average rock density were taken at the KURF sites and found to be $\sim$2.69 $\frac{g}{cm^3}$ which is slightly higher than the density of "standard

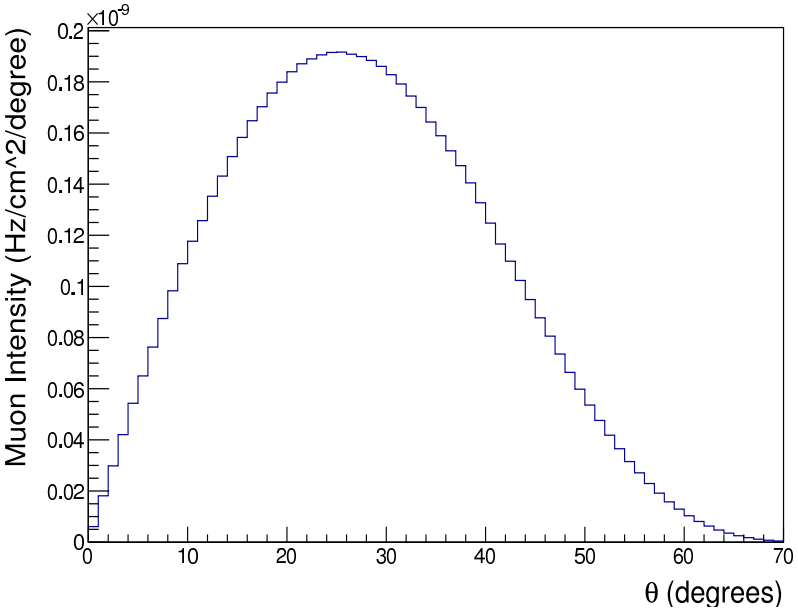

Figure 2.6: The predicted polar angle distribution considering a flat surface above the detector at Homestake.

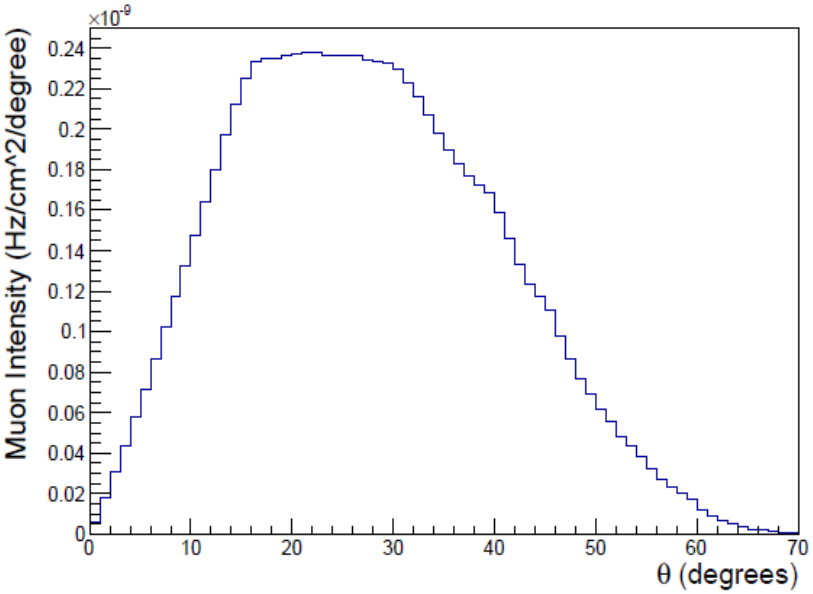

Figure 2.7: The predicted polar angle distribution using actual elevation data at Homestake.

rock" which is assumed to be 2.65 $\frac{g}{cm^3}$. Measurements of the cosmic muon flux underground were carried out at KURF, but not at DUSEL. An analysis of these measurements will be

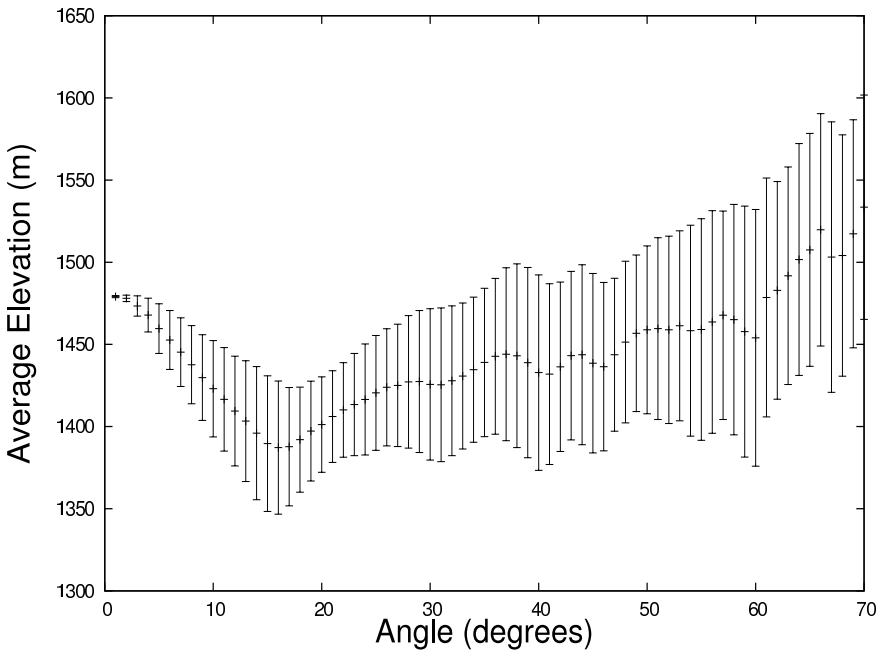

Figure 2.8: The average elevation of the land above the detector as a function of polar angle at Homestake. Features in this graph can help explain the prominent features in the comparison between the flat surface and elevation data predictions.

presented in Chapter 4.

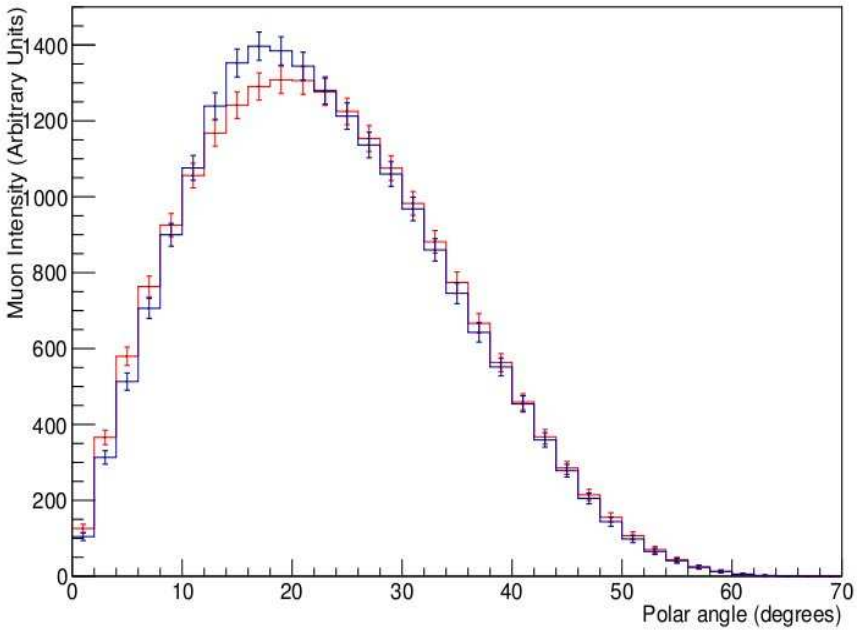

Figure 2.9: Detector simulation for 1 year of data taking at Homestake. The red line is the detector response for flat land above the detector while the blue line is the detector response using the actual elevation data.

Chapter 3

The Muon Detector

The muon detector we used, known as the MegaMini (MM), is a portable prototype of the Outer Veto (OV) muon system of the Double Chooz experiment. The Inner Veto (IV) is designed to tag and track cosmic muons that can enter the most sensitive parts of the Double Chooz detector while the OV is designed to tag and track muons that miss the detector. Muon capture by nuclei can produce long lived isotopes such as ^{9}Li or ^{8}He that will decay by the emission of neutrons which can contribute to a fake signal, as described in Chapter 2.

3.1 Detector Design

The MM is a collection of 32 scintillator strips that are 20 cm x 5 cm x 1 cm. Scintillation light from the strips is collected by two Multi Anode PhotoMultiplier Tubes (MAPMTs) which will be described in this chapter. The strips were manufactured at Fermilab and are composed of three scintillating materials. The strips are made of polystyrene (C_8H_8) with a blend of PPO (1%) and POPOP (0.03%), which are known as secondary scintillators. The addition of these secondary scintillating materials serves to shift the wavelength of the scintillation light from the emission peak of the polystyrene to a wavelength that is absorbed efficiently by a wavelength shifting fiber connecting the strip to the PMT. Polystyrene is a commonly used scintillating material because of its cost and it emits at around 300 nm [140]. PPO has an absorption peak at 300 nm and an emission peak at 350 nm and also acts to strengthen the strip and make it more resistant to deformation because of changing temperatures. POPOP absorbes at 350 nm and emits at 410 nm. Each strip is extruded with a 1.8 mm diameter hole, drilled into the center running along the long axis of the strip, into which a 1.5 mm diameter wavelength shifting fiber (WLS) is inserted. The WLS is manufactured by Kuraray and is a model Y-11 multi-clad non-S type. Multi-clad refers to the outer and inner claddings on the polystyrene core of the fiber which have indices of refraction 1.42 and 1.49, respectively,

whereas the core has an index of refraction of 1.59. The two layers of cladding make up 6% of the diameter of the fiber and gives the fiber almost twice the trapping efficiency of a fiber with only one layer of cladding. The fibers come in two varieties, S type and non-S type. The S type fibers have the polystyrene molecules that make up the core aligned with the axis of the fiber. The advantage of S type fibers is that they are more resistant to losses in efficiency due to bending, but the disadvantage is an attenuation length that is 10% less than the non-S type. The attenuation length of the non-S type fiber is >3.5 m. The WLS has an absorption peak at 420 nm and emits [141] at 476 nm. A fiber with this emission peak was chosen to match the peak response frequency of the photocathode on the MAPMT. The strips have a 0.25 mm thick reflective coating of TiO_2 to minimize light losses that covers the all but the 5 cm x 1 cm faces. The back face of each strip is covered by a reflector which the fiber is fastened to by glue to ensure that the fiber collects as much light from the strip as possible.

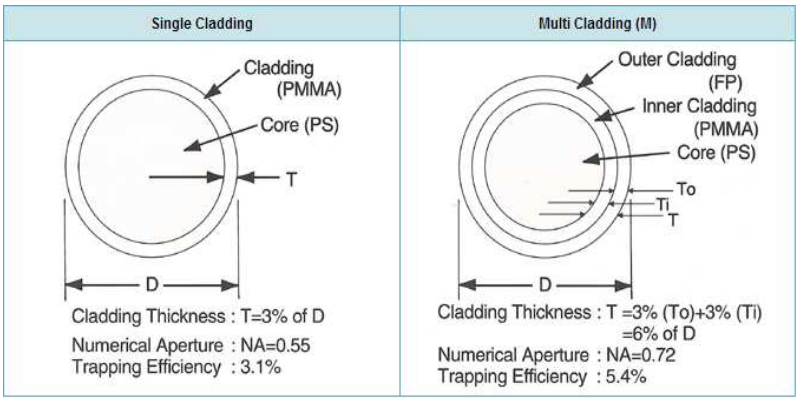

Figure 3.1: Single-clad and multi-clad fibers from Kuraray [6]

The 32 strips of the MM are grouped into 4 pairs of layers known as bilayers or modules. A single layer is made of 4 strips which are layed out side-by-side so that they are in contact along their 20 cm x 1 cm faces. In this arrangement, there is a dead space of 3 mm between strips. A bilayer is a pair of layers stacked on top of one another where all 8 strips are oriented the same way, but one of the layers is offset by 2.5 cm as shown in Fig. 3.4. The strips are aligned this way to reduce the dead space in the bilayer by ensuring that if a muon passes through the dead area between the strips of one of the layers that it will almost certainly be detected as it passes through the next layer. The 4 bilayers are stacked on top of each other so that successive bilayers are oriented orthogonally. There is an Aluminum sheet that creates a space of 2 mm between layers within a module, and a space of 4 mm between modules because of neighboring sheets. This setup allows us to efficiently select muon events and reject background. The two main backgrounds are gamma rays and neutrons from radioactive decays. The detector was exposed to sources of both backgrounds for testing purposes. Gamma rays between 0.5 MeV and 10 MeV have a 5% chance of double Compton scattering to cause hits in overlapping strips, but have a negligible probability of causing 8

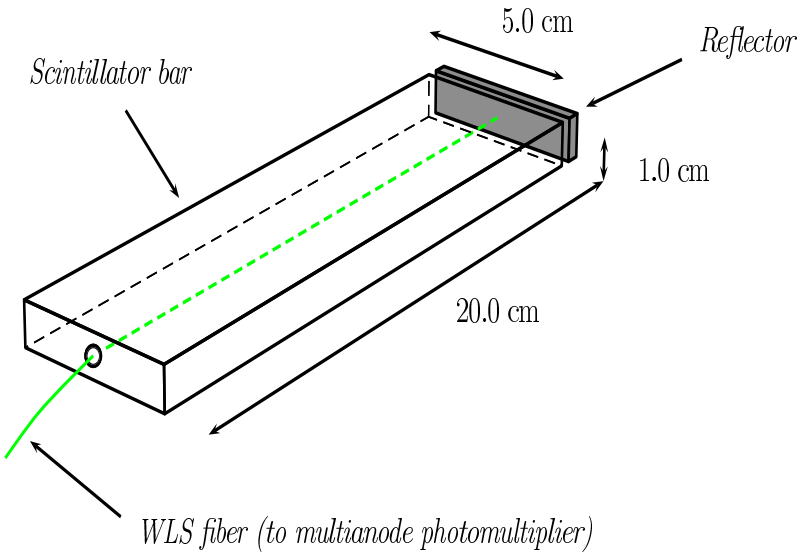

Figure 3.2: A diagram of a typical strip in the detector.

Figure 3.3: A photo of a strip with the white TiO_2 coating visible.

fold coincidences. The 8 fold coincidence requirement also reduces the background due to neutrons down to a negligible level.

We use two MAPMTs to collect the scintillation light from the scintillator strips and convert it into electronic pulses to be used by our Data Acquision System (DAQ). The 64 channels of each MAPMT are in an 8 x 8 grid of pixels with each pixel having an effective area of 2 mm x 2 mm with 0.3 mm of dead space between neighboring pixels. The WLS fiber has a diameter of 1.5 mm and it must be aligned precisely to the corresponding pixel on the

Figure 3.4: A photo of the cross section of a bilayer or module.

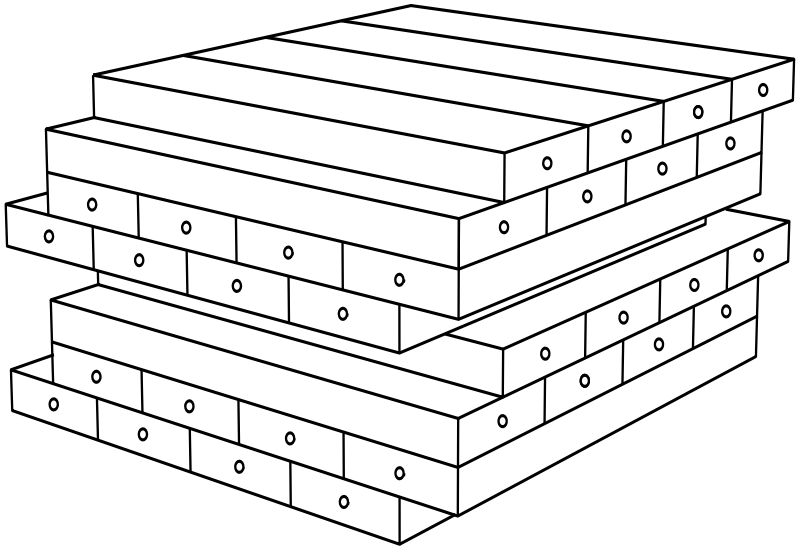

Figure 3.5: A schematic diagram of the detector.

face of the MAPMT because a significant amount of light can be lost to crosstalk if this is not done properly. To align the fibers with the pixels of the MAPMT a fiber holder was created with 64 precision drilled holes to match the layout of pixels on the face of the PM. Alignment markings that have been machined into the face of the PM by Hamamatsu were used to allign a precision template with drill bushings which was used to drill dowel pin holes for both the MAPMT and the fiber holder. Crosshairs were etched into a glass window on the template to be aligned with the alignment markings on the face of the MAPMT. The template was then secured to the MAPMT with screws and precise dowel pin holes were

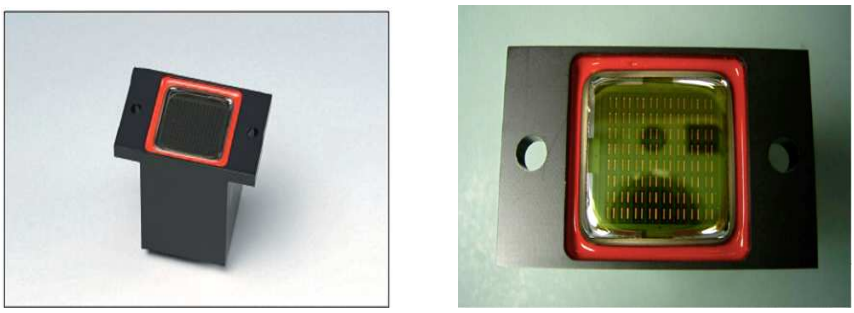

Figure 3.6: The Hamamatsu multianode photomultiplier tube model H8804.

drilled. The same procedure was used to drill the dowel pin holes into the fiber holder. With the addition of dowel pins, the fiber holder and the face of the MAPMT can only fit together in the proper way. Each MAPMT recieves light from 2 bilayers, comprising 16 channels. The fibers from these 16 channels are arranged in the 64 slots of the fiber holder so that they are not read by neighboring pixels. This also greatly reduces the contribution of optical crosstalk that is close to zero in the case of this detector.

The MAPMTs have time counters that are not synchronized. Therefore, a correction due to the offset between the boards must be applied in order to establish time coincidences as described in the next section. The offset is found by analyzing all of the data files in a run and plotting a histogram of the time difference between events in each module. The time corresponding to the low edge of the maximum bin of this histogram is used as the offset. The clocks used by the MAPMTs keep time in 16 ns intervals and have a range of $2^{32}\times16$ ns which comes out to 68.719 s and the clocks run from -2^{31} to $+2^{31}$. The offset is in units of 16 ns.

The MAPMT is manufactured by Hamamatsu and is a model H8804. The H8804 has a borosilicate glass window under which there is a single bialkali photocathode that has a minimum effective area [142] of 18.1 mm x 18.1 mm. Behind the photocathode there are focusing electrodes that guide the photoelectrons to the corresponding one of 64 channels. Each channel is a collection of 12 stages of dynodes that multiply the charge that comes from the photocathode and there is a separate anode output for every channel. There is a custom made PCB fixed to the base of the MAPMT to set the voltage ratios recommended by Hamamatsu to each of the 12 stages of dynodes. With a high voltage (HV) level of 800 V a channel will typically have a gain of 5×10^5. The anode outputs are multiplexed for use with an external ADC.

There is a front end electronics board for each MAPMT with a MAROC2 chip which has 64 inputs that are connected to the outputs of the H8804. MAROC stands for Multi Anode ReadOut Chip and is designed to read out MAPMTs. It contains a variable gain preamplifier, fast and slow pulse shapers, and a Wilkinson 12 bit ADC [143]. The variable gain preamp serves to correct for the dispersion of the gains from the 64 channels of the PMT. The signal

then passes through a current mirror that is connected to the fast and slow pulse shapers in parallel. The fast shaper has a typical peaking time of 10 ns and feeds comparators to decide if the channel was hit above threshold. The comparator levels are set by an internal 10 bit DAC. Signals from the fast shaper go to latches in the Field Programmable Gate Array (FPGA) which is located on the USB board. The trigger for the FPGA is a 64-fold-or meaning that when any latch is flipped, indicating a channel hit above threshold, a time window of 64 ns is open and any more latches that flip during that time will be part of an event. 64 ns corresponds to 4 clock cycles dictated by the 62.5 MHz external clock. The outputs of the latches go to a FiFo with a 32-bit timestamp, a hold is sent to the MAROC2, a copy of the data is sent to the ADC-Logic on the FPGA, and a dead time of 80 ns is set to allow the latches to reset. The slow shaper has a peaking time of 100 ns with a track-hold which allows enough time for a trigger to be formed in the FPGA. The ADC-Logic on the FPGA reads the data from the track-and-hold buffers on the MAROC2 to a Wilkinson ADC. The Wilkinson ADC works by allowing the input pulse to charge a capacitor until the voltage of the capacitor is equal to the voltage amplitude of the input signal. When this condition is met, the capacitor is allowed to linearly discharge while a gate is kept open to let clock signals through. The number of clock signals that are read as the capacitor discharges is proportional to the amplitude of the input signal. The front end boards are connected to the USB board with ethernet cables and the he USB board is connected directly to a PC. The Event Builder software processes 3 data streams coming from the USB board: trigger data packets, ADC data packets, and Unix timestamp packets. We programmed the Event Builder to write data to signal files in intervals of approximately 20 s. An individual run is made up of 180 signal files for approximately 1 hour of run time.

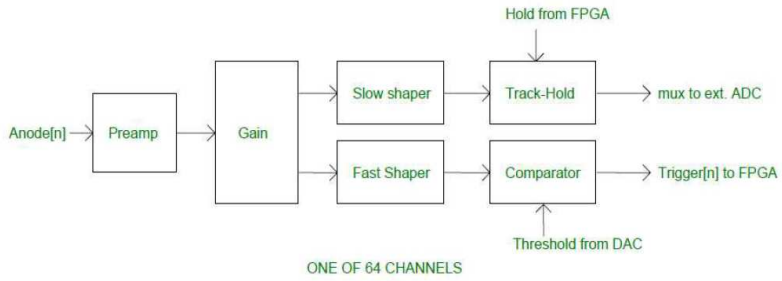

Figure 3.7: A diagram of a channel in the MAROC2.

The entire assembly containing the MM, the modules used to power the MM and electronics, and the PC with the Event Builder are portable enough to fit on a cart that can be pushed or carried. The MM along with the front end electronics are housed in a light-tight wooden box of approximate dimensions 100 cm x 70 cm x 20 cm that is painted black on the inside. The high voltage and low voltage power supplies along with the PC are outside the box for convenience and to dissipate excess heat.

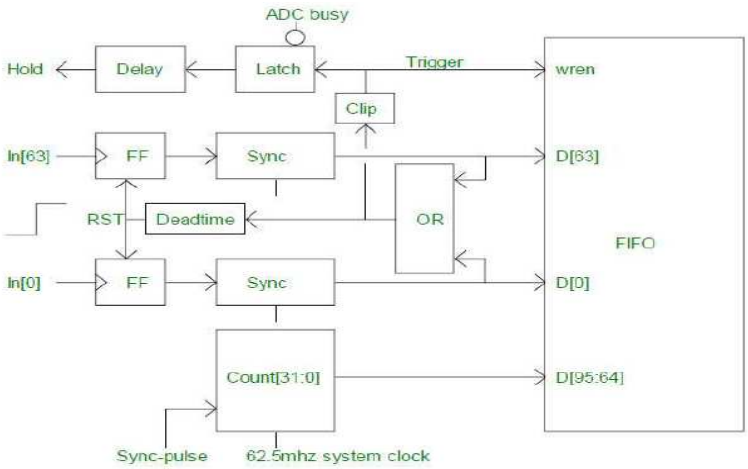

Figure 3.8: Internal logic of the FPGA.

Figure 3.9: A picture of the USB board with the Altera FPGA.

3.2 Electronics Testing and Calibration

The linearity of the response of the MAROC2 and its internal ADC were tested in two different ways. The first technique used was charge injection in which a pulser was directly connected to a single PMT socket, completely bypassing the MAPMT. The second method called light injection consisted of connecting the MAPMT to the MAROC2 and illuminating the pixels with a light source of varying intensity.

For charge injection the amplitude of the pulse was varied between 1 V and 10 V for pulse widths of either 7 ns, 10 ns, or 15 ns. The output of the pulser was put through a 10 kΩ resistor in order to measure the amount of charge injected by each pulse. An oscilloscope was used to perform a time integration on the voltage of the pulse, which is used to find the total charge injected by dividing by the resistance, according to the formula

$$\int \frac{V(t)}{R} dt = \int I(t) dt = Q \tag{3.1}$$

Figure 3.10: The box containing the detector with the laptop, HV and LV modules on top.

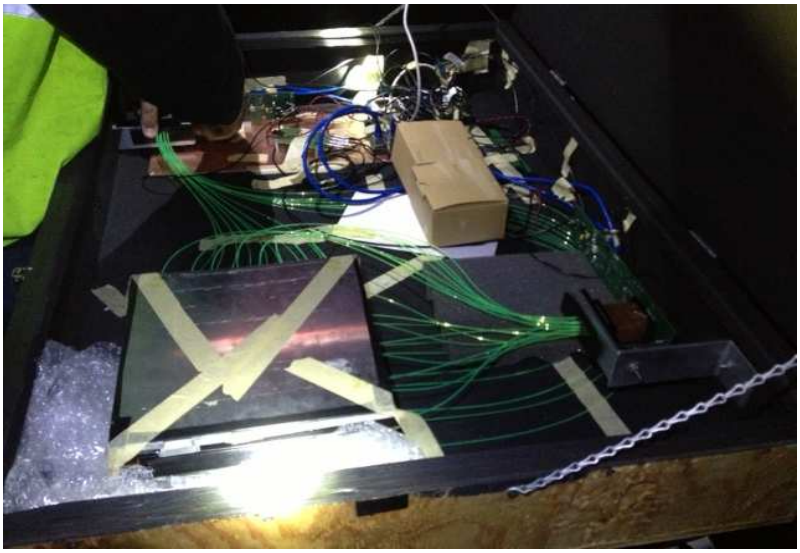

Figure 3.11: The detector inside the box. The green fiber optic cables are visible that connect the strips to the MAPMTs.

The amount of charge injected was plotted against the ADC count registered by the chip. Nonlinearity was observed in the response of the chip and is apparently a function of pulse width. Using 7 ns pulses a plot of the charge output versus the ADC count showed a 30% nonlinearity at 1000 ADC. A longer pulse with was found to reduce the nonlinearity effect.

This observation suggested that the linearity of the chip should be tested with the MAPMT connected, and instead of an electronic pulser, a pulsing LED made by PicoQuant was used. The pulses had a width less than 5 ns. First, the relationship between the input light intensity and the charge output of the MAPMT was measured. The MAPMT was plugged into a standard base which was connected to an oscilloscope. The MAPMT was then connected to the MAROC2 to measure the charge versus ADC count. This plot shows a linear response of the MAPMT combined with the MAROC2 from 100 ADC to 1300 ADC.

The response of each channel of the MAPMT should ideally be equal, but in practice this is never the case. Similarly, the response of each of the two MAPMT is different. The ADC to Photoelectron (PE) ratios are 16.9:1 and 15.8:1 for the two PMT boards. The fibers that connect the strips to the electronics are also different lengths. To correct for this we perform a calibration on each channel. If we examine the ADC distribution for a single channel consisting of all hits above a threshold of 1/3 PE we see a prominent spike at 1 PE which comes from non-muon events. This includes gamma rays from spallation, which come from radioactive decays in nearby rocks that enter the detector and will typically yield 1-2 PE. Gamma rays are used in the calibration of the channels by establishing a 1 PE peak. Separate clocks are used for each PMT board and an offset must be calculated and implemented to establish time coincedences between the two modules.

We would like to clean the data so that the ADC distribution contains entries only from muons. To be certain that the ADC values in the distributions have come from muons, we begin with a sample of events with an 8 fold coincidence, meaning overlapping strips in all 8 layers were hit above threshold within the preset time window, and select the strip with the maximum ADC in each bilayer. We find the peak of this distribution by fitting a gaussian function to a suitable range near the peak of the distribution and scale it to 200 ADC. The value 200 ADC was chosen for three reasons. The MAROC2 chip has a significant nonlinearity above 1000 ADC and we know that the muon ADC distribution has a long tail, therefore we would like to keep the number of muons that can deposit more than 1000 ADC to a minimum. Also, since muons typically yield between 4 and 6 PE, the application of a gain constant would provide further separation of signal to background. Finally, the gain of the preamp in the MAROC2 is designed to be set in multiples of 1/16 from 0 to 40 and it is known to be nonlinear when the gain is set below 7 or above 32. The choice of 200 ADC is convenient because the gain for most channels set at 21 or 22.

The data taken on the surface consists of enough muon events that we have a low statistical error. This is not the case for the data taken inside the mine, so we use a slightly different calibration technique. First, we scale the average ADC of each channel to 200 ADC with no fitting at this stage. We then combine the ADCs from all channels into a single pulse

amplitude distribution. A fit is performed on this aggregate distribution and is scaled so that the peak is at 200 ADC. That scaling factor is then applied to each channel. A 1 PE peak is seen near 20 ADC and this is caused by natural radioactivity.

The calibration of each of the channels is necessary for determining the consistency of the response of the detector as a function of threshold. As the threshold of the detector is changed, the efficiency we calculate for the bilayers changes. Raising the threshold will result in an increase of muon events that are cut and will lower the efficiency and ultimately the rate.

3.3 Detector Efficiency and Data Purity

The calculation of the muon rate takes into consideration the efficiencies we calculate for each of the the bilayers and the estimated purity of the data. The efficiency of each bilayer depends on the minimum threshold that we select for the detector and from the geometrical acceptance. We derive an estimation of the lower limit of the purity of the data which depends on the efficiency.

The efficiency of a bilayer is essentially a measure of how often that particular bilayer detects overlapping hits in events that are almost certainly muons. Considering events where 3 of the 4 bilayers record overlapping hits above a high threshold, which is 4 PE in our case, ensures that the event is most likely the result of a muon. Using that subset of events, the events containing overlapping hits in the bilayer in question are counted. We estimate the efficiency of the bilayer by taking the ratio of the number of events that have hits in all 4 bilayers, with a low threshold for the bilayer in question and a high threshold for the other three, to the number of events that have high threshold hits in the other three bilayers. We choose 1/3 PE as the low threshold and 4 PE as the high threshold. The efficiency for the entire MM is calculated as the product of the efficiencies of each bilayer. The efficiency of a bilayer is computed as

$$\epsilon_i = \frac{N^i_{3+1fold}}{N^i_{3fold}} \tag{3.2}$$

where N^i_{3fold} is the number of events in which every bilayer besides the ith were hit above the 4 PE threshold. $N^i_{3+1fold}$ is the number of events in which the ith bilayer was hit above the lower threshold of 1/3 PE and the other bilayers were hit above the higher threshold.

We also estimate the minimum purity of the muon sample in the following way

$$N_{4-fold} = N^{\mu}_{4-fold} + N^{rad}_{4-fold} \tag{3.3}$$

where N_{4-fold} is the total number of events that have overlapping hits in all four bilayers,

Table 3.1: A table of bilayer efficiencies.

Bilayers	Efficiencies (%)
x_1	75.2 ± 0.1
y_1	84.4 ± 0.1
x_2	81.2 ± 0.1
y_2	96.0 ± 0.1

N^{μ}_{4-fold} is the number of 4-fold events due to muons, and N^{rad}_{4-fold} is the number of 4-fold events due to radiation.

$$N^{i}_{3-fold} = N^{\mu}_{4-fold}/\epsilon^{\mu}_{i} + N^{rad}_{4-fold}/\epsilon^{rad}_{i} \tag{3.4}$$

where N^{i}_{3fold} is the number of events in which 3 bilayers, besides the ith bilayer, were hit above a low threshold, ϵ^{μ}_{i} and ϵ^{rad}_{i} are the bilayer efficiencies for muons and radiation, respectively. We can then write

$$\frac{N^{i}_{3-fold}}{N_{4-fold}} = \frac{\pi^{\mu}_{4-fold}}{\epsilon^{\mu}_{i}} + \frac{(1-\pi^{\mu}_{4-fold})}{\epsilon^{rad}_{i}} \tag{3.5}$$

If we assume that $\epsilon^{\mu}_{i} > 2\epsilon^{rad}_{i}$ then we can write

$$\pi^{\mu}_{4-fold} > 2 - \frac{N^{i}_{3fold}}{N_{4fold}}\epsilon_{i} \tag{3.6}$$

In some cases the purity can be greater than 1. This is because in calculating the lower bound of the purity, we make the assumption that the efficiency for detecting radiation events is less than half of the efficiency for detecting muons. We can also estimate the purity without this assumption. If we instead assume that the purity of the data is 1 at 4 PE, we can calculate the purity at other thresholds in this way

$$Purity_{threshold} = \frac{Rate_{threshold}}{Rate_{4PE}} \tag{3.7}$$

3.4 Detector Simulation

When reconstructing the muon tracks from the data and comparing the angular distributions with what can be expected from our predictions, it is essential to quantify the most significant effects in order to ultimately correct for them. There are purely geometrical effects due to the fact that we count events only if they have at least 8 hits that satisfy the overlap condition for all four bilayers. Thus, the detector has an angular acceptance that is a function of both spherical angles. Vertical muons will almost certainly pass through all 8 layers of the detector, while muons coming in at higher polar angles are less likely to cross all 8 layers.

Due to the rectagular shape of the detector, muons coming in along the diagonals of the detector are more likely to make it through at higher angles. In addition, the selection of events from the data used for reconstruction must be matched as accurately as possible to the selection made in the simulation. For simplicity, we reconstruct events from the data if they had exactly 8 strips hit above threshold. This selection introduces a bias that supresses the reconstructed flux at higher polar angles, since those muons would be more likely to deposit scintillation light in neighboring strips in the same layer. It should be noted that our simulation of the detector response is only geometrical.

We use the following procedure to estimate the correction to the angular reconstruction due to geometrical acceptance. The size and location of each strip is incorporated into the program that includes a value for the dead space between the strips and separate values for the separation between individual layers and the separation between bilayers. A lateral separation between strips of 0.3 mm is used along with a 0.2 mm separation between layers and a 0.4 mm separation between bilayers. A point on the top layer of the simulated detector is chosen at random and the spherical angles are chosen from parent distributions that we provide. The location of the simulated track is then computed for each of the 8 layers and kept only if it reaches the bottom layer. Our selection includes the additional condition that the track pass through only 1 strip in each layer. This is done to match our selection of the data.

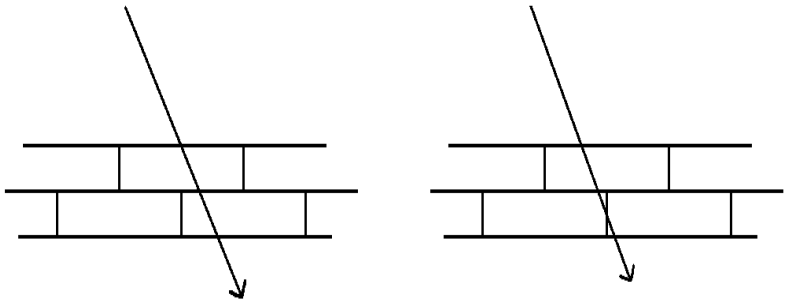

Figure 3.12: Left: A track accepted by our selection. Right: A track rejected by our selection.

Another effect made evident by studying the simulated detector is a smearing between the true and reconstructed angles of the simulated tracks. Any track reconstruction procedure will introduce a smearing effect since we cannot achieve a perfect reconstruction. We first assume that if a strip is hit that it is hit in the center along the axis of the WLS. In the pair of figures below we show the layout of the coordinates used in the reconstruction with an example event in the detector, and an example of a best fit line for the "Y" bilayers in the event.

We use the best fit lines for each bilayer to construct the best fit track in 3 dimensions. As shown in the figure above, we take Δy from the lateral separation between the middle of the top and bottom strips that were hit. We do the same for the hits in the "X" bilayer. The spherical angles are calculated in the following way

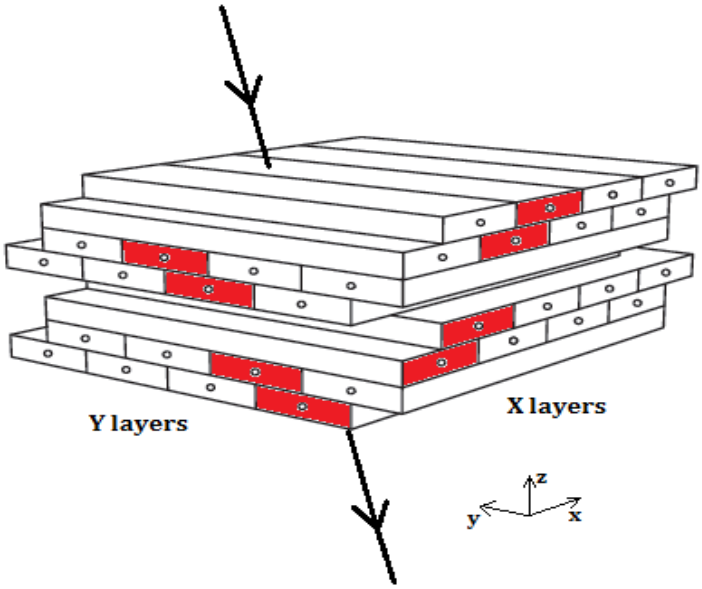

Figure 3.13: A sample event showing which strips were hit in the detector.

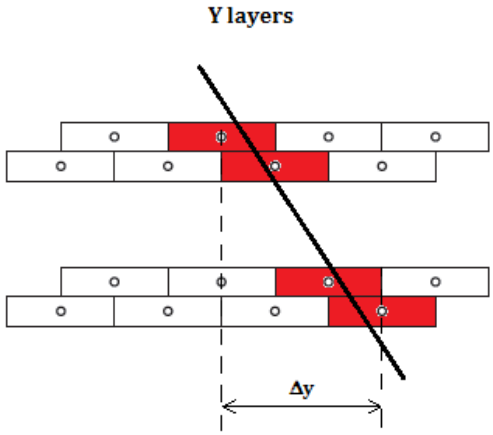

Figure 3.14: Y module hits with the best fit line.

$$\theta = sin^{-1}\frac{\Delta r}{\Delta z} \qquad \phi = tan^{-1}\frac{\Delta y}{\Delta x} \tag{3.8}$$

where $\Delta r = (\Delta x^2 + \Delta y^2)^{\frac{1}{2}}$ and Δz is the height of the detector.

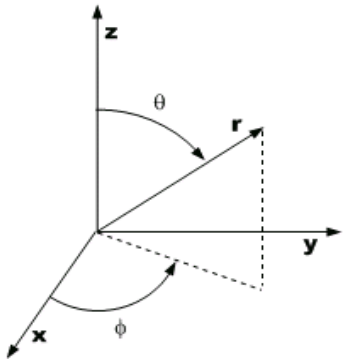

Figure 3.15: The spherical coordinate system we use. Figure from Ref. [7]

Chapter 4

Muon Flux Analysis

We present an analysis of the muon flux conducted at the Virginia Tech campus and at the Kimballton Undergroung Research Facility (KURF). The Virginia Tech campus, located in Blacksburg, VA, is at an altitude of ∼2080 ft (∼630 m) above sea level and the KURF sites have vertical overburdens between ∼290 m.w.e and ∼380 m.w.e on level 2 of the mine. The analysis includes a measurement of the absolute rate as well as an angular reconstruction of the data and a comparison to the theoretical expectation for each site.

4.1 Rate Measurements

We present our measurements of the muon rate in units of $\frac{Hz}{m^2}$. Muon events are defined as having hits in all 8 layers of the detector with the condition that the hits in each bilayer must be overlapping. Calculating the rate involves correcting the number of events divided by the total runtime for detector efficiency, sample purity, and for the effective area of the detector. The efficiency and purity calculations are explained in Chapter 3. We take the purity of the data at 4PE to be 1 and we estimate the purity at other detector thresholds by taking the ratio of the measured rate at 4PE to the measured rate the specified threshold.

To calculate the runtime, the detector was set to take data in intervals, known as runs, of approximately 1 hour. Data from each run is divided into 180 signal files in which data is taken for approximately 20 s. We calculate the total runtime by summing the runtimes for each of the signal files. If the final clock time in the signal file is greater than the initial time, we take the difference. If the final time is less than the initial time, we add 2^{32} and then take the difference. In this way we avoid factoring in the small dead time between each of the signal files. Problems happen occasionally to the detector in which signal files can become corrupted, therefore I include runs in the analysis only if they contain 180 signal files of 20 s each.

Table 4.1: Event counts for the various sites after the application of gain constants. The error is the square root of the number of counts.

Site	1/3 PE	1 PE	2 PE	3 PE	4 PE
Rob316	174235 ± 417.4	164268 ± 405.3	141380 ± 376.0	114103 ± 337.8	86116 ± 293.5
2002	434 ± 20.8	407 ± 20.2	349 ± 18.7	267 ± 16.3	202 ± 14.2
2014	434 ± 20.8	409 ± 20.2	342 ± 18.5	294 ± 17.1	223 ± 15.0
2027	634 ± 25.2	604 ± 24.6	538 ± 23.2	437 ± 20.9	335 ± 18.3
2041	360 ± 19.0	337 ± 18.4	288 ± 17.0	232 ± 15.2	164 ± 12.8
2049	237 ± 15.4	229 ± 15.1	204 ± 14.3	163 ± 12.8	124 ± 11.1
2059	93 ± 9.6	90 ± 9.5	88 ± 9.4	80 ± 8.9	72 ± 8.5
2067	326 ± 18.1	307 ± 17.5	266 ± 16.3	221 ± 14.9	169 ± 13.0

Table 4.2: Runtimes in sec for the various sites

Site	Total Runtime (s)	No. of Runs	Average Time/Run (s)
Rob316	56028	15	3735
2002	44806	12	3734
2014	44672	12	3723
2027	67210	18	3734
2041	59719	16	3733
2049	41075	11	3734
2059	14939	4	3735
2067	44767	12	3731

The detector was deployed in one of the labs on the third floor of Robeson Hall at the Center for Neutrino Physics (Room 316) on the Virginia Tech campus. We estimate the expected flux at our location to be 173 $\frac{Hz}{m^2}$. We obtain this number by using an empirical formula developed by Ziegler [144] in which we use the muon rate at sea level of 130 $\frac{Hz}{m^2}$ to estimate the rate at the altitude of Blacksburg, VA. Ziegler converts altitude in feet to atmospheric density using

$$A = 1033 - (0.03648H) + (4.26 \times 10^{-7}H^2) \tag{4.1}$$

where H is the altitude in feet and A is the atmospheric density in $\frac{g}{cm^2}$. The conversion from the rate at sea level to the rate at Blacksburg, VA is calculated using

$$I_2 = I_1 e^{(A_1 - A_2)/N} \tag{4.2}$$

where I_1 is the muon rate at sea level and I_2 is the muon rate at Blacksburg, VA. N is the muon absorption length given as 261 $\frac{g}{cm^2}$. The formulae provided by Ziegler are used to

Table 4.3: Efficiencies for the various sites after the application of gain constants. The gain constants are explained in Chapter 3.

Site	1/3 PE	1 PE	2 PE	3 PE	4 PE
Rob316	0.594 ± 0.003	0.562 ± 0.003	0.488 ± 0.003	0.398 ± 0.003	0.303 ± 0.003
2002	0.52 ± 0.06	0.49 ± 0.06	0.41 ± 0.06	0.32 ± 0.06	0.25 ± 0.06
2014	0.59 ± 0.05	0.56 ± 0.06	0.48 ± 0.06	0.43 ± 0.06	0.33 ± 0.06
2027	0.52 ± 0.04	0.50 ± 0.04	0.45 ± 0.05	0.37 ± 0.05	0.28 ± 0.05
2041	0.48 ± 0.06	0.46 ± 0.06	0.39 ± 0.06	0.33 ± 0.07	0.23 ± 0.07
2049	0.52 ± 0.07	0.51 ± 0.07	0.47 ± 0.07	0.39 ± 0.08	0.30 ± 0.08
2059	0.58 ± 0.10	0.57 ± 0.10	0.56 ± 0.10	0.50 ± 0.10	0.45 ± 0.10
2067	0.55 ± 0.06	0.53 ± 0.06	0.46 ± 0.06	0.39 ± 0.07	0.30 ± 0.07

predict the rate of all cosmic ray particles given an altitude. We assume that the rate of cosmic muons on the surface scales in the same was as the rate of all cosmic rays on the surface.

Table 4.4: Measured muon rates in Hz/m^2 for the various sites after the application of gain constants. The errors are the statistical error and a 10% systematic error added in quadrature. The systematic error is a conservative estimate of a 2-3% error in rock density and a 5-6% error in site depth added in quadrature.

Site	1/3 PE	1 PE	2 PE	3 PE	4 PE
Rob316	170.9 ± 17.1	170.3 ± 17.1	168.8 ± 16.9	167.1 ± 16.8	165.6 ± 16.6
2002	0.60 ± 0.08	0.59 ± 0.08	0.58 ± 0.08	0.59 ± 0.09	0.59 ± 0.09
2014	0.56 ± 0.08	0.56 ± 0.08	0.56 ± 0.08	0.56 ± 0.08	0.56 ± 0.08
2027	0.58 ± 0.07	0.58 ± 0.08	0.58 ± 0.08	0.58 ± 0.08	0.58 ± 0.08
2041	0.41 ± 0.06	0.41 ± 0.06	0.41 ± 0.06	0.41 ± 0.07	0.41 ± 0.07
2049	0.35 ± 0.06	0.36 ± 0.06	0.36 ± 0.06	0.36 ± 0.06	0.36 ± 0.07
2059	0.35 ± 0.08	0.35 ± 0.08	0.35 ± 0.08	0.35 ± 0.08	0.35 ± 0.08
2067	0.43 ± 0.06	0.43 ± 0.06	0.43 ± 0.07	0.43 ± 0.07	0.42 ± 0.07

4.2 Angular Reconstruction

We performed an angular reconstruction of the data in which we compare the reconstructed angles of the data with the muon angular distribution prediction from simulations using the

Table 4.5: Estimated purities for the various sites after the application of gain constants. We define the purity of measurements at 4PE to be 1.

Site	1/3 PE	1 PE	2 PE	3 PE
Rob316	0.98 ± 0.14	0.98 ± 0.14	0.98 ± 0.14	0.99 ± 0.14
2002	0.99 ± 0.20	0.99 ± 0.20	0.98 ± 0.21	0.99 ± 0.22
2014	0.99 ± 0.20	1.0 ± 0.20	1.0 ± 0.20	1.0 ± 0.20
2027	0.98 ± 0.18	0.98 ± 0.20	0.99 ± 0.20	0.99 ± 0.20
2041	0.99 ± 0.22	0.99 ± 0.22	0.99 ± 0.22	0.99 ± 0.24
2049	0.98 ± 0.27	0.99 ± 0.26	0.99 ± 0.26	1.0 ± 0.26
2059	0.97 ± 0.32	0.97 ± 0.32	0.98 ± 0.32	0.99 ± 0.32
2067	0.99 ± 0.21	0.99 ± 0.21	1.0 ± 0.23	1.0 ± 0.23

MUSIC code. While our detector is fairly efficient at detecting muons because of our 8-fold coincidence requirement, the coarse segmentation of the detector does not allow for very precise angular measurements. The issue is apparently less serious for the polar angle than for the azimuthal angle. In the case of vertical muons, our reconstruction algorithm will always reconstruct their azimuthal angle as either 0°/360°, 90°, 180°, or 270°, and vertical muons will have a reconstructed polar angle of approximately 9°. While the geometrical acceptance for vertical muons is the highest, the smearing effect is the most pronounced since muons with polar angles between 0° and 40° can be reconstructed at approximately 9°. For larger polar angles, there are more possible strip combinations and thus more possible reconstructed angles for both the polar and azimuthal angles. For these reasons, the data is presented in four 20° bins from 0°-80° for the polar angle, and in six 60° bins from 0°-360° for the azimuthal angle. In the comparison between data and simulation, we match the data selection of events with only 8 strips above threshold in our simulatuion by reconstructing simulated muon tracks only if they intersect exactly 8 strips. This is because we do not take into account for strips hit by gamma rays in our simulation. We also take into account the smearing effect and the geometrical acceptance of the detector as described in Chapter 3, but we did not simulate the detector response in the MC. A magnetic compass was used to ensure that the detector was oriented in the same way for every location.

The geometrical acceptance is computed for a particular angular bin in the following way. We simulate the numbers and angular distributions of muons according to our MUSIC simulation and count the number of muons in each angular bin. We then pass these muons through a geometrical simulation of our detector and count the number of muons that make it through the entire detector satisfying our requirement of 8 strips only. The acceptance is estimated as the ratio of these two numbers for each angular bin.

Smearing occurs because the reconstructed angle of the muon can be significantly different than the true angle. The calculation of the smearing effect is similar to the way we calculate

Table 4.6: Comparison of measured muon rates in Hz/m^2 corrected for purity at a 2PE threshold after the application of gain constants. Ziegler's prediction was used for the surface and the MUSIC prediction was used for the underground sites. A 10% error was assigned to the surface prediction for consistency.

Site	Depth (m.w.e)	Measurement (Hz/m^2)	Prediction (Hz/m^2)	Deviation
Rob316	0.0	165.8 ± 16.9	$173.3^{+17.3}_{-17.3}$	-4%
2002	307	0.57 ± 0.08	$0.51^{+0.06}_{-0.06}$	11%
2014	328	0.56 ± 0.08	$0.47^{+0.06}_{-0.05}$	16%
2027	292	0.57 ± 0.08	$0.62^{+0.08}_{-0.06}$	-9%
2041	348	0.40 ± 0.06	$0.37^{+0.04}_{-0.04}$	8%
2049	358	0.35 ± 0.06	$0.33^{+0.05}_{-0.03}$	6%
2059	377	0.34 ± 0.08	$0.31^{+0.04}_{-0.03}$	9%
2067	340	0.43 ± 0.07	$0.41^{+0.05}_{-0.04}$	5%

the geometrical acceptance. Once the simulated sample of muons is passed through our geometrical simulation of our detector, we keep the true angle of the muon and the combination of strips that were hit. Our reconstruction algorithm takes the strips that were hit as inputs and outputs the corresponding reconstructed angles. We start with the number of simulated muons that made it through the entire detector which satisfy our requirement of 8 strips only in a particular angular bin, and then we count how many of those which have reconstructed angles in the same bin. The smearing effect is the ratio of these two numbers.

For example, in our simulation of the flux for site 2002, we predict that 163 muons with polar angles between 0° and 20° will hit the top of the detector. Of these, we predict that 92 will make it through the entire detector and hit only 8 strips. Thus $\frac{92}{163}$ would be the geometrical acceptance of this bin. Of the 92 simulated muon tracks with angles between 0° and 20°, only 60 are predicted to have reconstructed angles between 0° and 20°. Thus $\frac{60}{92}$ would be the smearing effect of this bin.

In order to properly compare data to simulation we scale our data points by the product of these two factors. In the reconstruction of the data taken by the detector on the surface, we also correct for the contamination of events by stray gamma rays. Occasionally, a gamma ray can enter the detector and cause a hit above threshold in a strip. This should much more frequently on the surface than it does inside the mine. The Kimballton Limestone Mine was chosen as a location for KURF partly because of the low amount of background radiation. Events that are thought to consist of a muon and at least 1 gamma are not reconstructed since we only reconstruct events with only 8 strips hit.

The measured flux at all sites is calculated as the sum of the data points.

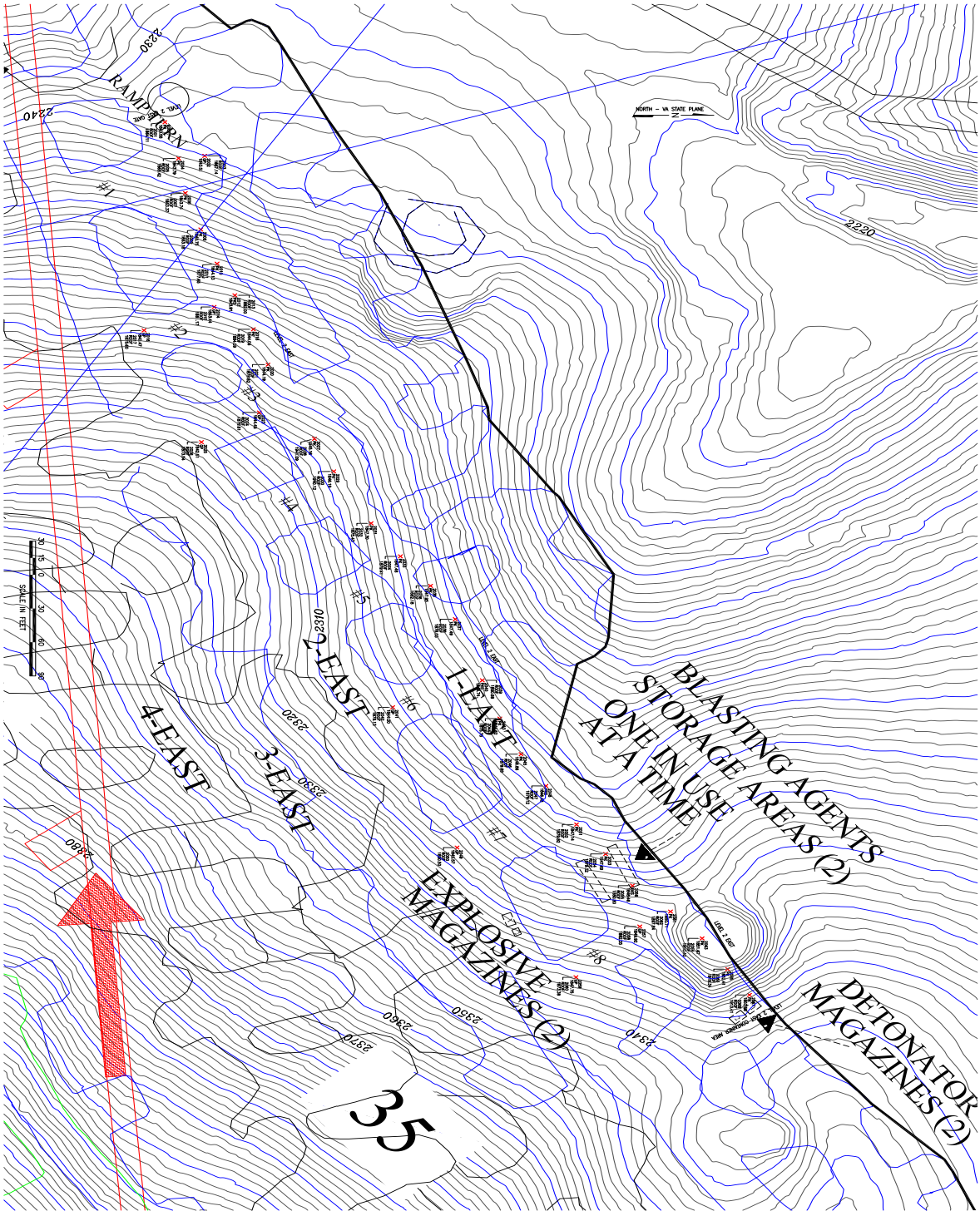

Figure 4.1: A map of the sites on Level 2 of the mine with an overlay of a contour map of the overburden.

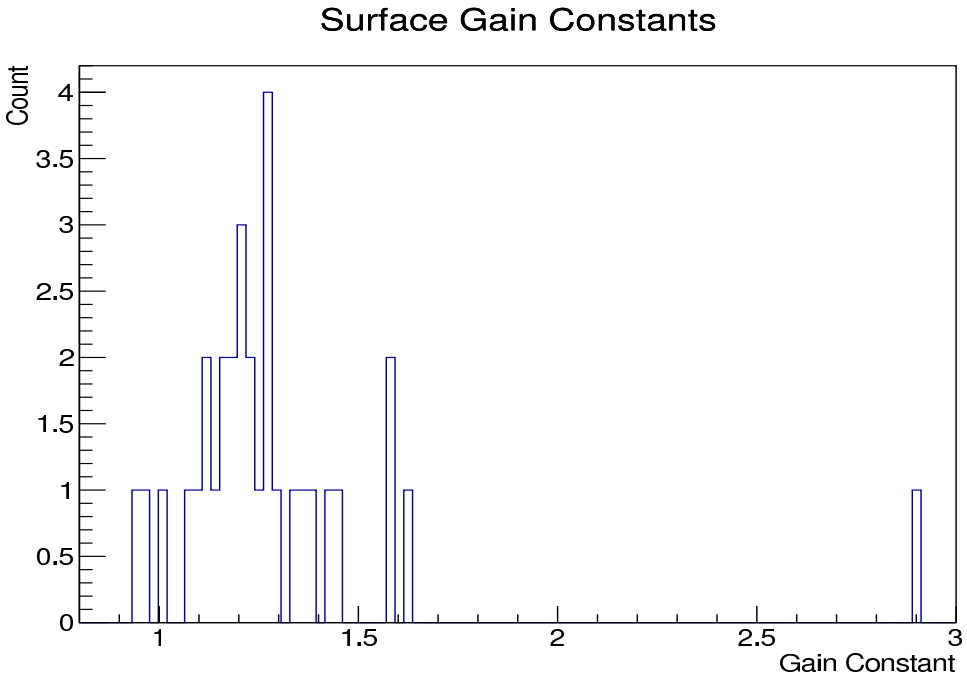

Figure 4.2: Gain constants calculated for the surface. The HV for the MAPMTs was controlled by a NIM crate on the surface.

4.3 Gain Constants

The HV needed to operate the MAPMTs was provided by a NIM crate for data taken in Room 316, while portable HV modules were used for the data taken on level 2 of the mine. The gain constants calculated for the underground sites are slightly larger than the gain constants calculated for the surface data likely due to HV fluctuations because of the relative instability of the power source used in the mine.

All of the gain constants have close to the same value except for a few channels which includes channel 63 of PMT 3. This can be attributed to a few factors. Nonuniformity in the construction of the MAPMT can result in low gain channels in which light collection efficiency is lower by construction. In addition to lower light collection efficiency by construction, the optical fiber connecting this channel to the corresponding strip is longer than other fibers due to the location of the bilayer relative to the MAPMT and has a greater bend. The combination of these factors can explain why this particular channel has an abnormally high gain constant.

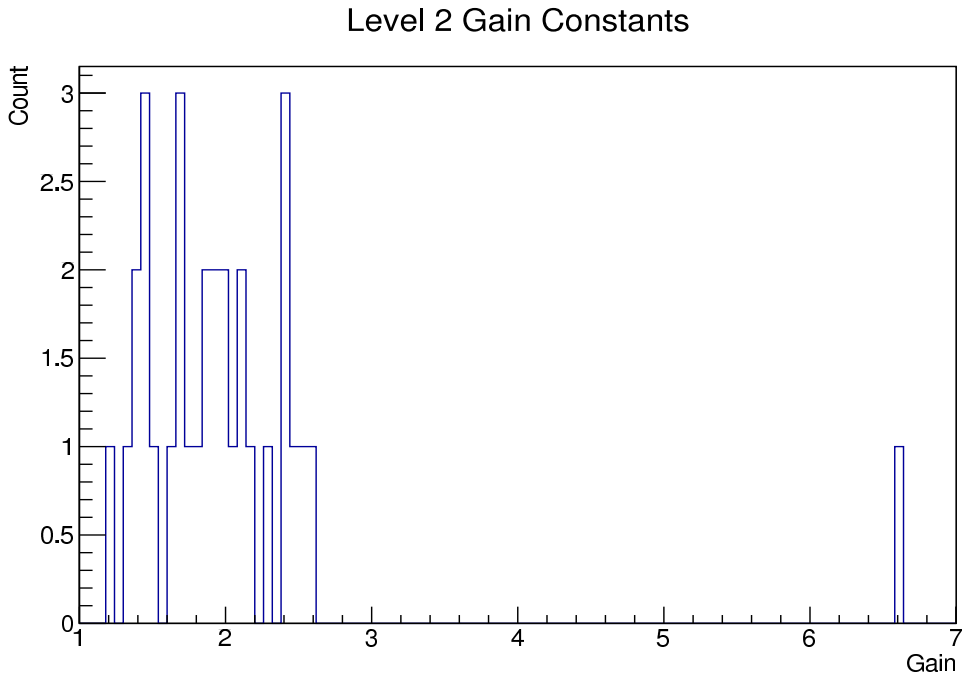

Figure 4.3: Gain constants calculated for the Level 2 sites. The HV for the MAPMTs was controlled by portable HV modules for the underground sites.

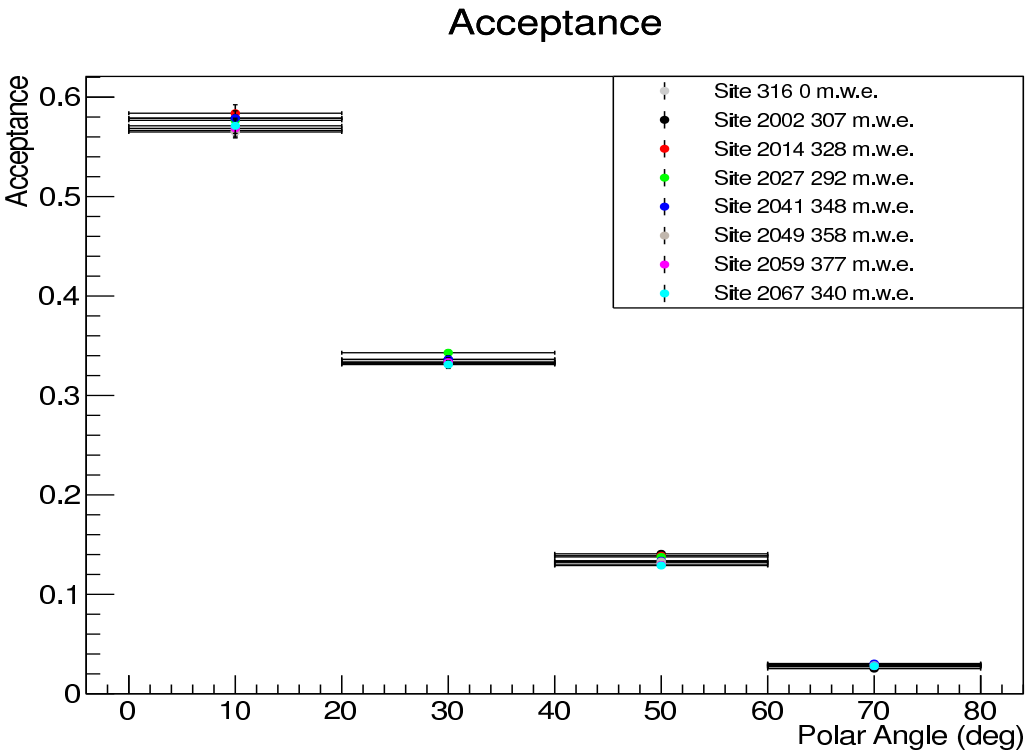

Figure 4.4: Polar angle geometrical accptance of the detector.

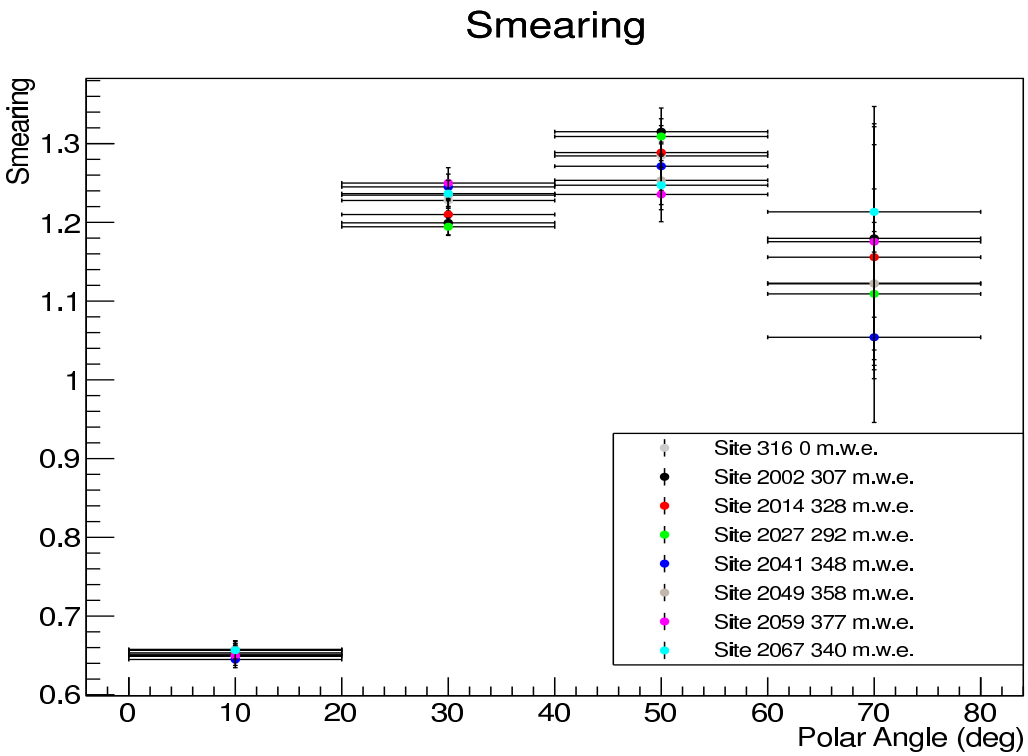

Figure 4.5: Polar angle smearing effect of the detector.

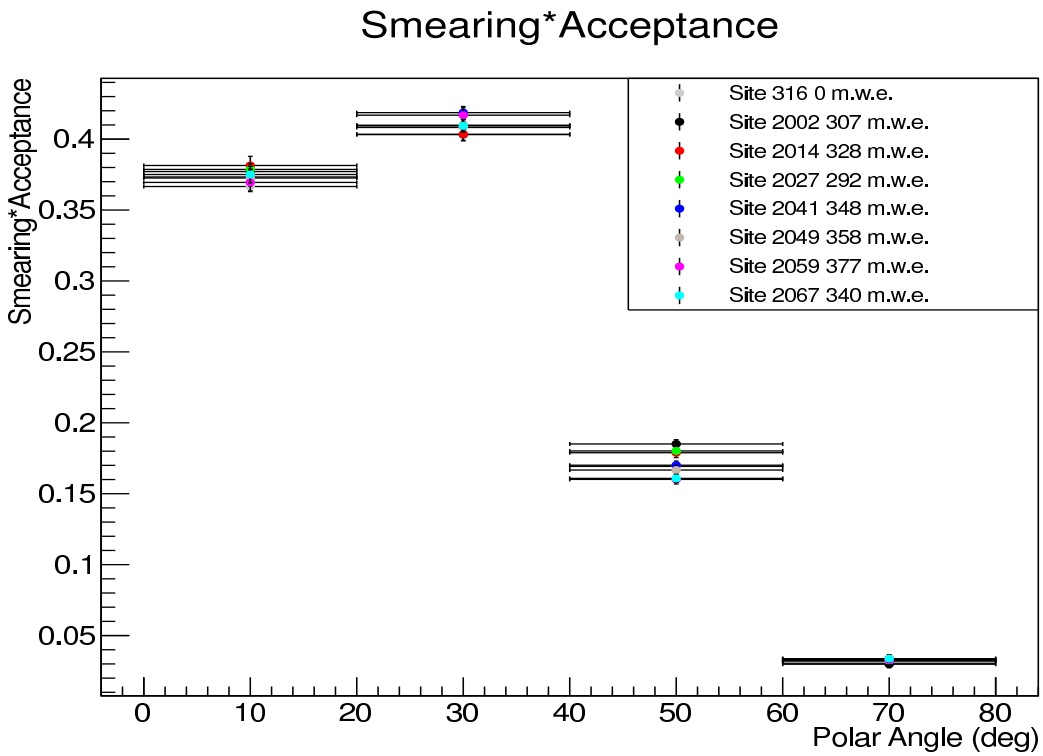

Figure 4.6: Polar angle product of geometrical acceptance and smearing effect.

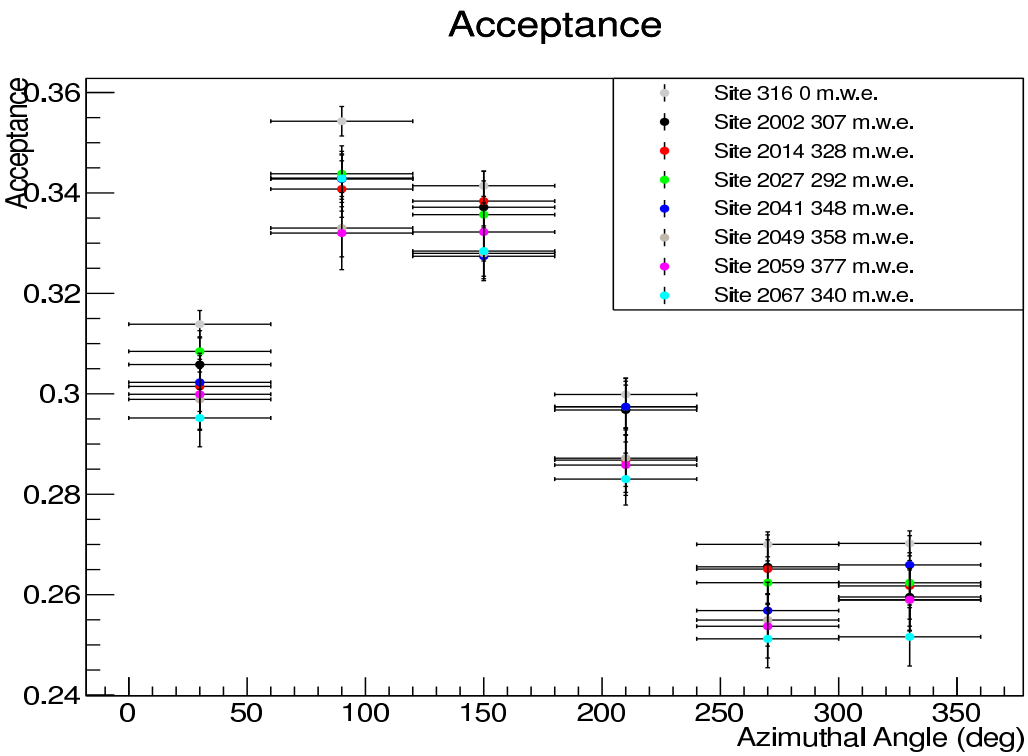

Figure 4.7: Azimuthal angle geometrical accptance of the detector.

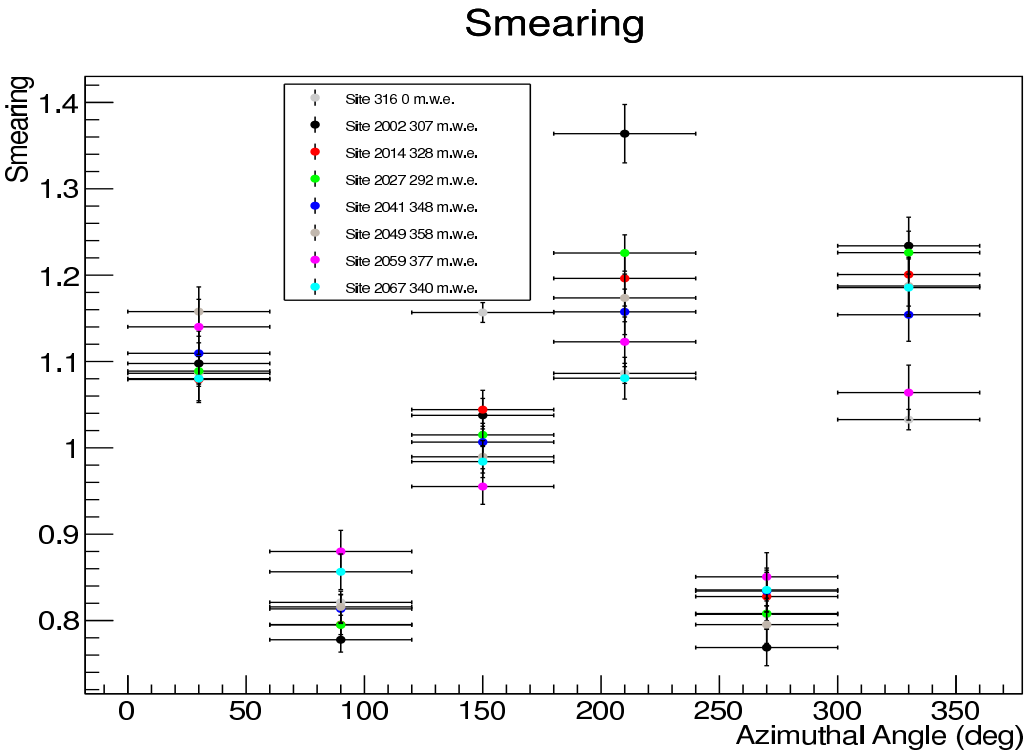

Figure 4.8: Azimuthal angle smearing effect of the detector.

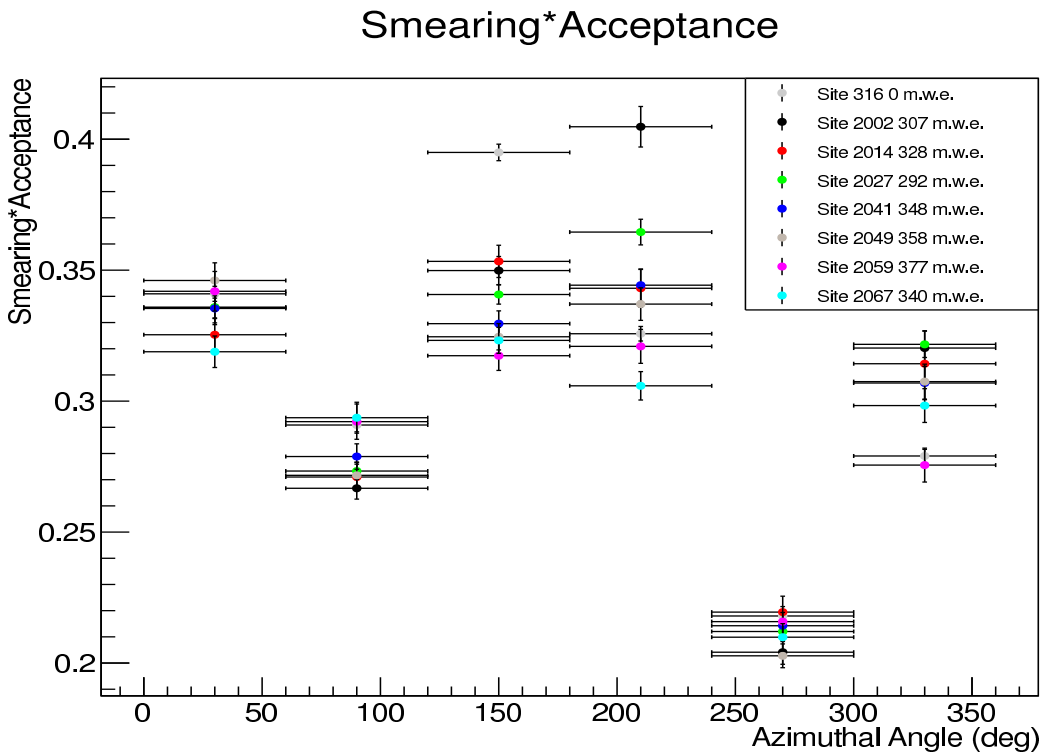

Figure 4.9: Azimuthal angle product of geometrical acceptance and smearing effect.

4.3.1 Surface Data (Room 316)

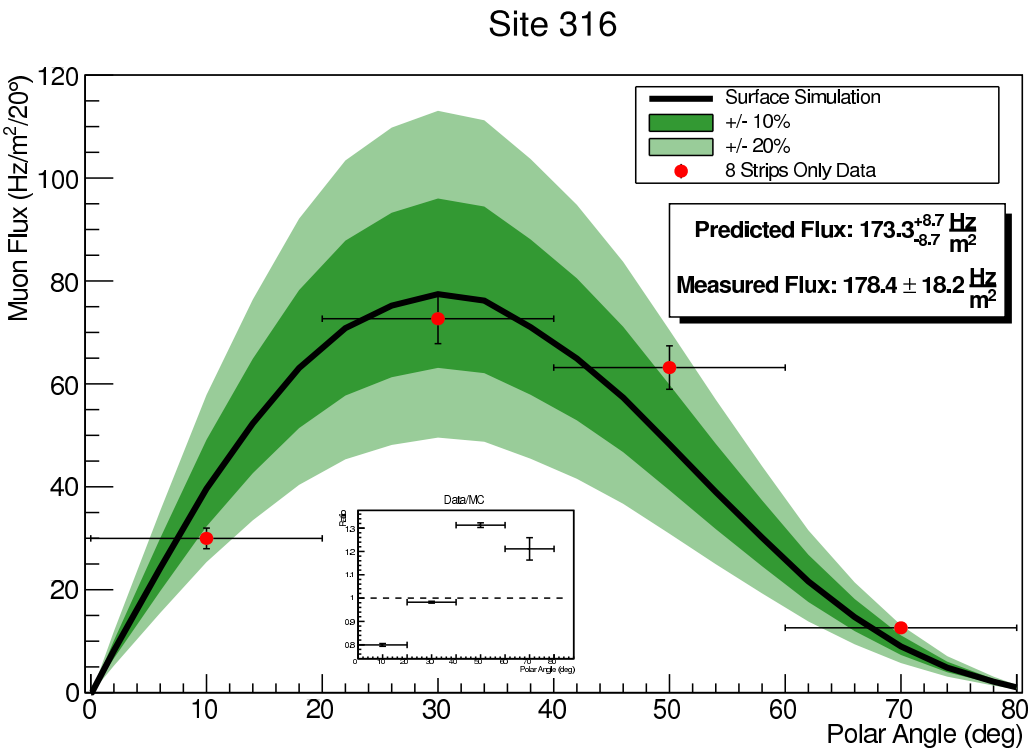

Figure 4.10: Polar angle reconstruction on the surface.

Before taking the detector into the mine we first took data in Room 316 of Robeson Hall on the Virginia Tech campus. The overall distribution of cosmic muons at the surface [9] is known to be proportional to $\cos^2\theta$ where θ is the angle relative to the vertical. Since our detector has a flat surface we include an additional factor of $\cos\theta$ in the expected cosmic muon flux. The distribution of cosmic muons is assumed to be isotropic in the azimuthal angle.

When the corrections for smearing and acceptance are applied to the data taken from the surface we find that the integrated flux is significantly below the prediction. We assume that the discrepancy is due to gamma rays entering the detector. Gamma rays originate from cosmic ray showers as well as radioactive impurities present in various materials located in Robeson Hall. Gamma ray contamination does not appreciably affect the measurement of the muon rate since gamma rays are not able to cause hits above threshold in 8 overlapping strips. The angular reconstruction is significanly affected since we only reconstruct events with only 8 strips hit. We reconstruct events with 8 hit strips only because we don't take into account for events that contain muons and gamma rays in our Monte Carlo simulations. To correct for this we apply a correction factor uniformly to all angular bins. The factor is calculated as the ratio of the number of events with only 8 strips hit to the total number

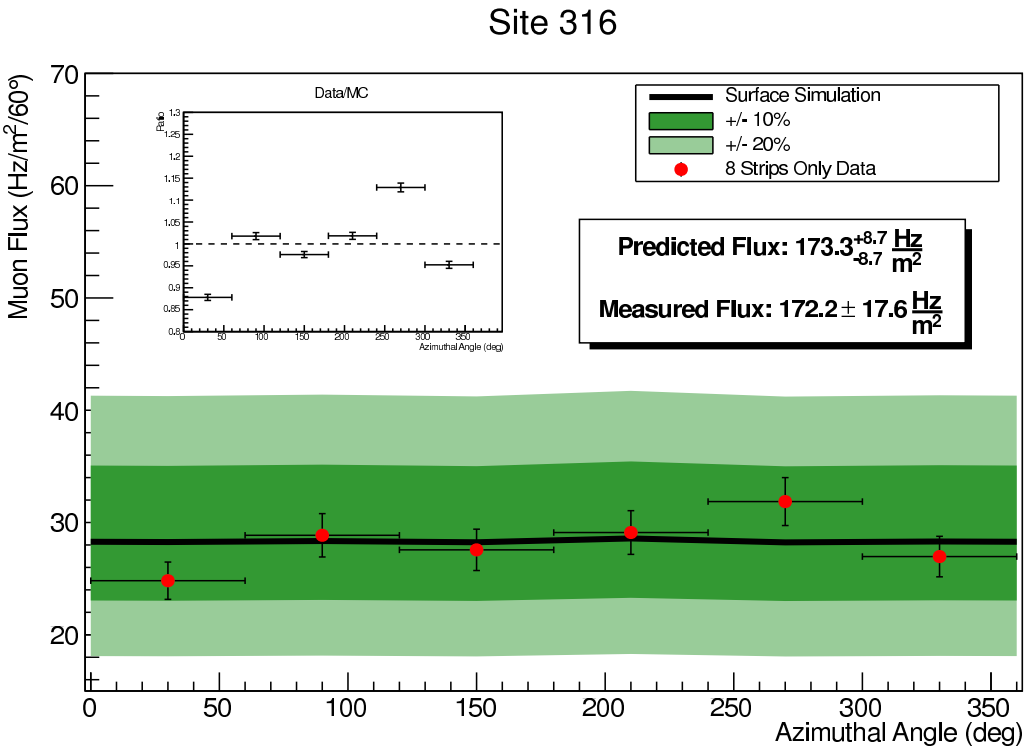

Figure 4.11: Azimuthal angle reconstruction on the surface.

of muon events. For the data taken in Room 316 the correction factor was 0.606. With the correction factor applied, along with the purity, acceptance, and smearing corrections, the data becomes in good agreement with the prediction.

4.3.2 Underground Measurements

Level 2 of the mine has no power source that can be tapped to run the detector and its modules. A diesel generator connected to a back-up battery was used to run the detector and would provide power for up to 17 hours at a time. Portable HV and LV modules were used to power the MAPMTs which are responsible for the different gain constants used in the level 2 rate measurements.

For most of the sites underground there is good agreement between the MUSIC prediction and the polar angle reconstruction, but there are significant deviations between the MUSIC prediction and the azimuthal reconstruction in some angular bins at all of the sites. While the integrated flux at each site is in good agreement with the prediction, the deviations in the various angular bins can be explained by a combination of factors.

Inside the mine on level 2 the various sites were identified by markers which were spray

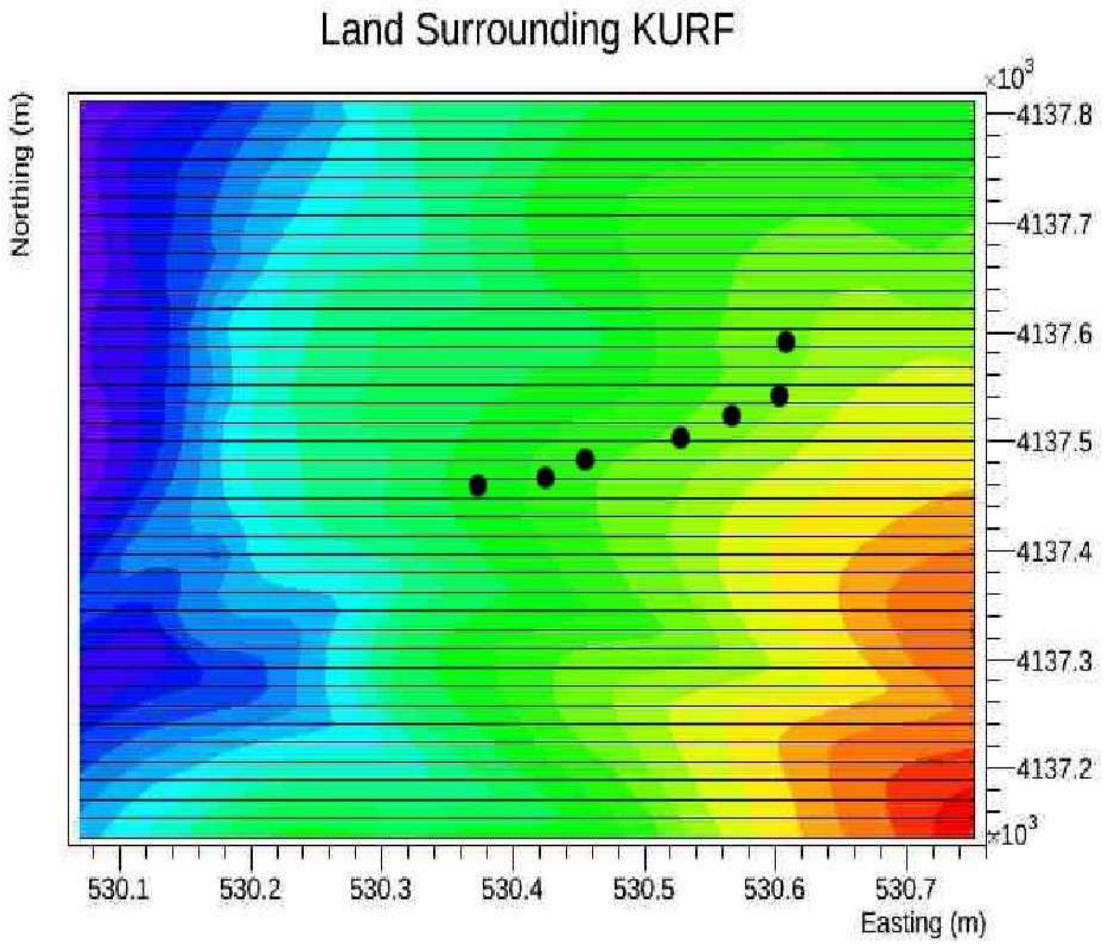

Figure 4.12: Overview of the land above the Level 2 sites. The leftmost point is site 2002 and the site numbers increase to the right.

painted onto the ground. Level 2 has two main roadways in the areas that the detector was placed with lage support columns separating the roadways. The spaces between the columns are large enough to drive mine vehicles through. For many of the sites the detector could not be placed exactly on the marker since the level 2 road had to be kept clear to allow the transit of mine vehicles. Because of this, the vertical overburden could be different by up to 5%.

Another significant source of error is the fact that the detector rests on a cart that is close to the floor, and the hallways that comprise level 2 of the mine have ceilings as high as 10 m. The path lengths used as inputs to MUSIC are based on the vertical overburden at the particular site as given in the survey as shown. The flux in a direction along the road would be higher than the prediction due to the reduced path length through the rock. In contrast, a reduced flux would be expected in the direction of a column due to the increase

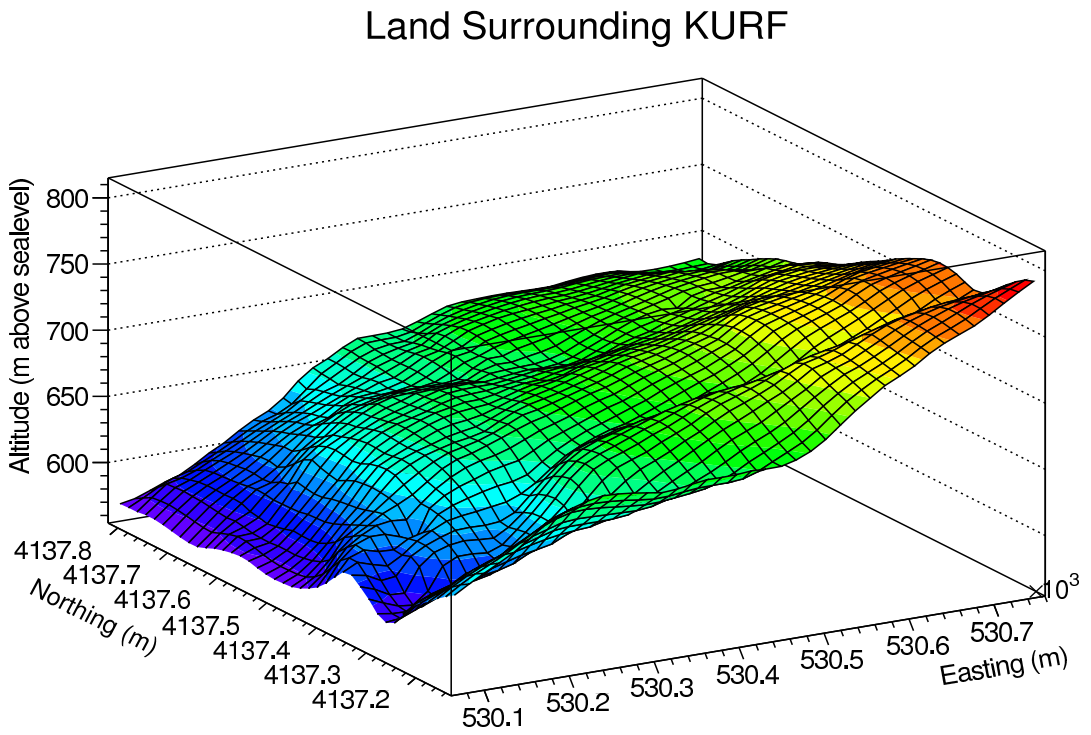

Figure 4.13: Elevation plot of the land above the Level 2 sites.

in path length through the rock.

Overburden Calculations Based on Lidar Surface Information & Field Survey Data Note: Overburden Calculated Between Surface Elevation and Ceiling Elevation					
Point #	Floor Elevation	Ceiling Elevation	Surface Elevation	Overburden (ft)	Overburden (m.w.e.)
Level 2 East					
2002	1843.51	1867.14	2240.16	373.02	306.9
2014	1843.44	1881.17	2280.04	398.87	328.2
2027	1845.16	1941.09	2296.39	355.30	292.3
2041	1844.20	1879.13	2301.79	422.66	347.7
2049	1845.57	1880.50	2315.33	434.83	357.8
2059	1847.75	1873.38	2331.60	458.22	377.0
2067	1853.58	1913.41	2326.87	413.46	340.2

Figure 4.14: Survey Data of the Rock Overburden at the Kimballton Limestone Mine.

Also, while an average rock density is used in the simulation, the different strata that make up the mountain will have different individual densities. The flux in an angular bin would be reduced if there was a significant path length through a rock of higher density than limestone. A large part of the overburden at polar angles less than 40° is composed of Martinsburg Formation shale which has a dry density [145] of 2.74 g/cm^3, while the average density of the limestone is 2.69 g/cm^3.

Site 2002 (307 m.w.e)

Site 2002 is near the entrance to Level 2 of the mine and is situated in a small alcove just off of the road. The northward direction was toward the alcove with the road running in the East-West direction. The ceiling is roughly 10 m high on Level 2 and the cavity formed by the road will result in a lower path length through rock. This can be seen noting that the measured azimuthal fluxes in the bins 0°-60° and 120°-180° are significantly above the MUSIC prediction. The reduced flux in the 60°-120° azimuthal angle bin is likely due to the wall to the north of the site. The reduced fluxes in the 180°-240° and 300°-360° azimuthal bins are likely due to the presence of two large support columns in those directions. A short hallway in the southward direction can explain why the flux in the 240°-300° is closer to the prediction.

Site 2014 (328 m.w.e.)

Site 2014 is located in the middle of the road about 50 m east of site 2002 farther into the mine. The detector was placed against the northeast edge of the column located to the immediate southwest of site 2014. The hallway proceeds to the northeast of this location and can explain the larger measured fluxes in the 0°-60° and 60°-120° bins. There is only a

small section of hallway to the northwest of the detector location and this is likely why the measured flux is in good agreement with the prediction in the 120°-180° bin. The measured fluxes are the lowest in the 180°-240° and 240°-300° bins because of the column against which it was placed. The measured flux in the 300°-360° bin is closer to the prediction because of the short section of hallway in that direction.

Site 2027 (292 m.w.e.)

Site 2027 is located in the middle of the road on level 2 about 41 m northeast of site 2014 and the detector was placed near the wall to the north of the site. At this location the hallway runs from the southwest to the northeast. This explains why the measured flux is near the prediction for the 0°-60° bin and why the measured fluxes are lowest in the 60°-120° and 120°-180° bins. The measured fluxes in the 180°-240° and 300°-360° bins are above the prediction because the largest open spaces in the hallway are in these directions. The short section of hallway to the south of site 2027 can explain why the flux measurement in the 240°-300° is in good agreement with the prediction.

While the measured muon rate was in agreement with the MUSIC prediction, the integrated flux from the reconstruction was significantly less than the predicted spectrum after correcting for acceptance and smearing. We assume gamma ray contamination from an unknown source, possibly nearby machinery, to be responsible for the deficit of events with only 8 strips hit. We uniformly correct each bin in both polar and azimuthal angles by the ratio of events with only 8 strips to the total number of events. This assumes that all events with more than 8 strips hit are contaminated. That is likely not the case since the corrected integrated flux is more than the predicted integrated flux by a greater margin than at any other site.

Site 2041 (348 m.w.e.)

Site 2041 is located approximately 75 m to the east of site 2027 and is marked in the middle of the roadway. The detector was placed to the southwest of site 2041 near the wall to the south to avoid mine traffic. The largest open section of hallway relative to this location is to the northeast direction which can contribute to the measured flux being significantly above the prediction in the 0°-60° bin. The column to the north of the detector is likely responsible for the measured flux in the 60°-120° bin being below the prediction. The hallway also has a large open section to the west of where the detector was placed which can explain why the measured flux in the 120°-180° bin is above the prediction. The wall to the immediate south of the detector location can explain why the measured fluxes in the 180°-240°, 240°-300°, and 300°-360° bins are below the prediction.

Site 2049 (358 m.w.e.)

Site 2049 is located approximately 40 m to the east of site 2041 and is marked near the middle of the roadway between two support columns. The detector was placed near the east face of the support column located to the west of site 2049. The largest opening in the hallway from this location is in the northeast direction which can explain why the measured fluxes in the 0°-60° and 60°-120° bins are above the prediction. The measured fluxes in the 120°-180° and 180°-240° bins are below the prediction and this can be explained by the the column directly to the west of the detector. The short section of hallway to the south and southeast can explain why the measured fluxes in the 240°-300° and 300°-360° bins are below the prediction.

Site 2059 (377 m.w.e.)

Site 2059 is located approximately 43 m to the northeast of site 2049 and is marked in the middle of a relatively open section of level 2. The detector was placed to the east of the marker and just south of the nearest support column to avoid mine vehicle traffic. The large open space to the northeast is likely responsible for the measured flux in the 0°-60° bin being significantly above the prediction. The column to the north is smaller than the typical column on level 2 and can explain why the measured flux in the 60°-120° bin is slightly lower than the prediction. The column to the southwest and the wall to the south can explain why the measured fluxes in the 180°-240° and 240°-300° bins are below the prediction. The hallway has a small open section to the southeast of the detector which can explain why the measured flux is close to the prediction.

Site 2067 (340 m.w.e.)

Site 2067 is located approximately 40 m to the north of site 2059 near large explosives magazines made of steel. While the site is marked to the west of the magazines, the detector was placed behind the magazines to the east of the marker. The hallway opens up to the northeast which explains the measured flux being above the prediction in the 0°-60° bin. The measured flux in the 60°-120° bin is significantly above the prediction despite a wall to the north of the detector location. This can be attributed to a difference in the mountain profile since the depth of the overburden changes significantly from the marked location of site 2067 to the point where the detector was placed. The flux measured in the 120°-180° bin is lower than the prediction most likely because of the presence of the explosives magazines located to the west of the detector. They have a much higher average density than the surrounding rock and will stop muons more readily. Support columns located to the southeast and southwest of the detector can explain why the measured fluxes in the 180°-240° and 300°-360° bins are lower than the prediction. The small opening of the hallway to the south of the detector can explain why the flux in the 240°-300° bin is closer to the prediction.

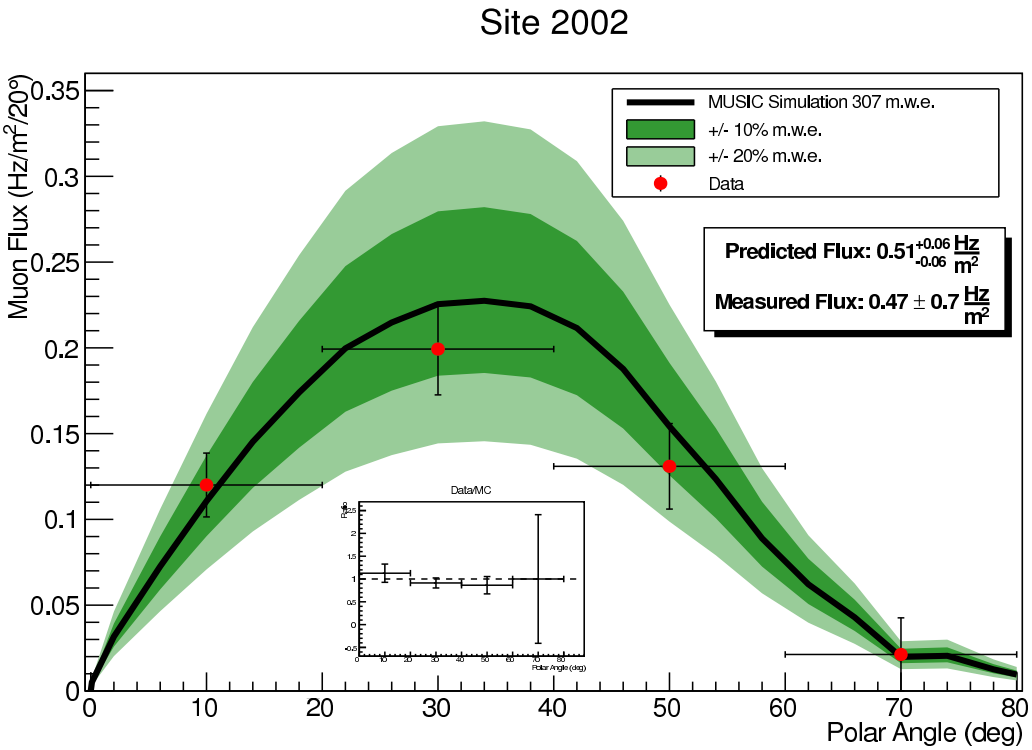

Figure 4.15: Polar angle reconstruction at site 2002.

4.4 Summary

We performed a fit in which vertical overburden is compared to muon flux using a well known 3 parameter formula [146]

$$I_\mu(x) = A\frac{x_0}{x}^{\alpha} e^{-\frac{x}{x_0}} \tag{4.3}$$

where α is a dimensionless number, x_0 is in m.w.e., and A as units of Hz/m^2. The minimum χ^2 fit yeilds

$$A = 0.033 \ \pm \ 0.028 \ Hz/m^2 \qquad \alpha = 1.91 \ \pm \ 0.44 \qquad x_0 = 1483 \ \pm \ 552 \ m.w.e.$$

This function, along with the data, is shown in Fig. 4.29.

As a consistency check, simulations were performed assuming the land above the detector is either flat or a perfect mountain, where a perfect mountain is defined to be a hemisphere with the detector at the center. We assume that the real mountain profile would yield a flux somewhere between these two cases. The results are shown in Fig. 4.30.

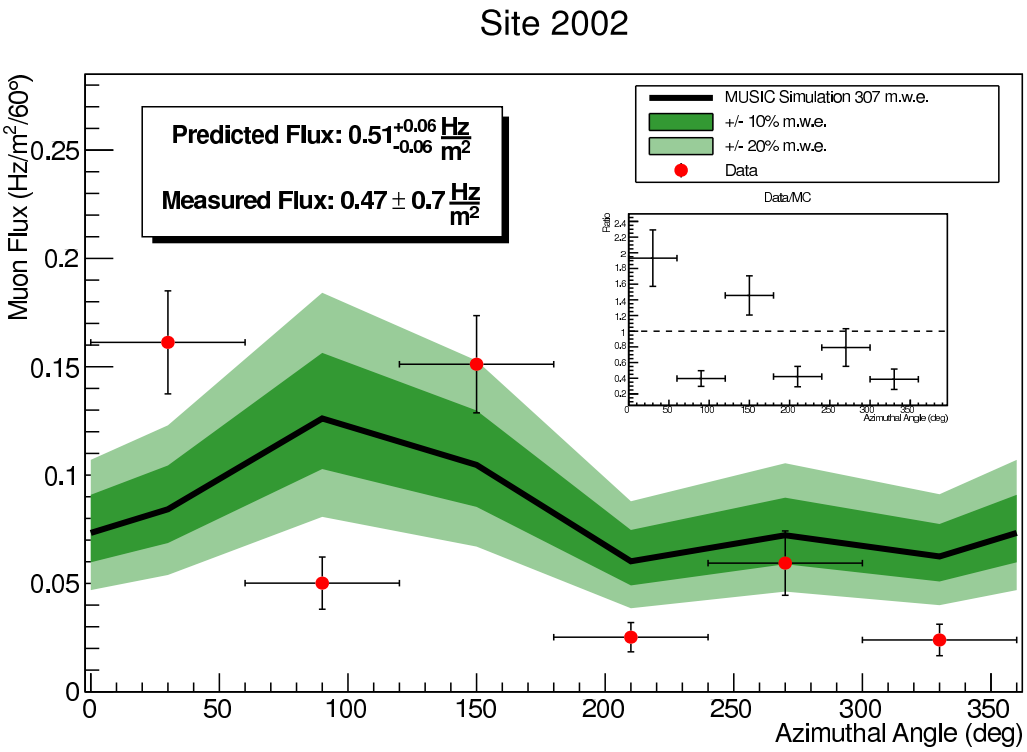

Figure 4.16: Azimuthal angle reconstruction at site 2002.

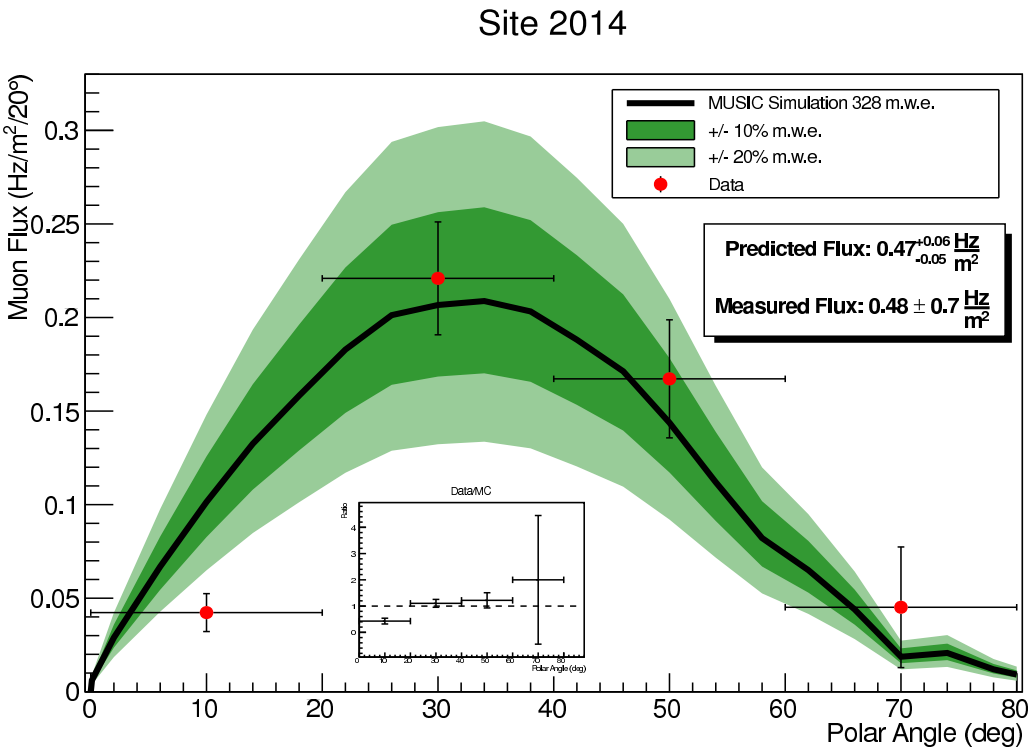

Figure 4.17: Polar angle reconstruction at site 2014.

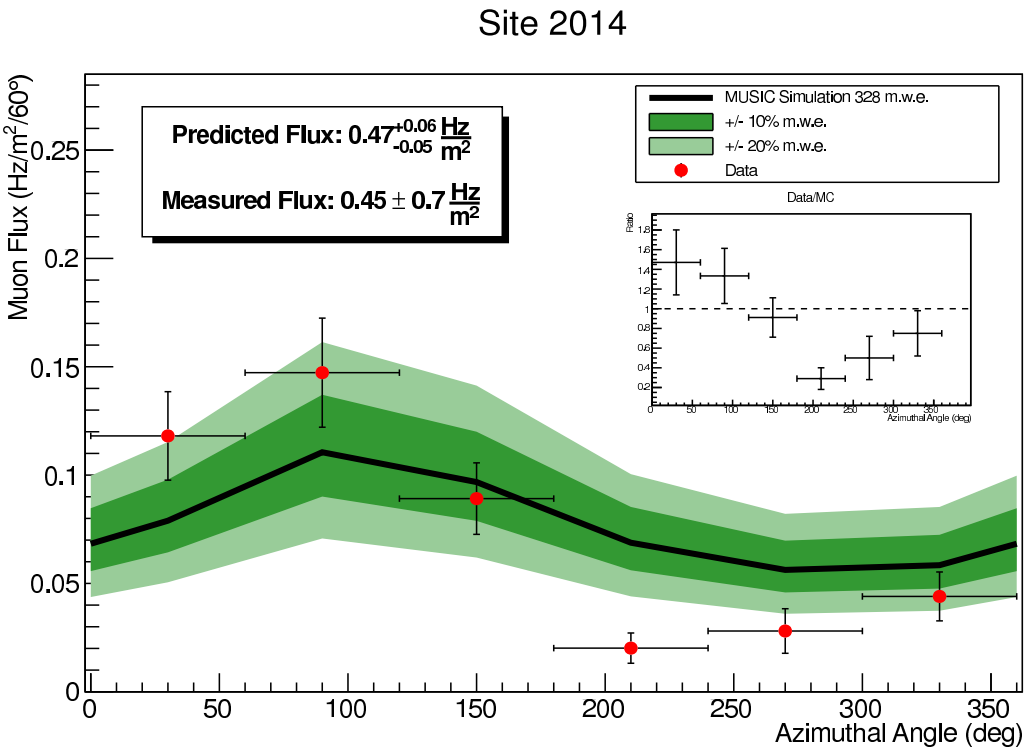

Figure 4.18: Azimuthal angle reconstruction at site 2014.

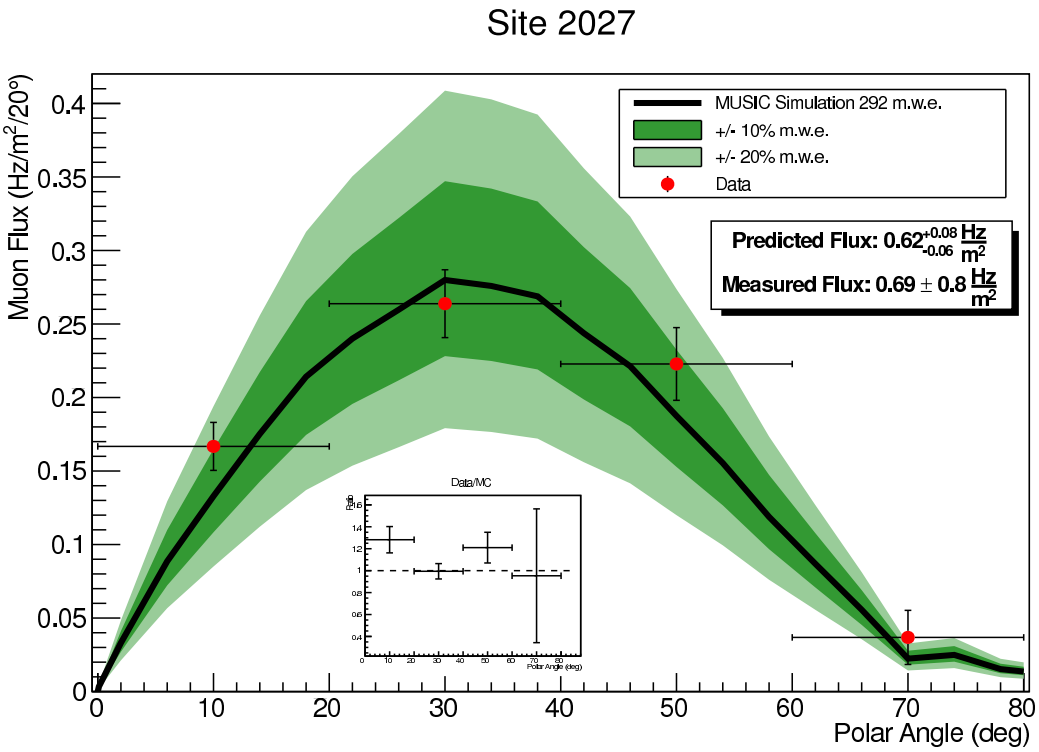

Figure 4.19: Polar angle reconstruction at site 2027. A correction factor was applied to account for sample contamination.

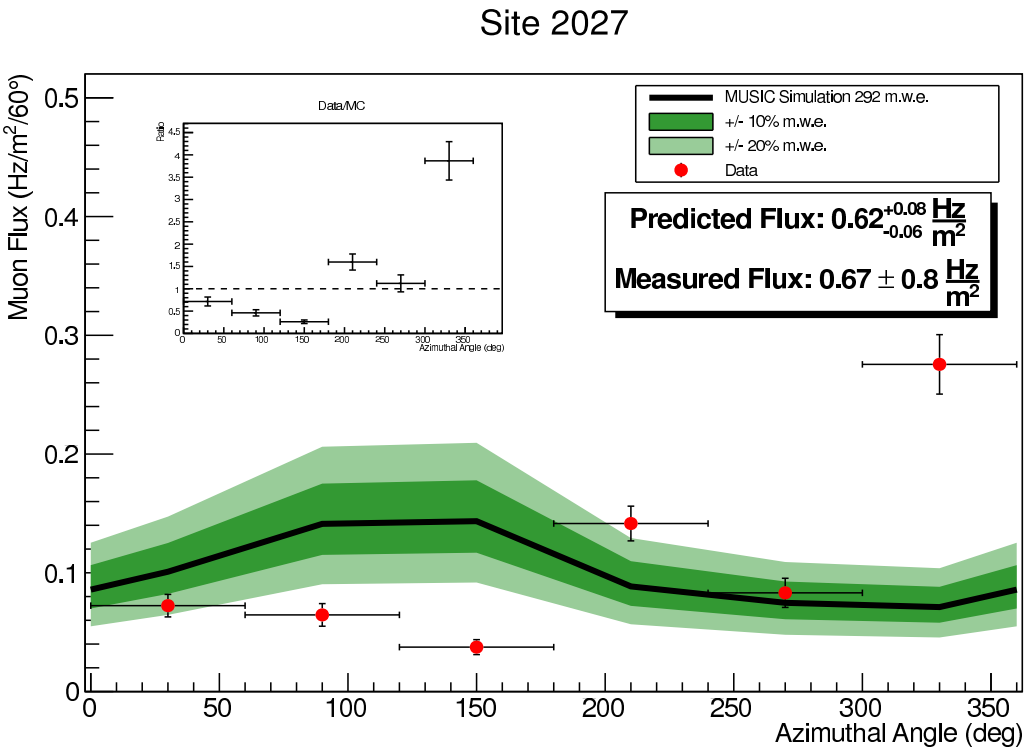

Figure 4.20: Azimuthal angle reconstruction at site 2027. A correction factor was applied to account for sample contamination.

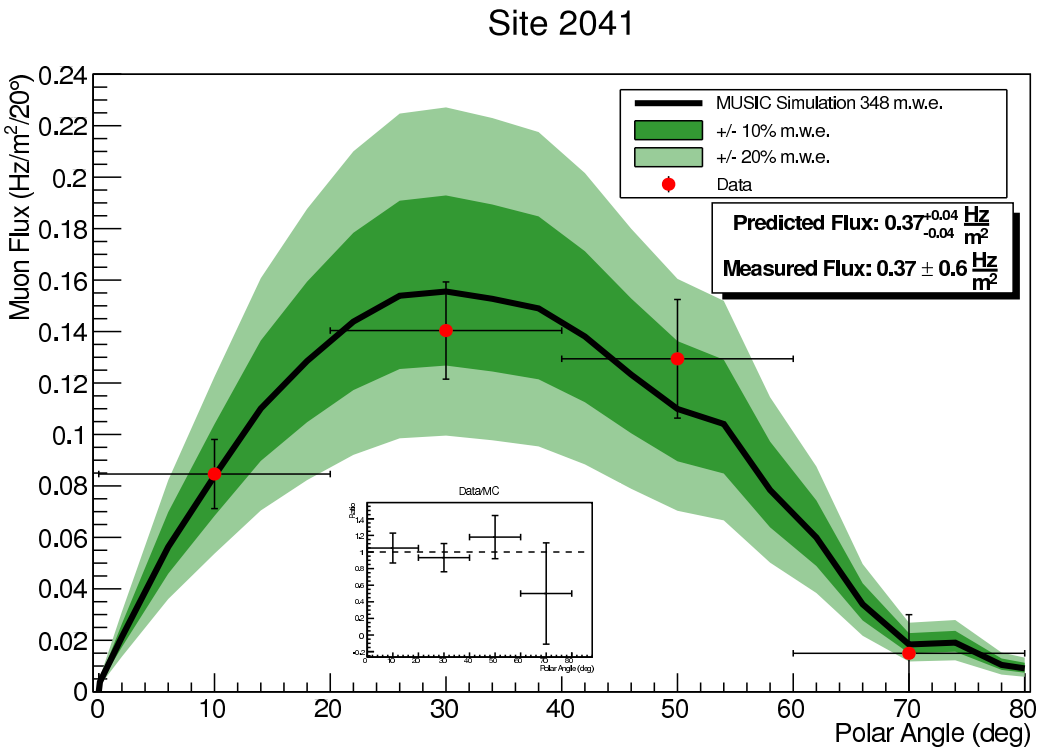

Figure 4.21: Polar angle reconstruction at site 2041.

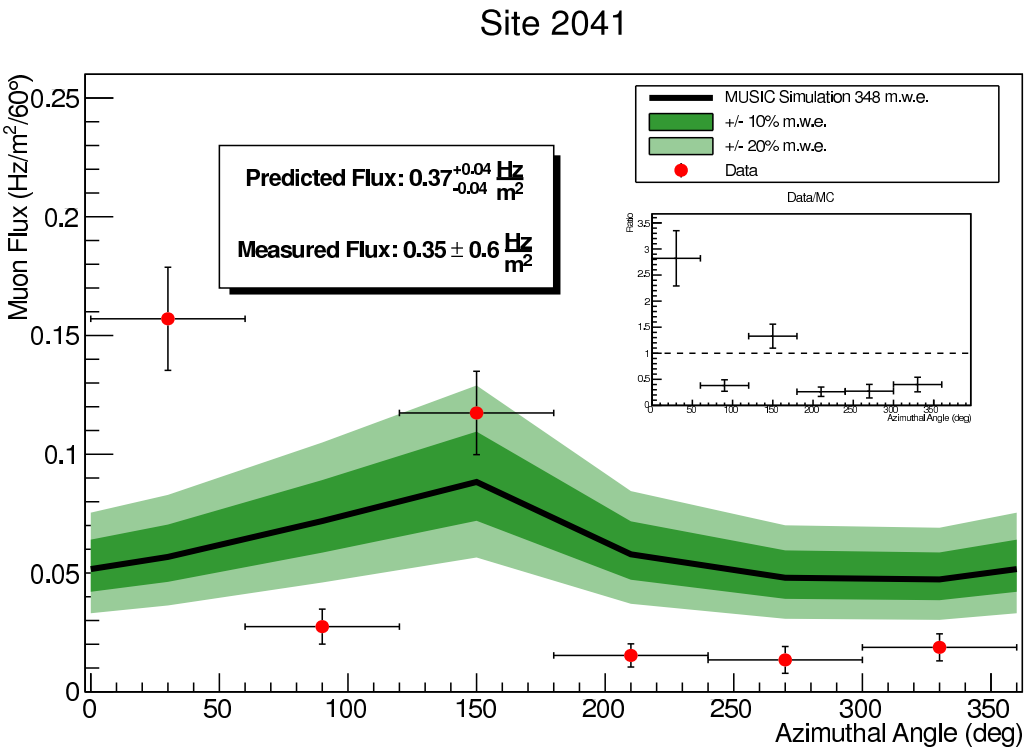

Figure 4.22: Azimuthal angle reconstruction at site 2041.

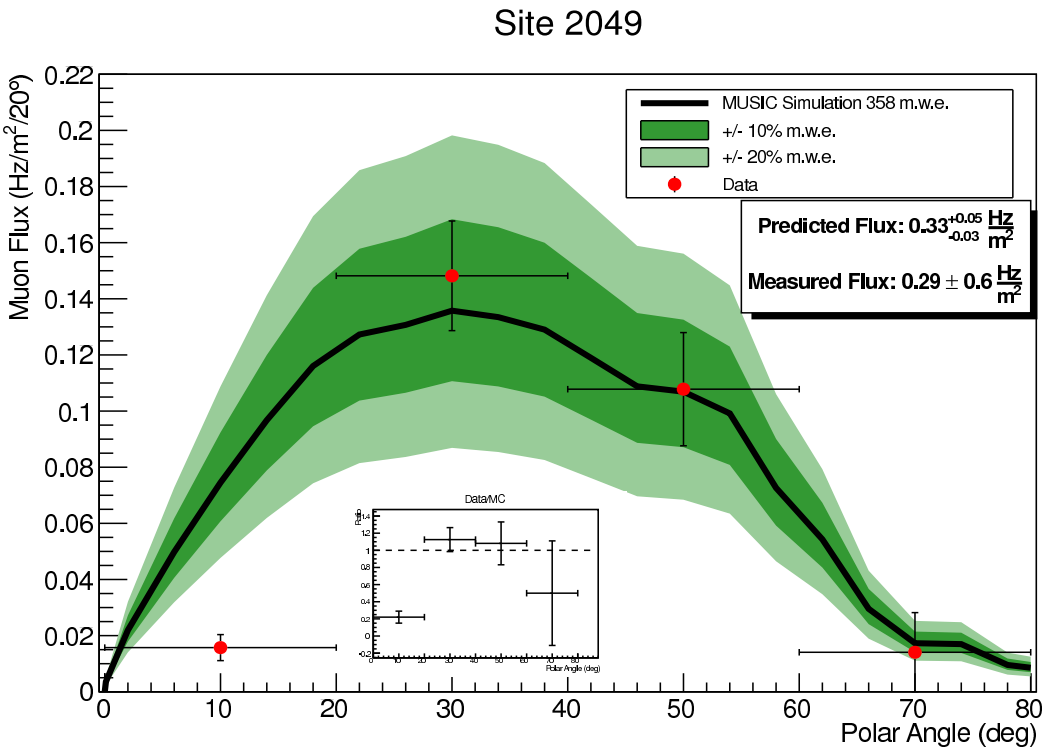

Figure 4.23: Polar angle reconstruction at site 2049.

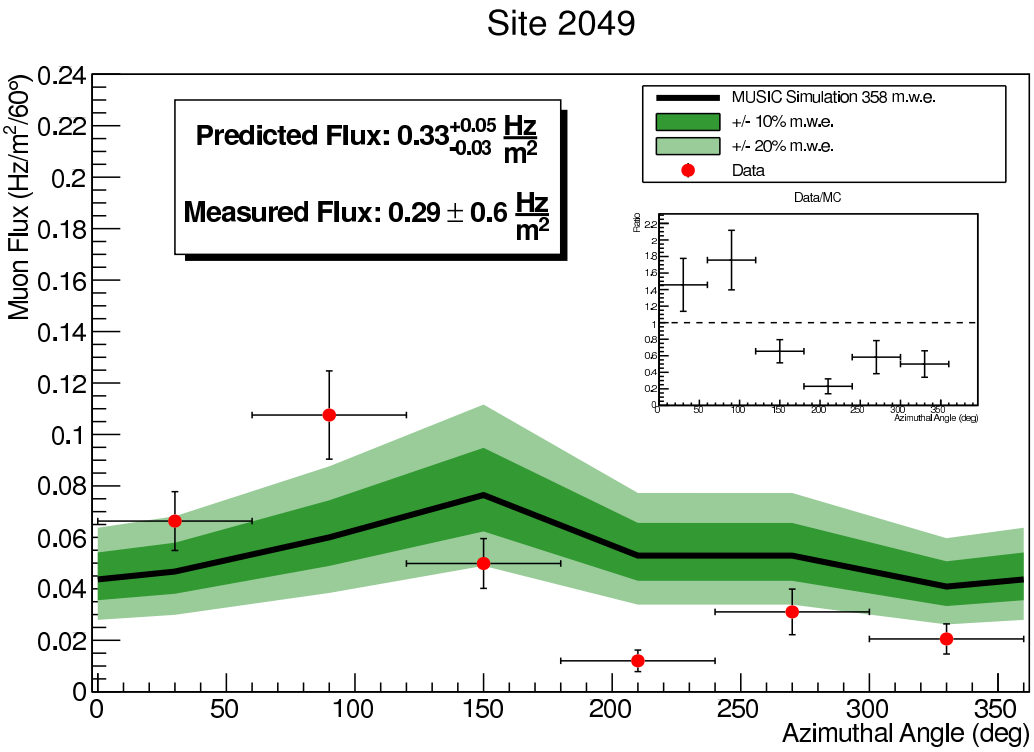

Figure 4.24: Azimuthal angle reconstruction at site 2049.

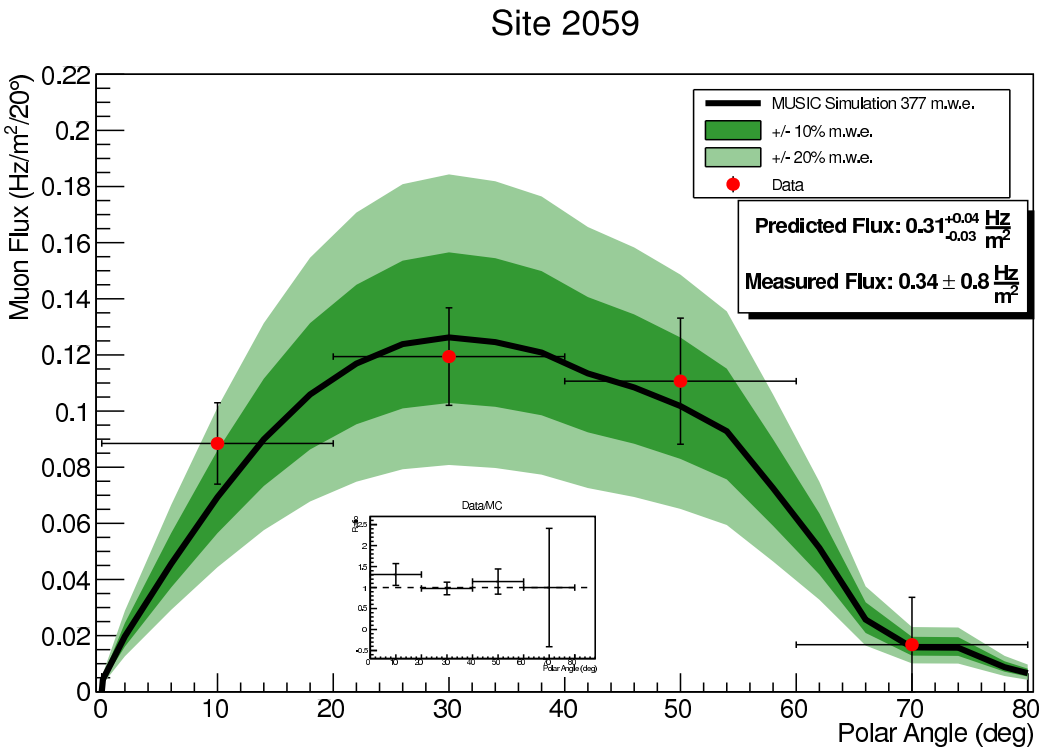

Figure 4.25: Polar angle reconstruction at site 2059.

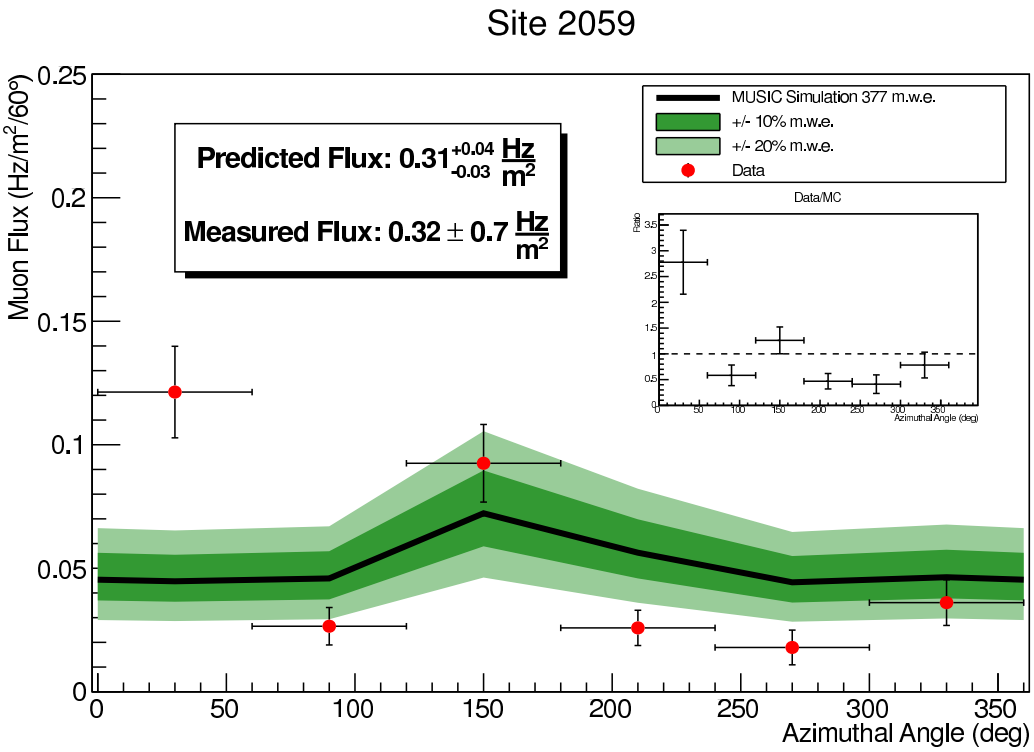

Figure 4.26: Azimuthal angle reconstruction at site 2059.

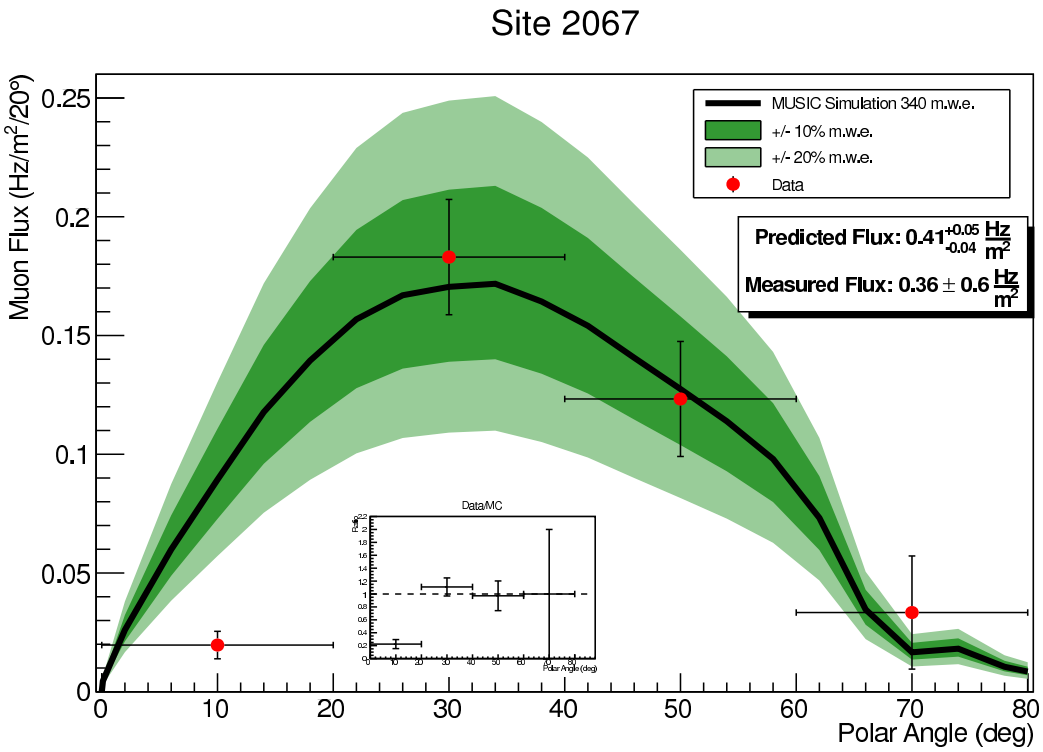

Figure 4.27: Polar angle reconstruction at site 2067.

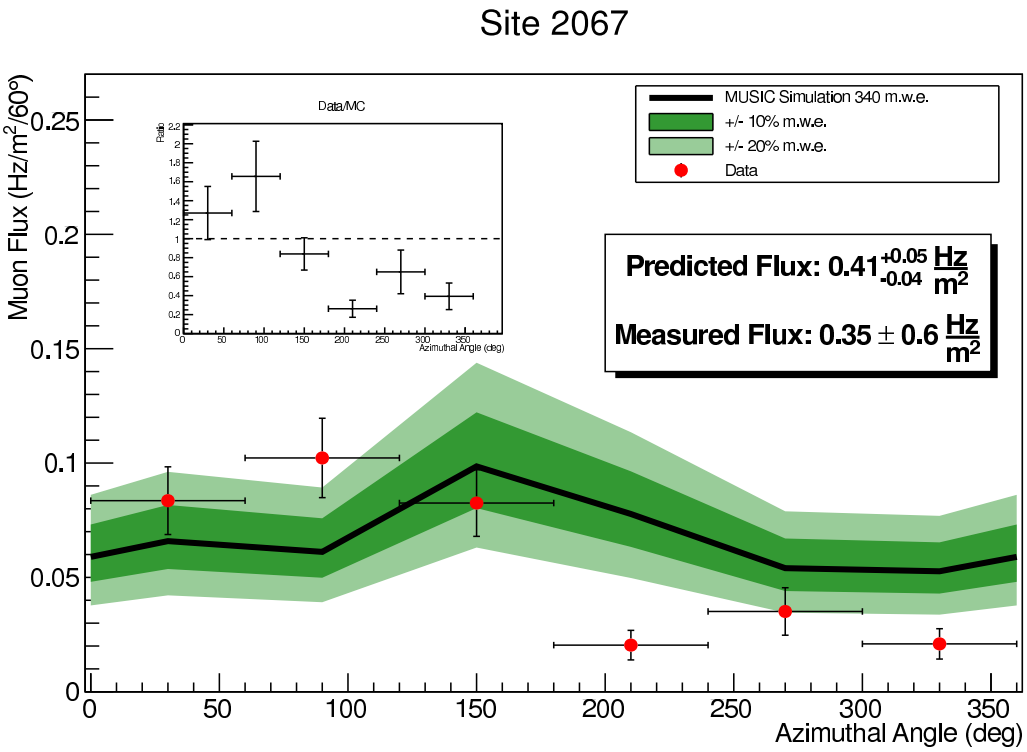

Figure 4.28: Azimuthal angle reconstruction at site 2067.

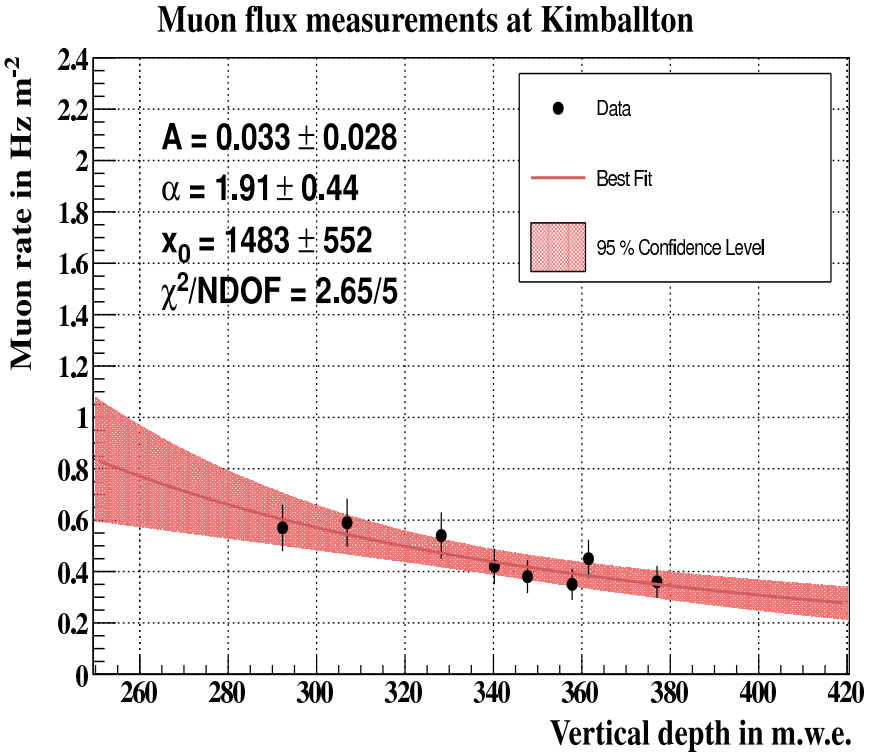

Figure 4.29: Muon flux predictions and measurements for the Level 2 sites. The error band is obtained by propagating the errors on the parameters from the fit. Figure from Ref. [8]

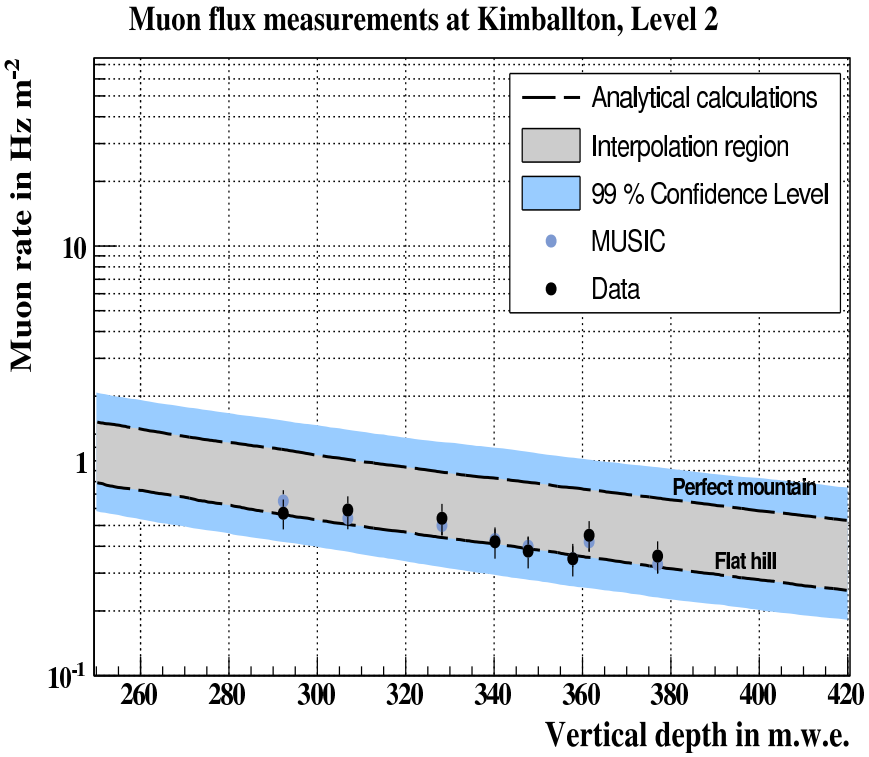

Figure 4.30: Muon flux predictions and measurements for the Level 2 sites. Figure from Ref. [8]

Chapter 5

Conclusion

The measurements of the cosmic muon flux at the various sites on Level 2 of KURF were generally in good agreement with the prediction of the simulation and the surface measurement was in very good agreement with the prediction. This was true for the rate measurements with events that had at least 8 overlapping hits and for the corrected rate measurements using reconstructed events that had 8 hits only. Because of this we can conclude that the MUSIC simulation technique using accurate elevation data is a fairly accurate tool to simulate the flux of cosmic muons at underground sites. At most sites, the polar angular reconstruction was in good agreement with the MUSIC prediction with the most variation being present for vertical muons. These variations can be attributed to nearby columns or differences in overburden between where the detector was placed and the site locations. The azimuthal reconstruction suffered from significant differences with the MUSIC prediction, despite the integrated flux from the azimuthal angular reconstruction being within error of the MUSIC prediction, while the azimuthal angular reconstruction of the data from the surface shows small variations from isotropy. These results suggest that the formations near the detector such as columns, outcroppings, or walls, can significantly affect the measured flux in the direction of the obstacle. If used for future measurements, a visit to the site before the detector is deployed could yield important information that can be used to more accurately model the flux.

The detector was found to be fairly efficient at detecting cosmic muons but it has a poor angular resolution, especially for vertical muons. The reconstruction procedure consists of finding the best fit tracks for the x and y bilayers. We assume that a strip was hit along the axis that contains the optical fiber and we use the best fit tracks in each bilayer to compute the angles of the best fit track in three dimensions. The angular resolution was determined by two additional factors: the size of the strips relative to the detector size, and their arrangement in the detector. If strips with smaller widths were used, a detector with the same effective area would have a finer angular resolution because a muon passing through would have more possible strip combinations through which to pass. Since the strips could

have been cut to be longer, a larger detector with strips that had the same width as the original detector would also have better angular resolution for the same reason. Either of these changes would have resulted in more angular resolution at polar angles less than 50° for which the flux is highest. The strips, in fact, were arranged in the detector in such a way that the ones on the top layer of a single bilayer were offset by half of the width of a strip, as described in Chapter 3. This configuration greatly reduced the likelihood that a muon could pass through only dead space on its way through a bilayer but also resulted in a significant smearing of the reconstructed angles of vertical muons. Instead of having layers that are 4.5 strips wide and offsetting successive layers, the detector could have been designed with layers that are exactly 4 strips wide with strips from the top layer of the bilayer directly on top of the corresponding strips from the bottom bilayer. This configuration would likely also have poor resolution, but would result in less smearing when reconstructing vertical muons. Ultimately, I would have taken data with the detector in both configurations and combined the results. A possibility that was considered for the proposed muon telescope described in Chapter 2 but was never considered for the MM was performing the measurements with an adjustable separation between the top two bilayers and the bottom two bilayers. This would have resulted in a higher angular resolution but a lower angular acceptance. Trials would then be conducted to determine the ideal separation to achieve the highest angular resolution in the polar angle range with the largest flux. Another limitation was the time for which the detector was available to take data. The problem was that the detector was deployed on a level of the mine that is not served by power so a diesel generator was used to power the detector and that would allow for almost 24 hours of continuous data taking at most. Also, data was taken only once at each site on level 2. In addition to taking data for a longer duration more than once at each site, I would have liked to rotate the detector in between data taking sessions. A compass was used to ensure that the detector was always facing the same way for each site. I would have liked to compare two sets of data taken at the same site with the orientation of the detector different by 180° to see specifically how the measured azimuthal angle distribution of muons would have changed.

Bibliography

[1] F. Reines and C. Cowan. The Reines-Cowan experiments: Detecting the Poltergeist. *Los Alamos Sci.*, 25:4–27, 1997.

[2] M. Strassler. How to make a neutrino beam, September 2011. http://profmattstrassler.com/2011/09/23/how-to-make-a-neutrino-beam/.

[3] John N. Bahcall, Aldo M. Serenelli, and Sarbani Basu. New solar opacities, abundances, helioseismology, and neutrino fluxes. *Astrophys.J.*, 621:L85–L88, 2005.

[4] Q. R. Ahmad et al. Direct evidence for neutrino flavor transformation from neutral-current interactions in the sudbury neutrino observatory. *Phys. Rev. Lett.*, 89:011301, Jun 2002.

[5] C. D. Dermer. Secondary production of neutral pi-mesons and the diffuse galactic gamma radiation. , 157:223–229, March 1986.

[6] KURARAY CO. LTD. Plastic Scintillating Fibers. http://kuraraypsf.jp/psf/index.html.

[7] Mark Lawrence. Three Dimensional Boundary Value Problems in Spherical Coordinates, April 2005. http://quantumrelativity.calsci.com/Physics/EandM8.html.

[8] L.N. Kalousis, E. Guarnaccia, J.M. Link, C. Mariani, and R. Pelkey. Cosmic Muon Flux Measurements at the Kimballton Underground Research Facility. *submitted to JINST*, 2014.

[9] T.K. Gaisser. Cosmic rays and particle physics. 1990.

[10] S.L. Glashow. Partial Symmetries of Weak Interactions. *Nucl.Phys.*, 22:579–588, 1961.

[11] Steven Weinberg. A Model of Leptons. *Phys.Rev.Lett.*, 19:1264–1266, 1967.

[12] David J. Gross and Frank Wilczek. Ultraviolet Behavior of Nonabelian Gauge Theories. *Phys.Rev.Lett.*, 30:1343–1346, 1973.

[13] D. Hanneke, S. Fogwell, and G. Gabrielse. New Measurement of the Electron Magnetic Moment and the Fine Structure Constant. *Phys.Rev.Lett.*, 100:120801, 2008.

[14] D. Hanneke, S. Fogwell Hoogerheide, and G. Gabrielse. Cavity Control of a Single-Electron Quantum Cyclotron: Measuring the Electron Magnetic Moment. 2010.

[15] Michael B. Green, J.H. Schwarz, and Edward Witten. SUPERSTRING THEORY. VOL. 1: INTRODUCTION. *Cambridge Monogr.Math.Phys.*, 1987.

[16] G. Veneziano. Construction of a crossing - symmetric, Regge behaved amplitude for linearly rising trajectories. *Nuovo Cim.*, A57:190–197, 1968.

[17] Leonard Susskind. Harmonic-oscillator analogy for the veneziano model. *Phys.Rev.Lett.*, 23:545–547, 1969.

[18] Bohdan Paczynski. Gravitational microlensing by the galactic halo. *Astrophys.J.*, 304:1–5, 1986.

[19] K. Griest. Detecting dark matter via microlensing. *AIP Conf.Proc.*, 243:1080–1085, 1992.

[20] Albert Einstein. Cosmological Considerations in the General Theory of Relativity. *Sitzungsber.Preuss.Akad.Wiss.Berlin (Math.Phys.)*, 1917:142–152, 1917.

[21] Varun Sahni, Andrzej Krasinski, and Ya.B. Zeldovich. Republication of: The cosmological constant and the theory of elementary particles (By Ya. B. Zeldovich). *Sov.Phys.Usp.*, 11:381–393, 1968.

[22] A. Davour. The PICASSO dark matter search project. *PoS*, IDM2008:010, 2008.

[23] R. Bernabei, Pierluigi Belli, F. Cappella, R. Cerulli, F. Montecchia, et al. Dark matter search. *Riv.Nuovo Cim.*, 26N1:1–73, 2003.

[24] Adam G. Riess et al. Observational evidence from supernovae for an accelerating universe and a cosmological constant. *Astron.J.*, 116:1009–1038, 1998.

[25] S. Perlmutter et al. Measurements of Omega and Lambda from 42 high redshift supernovae. *Astrophys.J.*, 517:565–586, 1999.

[26] B. Pontecorvo. Neutrino Experiments and the Problem of Conservation of Leptonic Charge. *Sov.Phys.JETP*, 26:984–988, 1968.

[27] W. Pauli. Dear radioactive ladies and gentlemen. *Phys.Today*, 31N9:27, 1978.

[28] E. Fermi. An attempt of a theory of beta radiation. 1. *Z.Phys.*, 88:161–177, 1934.

[29] C.D. Ellis and W.A. Wooster. The Average Energy of Disintigration of Radium E. *Nature*, 119:563–564, 1927.

[30] F. Reines and C.L. Cowan. Free anti-neutrino absorption cross-section. 1: Measurement of the free anti-neutrino absorption cross-section by protons. *Phys.Rev.*, 113:273–279, 1959.

[31] F. Reines and C.L. Cowan. A Proposed experiment to detect the free neutrino. *Phys.Rev.*, 90:492–493, 1953.

[32] C.L. Cowan, F. Reines, F.B. Harrison, E.C. Anderson, and F.N. Hayes. Large liquid scintillation detectors. *Phys.Rev.*, 90:493–494, 1953.

[33] C.L. Cowan, F. Reines, F.B. Harrison, H.W. Kruse, and A.D. McGuire. Detection of the free neutrino: A Confirmation. *Science*, 124:103–104, 1956.

[34] F. Reines, C.L. Cowan, F.B. Harrison, A.D. McGuire, and H.W. Kruse. Detection of the free anti-neutrino. *Phys.Rev.*, 117:159–173, 1960.

[35] nobelprize.org. Press Release: The 1995 Nobel Prize in Physics, May 2014. http://www.nobelprize.org/nobel_prizes/physics/laureates/1995/press.html.

[36] C.S. Wu, E. Ambler, R.W. Hayward, D.D. Hoppes, and R.P. Hudson. Experimental Test of Parity Conservation in Beta Decay. *Phys.Rev.*, 105:1413–1414, 1957.

[37] M. Goldhaber, L. Grodzins, and A.W. Sunyar. Evidence for Circular Polarization of Bremsstrahlung Produced by Beta Rays. *Phys.Rev.*, 106:826–828, 1957.

[38] M. Goldhaber, L. Grodzins, and A.W. Sunyar. Helicity of Neutrinos. *Phys.Rev.*, 109:1015–1017, 1958.

[39] Jr. Davis, Raymond. Attempt to detect the antineutrinos from a nuclear reactor by the Cl37(anti-nu,e-) A37 reaction. *Phys.Rev.*, 97:766–769, 1955.

[40] R. Davis. Solar neutrinos. II: Experimental. *Phys.Rev.Lett.*, 12:303–305, 1964.

[41] B.T. Cleveland, Timothy Daily, Jr. Davis, Raymond, James R. Distel, Kenneth Lande, et al. Measurement of the solar electron neutrino flux with the Homestake chlorine detector. *Astrophys.J.*, 496:505–526, 1998.

[42] M. HAAG. Status of the KATRIN Experiment. *PoS*, EPS-HEP2013:518, 2014.

[43] Ariel Goobar, Steen Hannestad, Edvard Mortsell, and Huitzu Tu. A new bound on the neutrino mass from the sdss baryon acoustic peak. *JCAP*, 0606:019, 2006.

[44] G. Danby, J.M. Gaillard, Konstantin A. Goulianos, L.M. Lederman, Nari B. Mistry, et al. Observation of High-Energy Neutrino Reactions and the Existence of Two Kinds of Neutrinos. *Phys.Rev.Lett.*, 9:36–44, 1962.

[45] Marcela S. Carena, Andre de Gouvea, Ayres Freitas, and Michael Schmitt. Invisible Z boson decays at e+ e- colliders. *Phys.Rev.*, D68:113007, 2003.

[46] V. Barger, James P. Kneller, Hye-Sung Lee, Danny Marfatia, and Gary Steigman. Effective number of neutrinos and baryon asymmetry from BBN and WMAP. *Phys.Lett.*, B566:8–18, 2003.

[47] T.K. Gaisser and M. Honda. Flux of atmospheric neutrinos. *Ann.Rev.Nucl.Part.Sci.*, 52:153–199, 2002.

[48] D. Maurin, F. Melot, and R. Taillet. A database of charged cosmic rays. 2013.

[49] V.L. Ginzburg, V.A. Dogiel, V.S. Berezinsky, S.V. Bulanov, and V.S. Ptuskin. Astrophysics of cosmic rays. 1990.

[50] Andrew W. Strong, Igor V. Moskalenko, and Vladimir S. Ptuskin. Cosmic-ray propagation and interactions in the Galaxy. *Ann.Rev.Nucl.Part.Sci.*, 57:285–327, 2007.

[51] S. Fukuda et al. Solar B-8 and hep neutrino measurements from 1258 days of Super-Kamiokande data. *Phys.Rev.Lett.*, 86:5651–5655, 2001.

[52] Y. Fukuda et al. Evidence for oscillation of atmospheric neutrinos. *Phys.Rev.Lett.*, 81:1562–1567, 1998.

[53] Y. Takeuchi. Solar neutrino results from Super-Kamiokande. *Int.J.Mod.Phys.*, A18:3777–3787, 2003.

[54] Y. Fukuda et al. Measurement of a small atmospheric muon-neutrino / electron-neutrino ratio. *Phys.Lett.*, B433:9–18, 1998.

[55] K. Abe et al. A Measurement of atmospheric neutrino flux consistent with tau neutrino appearance. *Phys.Rev.Lett.*, 97:171801, 2006.

[56] Y. Fukuda et al. Study of the atmospheric neutrino flux in the multi-GeV energy range. *Phys.Lett.*, B436:33–41, 1998.

[57] C. Saji. Results from Super-Kamiokande on atmospheric neutrino and limits on matter instability. *Int.J.Mod.Phys.*, A18:3809–3819, 2003.

[58] Toshiyuki Toshito. Super-Kamiokande atmospheric neutrino results. 2001.

[59] K. Abe et al. Precise Measurement of the Neutrino Mixing Parameter θ_{23} from Muon Neutrino Disappearance in an Off-axis Beam. 2014.

[60] John N. Bahcall and Roger K. Ulrich. Solar Models, Neutrino Experiments and Helioseismology. *Rev.Mod.Phys.*, 60:297–372, 1988.

[61] John N. Bahcall. NEUTRINO ASTROPHYSICS. 1989.

[62] John N. Bahcall. Solar neutrinos. I: Theoretical. *Phys.Rev.Lett.*, 12:300–302, 1964.

[63] J. Boger et al. The Sudbury neutrino observatory. *Nucl.Instrum.Meth.*, A449:172–207, 2000.

[64] David Waller. Results from the Sudbury Neutrino Observatory. *eConf*, C040802:WET001, 2004.

[65] Q.R. Ahmad et al. Direct evidence for neutrino flavor transformation from neutral current interactions in the Sudbury Neutrino Observatory. *Phys.Rev.Lett.*, 89:011301, 2002.

[66] J. Farine. Measurement of the rate of nu/e + d –gt; p + p + e- interactions produced by B-8 solar neutrinos at the Sudbury Neutrino Observatory. *Phys.Atom.Nucl.*, 65:2147–2155, 2002.

[67] B. Aharmim et al. Measurement of the Cosmic Ray and Neutrino-Induced Muon Flux at the Sudbury Neutrino Observatory. *Phys.Rev.*, D80:012001, 2009.

[68] B. Aharmim et al. Measurement of the ν_e and Total ^{8}B Solar Neutrino Fluxes with the Sudbury Neutrino Observatory Phase-III Data Set. *Phys.Rev.*, C87:015502, 2013.

[69] L. Wolfenstein. Neutrino Oscillations in Matter. *Phys.Rev.*, D17:2369–2374, 1978.

[70] S.P. Mikheev and A. Yu. Smirnov. Resonant amplification of neutrino oscillations in matter and solar neutrino spectroscopy. *Nuovo Cim.*, C9:17–26, 1986.

[71] K. Abe et al. Solar neutrino results in Super-Kamiokande-III. *Phys.Rev.*, D83:052010, 2011.

[72] T. Araki et al. Measurement of neutrino oscillation with KamLAND: Evidence of spectral distortion. *Phys.Rev.Lett.*, 94:081801, 2005.

[73] K. Eguchi et al. First results from KamLAND: Evidence for reactor anti-neutrino disappearance. *Phys.Rev.Lett.*, 90:021802, 2003.

[74] P. Vogel, G.K. Schenter, F.M. Mann, and R.E. Schenter. Reactor Anti-neutrino Spectra and Their Application to Anti-neutrino Induced Reactions. 2. *Phys.Rev.*, C24:1543–1553, 1981.

[75] M.-C. Chu. Precise measurement of θ_{13} at Daya Bay. 2008.

[76] H.R. Band, R. Brown, J. Cherwinka, J. Cao, Y. Chang, et al. Acrylic Target Vessels for a High-Precision Measurement of theta13 with the Daya Bay Antineutrino Detectors. *JINST*, 7:P06004, 2012.

[77] Yayun Ding, Jinchang Liu, Zhimin Wang, Zhiyong Zhang, Pengju Zhou, et al. A new gadolinium-loaded liquid scintillator for reactor neutrino detection. *Nucl.Instrum.Meth.*, A584:238–243, 2008.

[78] Xinheng Guo et al. A Precision measurement of the neutrino mixing angle θ_{13} using reactor antineutrinos at Daya-Bay. 2007.

[79] Ji-Lei Xu, Meng-Yun Guan, Chang-Gen Yang, Yi-Fang Wang, Jia-Wen Zhang, et al. Design and preliminary test results of Daya Bay RPC modules. *Chin.Phys.*, C35:844–850, 2011.

[80] F.P. An et al. Improved Measurement of Electron Antineutrino Disappearance at Daya Bay. *Chin.Phys.*, C37:011001, 2013.

[81] J.K. Ahn et al. Observation of Reactor Electron Antineutrino Disappearance in the RENO Experiment. *Phys.Rev.Lett.*, 108:191802, 2012.

[82] Y. Abe et al. Indication for the disappearance of reactor electron antineutrinos in the Double Chooz experiment. *Phys.Rev.Lett.*, 108:131801, 2012.

[83] J.K. Ahn et al. RENO: An Experiment for Neutrino Oscillation Parameter θ_{13} Using Reactor Neutrinos at Yonggwang. 2010.

[84] Y. Abe et al. Reactor electron antineutrino disappearance in the Double Chooz experiment. *Phys.Rev.*, D86:052008, 2012.

[85] J.A. Formaggio and C.J. Martoff. Backgrounds to sensitive experiments underground. *Ann.Rev.Nucl.Part.Sci.*, 54:361–412, 2004.

[86] J. Beringer et al. Review of Particle Physics (RPP). *Phys.Rev.*, D86:010001, 2012.

[87] Steven Weinberg. A model of leptons. *Phys. Rev. Lett.*, 19:1264–1266, Nov 1967. http://link.aps.org/doi/10.1103/PhysRevLett.19.1264.

[88] L. Michel. Interaction between four half spin particles and the decay of the mu meson. *Proc.Phys.Soc.*, A63:514–531, 1950.

[89] T. Aaltonen et al. Precise measurement of the W-boson mass with the CDF II detector. *Phys.Rev.Lett.*, 108:151803, 2012.

[90] Bruno Rossi and Kenneth Greisen. Cosmic-ray theory. *Rev. Mod. Phys.*, 13:240–309, Oct 1941. http://link.aps.org/doi/10.1103/RevModPhys.13.240.

[91] V. F. Hess. ber Beobachtungen der durchdringenden Strahlung bei sieben Freiballonfahrten. *Physikalische Zeitschrift*, 13:1084–1091, November 1912.

[92] nobelprize.org. Nobel Prize in Physics 1936 - Presentation Speech, May 2014. http://www.nobelprize.org/nobel_prizes/physics/laureates/1936/press.html.

[93] P.K.F. Grieder. Cosmic rays at earth: Researcher's reference, manual and data book. 2001.

[94] J. J. Engelmann, P. Ferrando, A. Soutoul, P. Goret, and E. Juliusson. Charge composition and energy spectra of cosmic-ray nuclei for elements from Be to NI - Results from HEAO-3-C2. , 233:96–111, July 1990.

[95] K.M. Schure, A.R. Bell, L.O'C Drury, and A.M. Bykov. Diffusive shock acceleration and magnetic field amplification. *Space Sci.Rev.*, 173:491–519, 2012.

[96] Enrico Fermi. On the Origin of the Cosmic Radiation. *Phys.Rev.*, 75:1169–1174, 1949.

[97] Ronald J. Allen. A Demonstration of the Magnetic Mirror Effect. *American Journal of Physics*, 30:867–869, 1962.

[98] J. Perez-Rios and A. S. Sanz. How does a magnetic trap work? *American Journal of Physics*, 81:836–843, 2013.

[99] M. Ackermann et al. Detection of the Characteristic Pion-Decay Signature in Supernova Remnants. *Science*, 339:807, 2013.

[100] V. K. Babaian and L. I. Dorman. The nonlinear theory of cosmic ray modulation by solar wind. I - Spherically-symmetrical model. II - The focusing effect in the asymmetric model. *International Cosmic Ray Conference*, 3:107–118, 1977.

[101] M. Schwabe. Sonnenbeobachtungen im Jahre 1843. Von Herrn Hofrath Schwabe in Dessau. *Astronomische Nachrichten*, 21:233, February 1844.

[102] W.R. Webber, F.B. McDonald, A.C. Cummings, E.C. Stone, B. Heikkila, et al. Sudden Intensity Increases and Radial Gradient Changes of Cosmic Ray MeV Electrons and Protons Observed at Voyager 1 beyond 111 AU in the Heliosheath. 2011.

[103] Bruno Rossi. Directional measurements on the cosmic rays near the geomagnetic equator. *Phys. Rev.*, 45:212–214, Feb 1934. http://link.aps.org/doi/10.1103/PhysRev.45.212.

[104] M.V.S. Rao and B.V. Sreekantan. Extensive air showers. 1998.

[105] V.A. Kudryavtsev, N.J.C. Spooner, and J.E. McMillan. Simulations of muon induced neutron flux at large depths underground. *Nucl.Instrum.Meth.*, A505:688–698, 2003.

[106] Y. Ashie et al. Evidence for an oscillatory signature in atmospheric neutrino oscillation. *Phys.Rev.Lett.*, 93:101801, 2004.

[107] C. Adams et al. Scientific Opportunities with the Long-Baseline Neutrino Experiment. 2013.

[108] Haruki Nishino. Search for proton decays via p —gt; e+ pi0 and p —gt; mu+ pi0 in Super-Kamiokande. *J.Phys.Conf.Ser.*, 136:042018, 2008.

[109] J. Esterline et al. The Majorana experiment. *Nucl.Phys.Proc.Suppl.*, 221:364, 2011.

[110] D.S. Akerib et al. First results from the LUX dark matter experiment at the Sanford Underground Research Facility. *Phys.Rev.Lett.*, 112:091303, 2014.

[111] Qingmin Zhang, Yifang Wang, Jiawen Zhang, Jun Cao, Talent Kwok, et al. An underground cosmic-ray detector made of RPC. *Nucl.Instrum.Meth.*, A583:278–284, 2007.

[112] F. Ardellier et al. Double Chooz: A Search for the neutrino mixing angle theta(13). 2006.

[113] Lindley Winslow. The KamLAND muon tracking system. *Nucl.Phys.Proc.Suppl.*, 221:414, 2011.

[114] J.G. Learned. Underground muons in super-kamiokande. 1997.

[115] M. Cribier, B. Pichard, J. Rich, J.P. Soirat, M. Spiro, et al. The muon induced background in the GALLEX experiment. *Astropart.Phys.*, 6:129–141, 1999.

[116] G. Bellini et al. Cosmogenic Backgrounds in Borexino at 3800 m water-equivalent depth. *JCAP*, 1308:049, 2013.

[117] A. Fujii, M. Morita, and H. Ohtsubo. Muon capture and nuclear structure. 1968.

[118] D.F. Measday. The nuclear physics of muon capture. *Phys.Rept.*, 354:243–409, 2001.

[119] A. Yushkov, M. Ambrosio, C. Aramo, D. D'Urso, L. Valore, et al. Precise determination of muon and electromagnetic shower contents from shower universality property. *Phys.Rev.*, D81:123004, 2010.

[120] Leonid B. Bezrukov and E.V. Bugaev. Inelastic scattering of high energy muons on nuclei. 1981.

[121] P. Kiraly, M.G. Thompson, and A.W. Wolfendale. Cosmic ray showers produced by muon bremsstrahlung. *J.Phys.*, A4:367–376, 1971.

[122] G. C. Baldwin and G. S. Klaiber. Photo-fission in heavy elements. *Phys. Rev.*, 71:3–10, Jan 1947. http://link.aps.org/doi/10.1103/PhysRev.71.3.

[123] Jean Delorme, Magda Ericson, Torleif Erik Oskar Ericson, and Petr Vogel. Pion and neutron production by cosmic ray muons underground. *Phys.Rev.*, C52:2222–2230, 1995.

[124] J.S. Levinger. The High-energy nuclear photoeffect. *Phys.Rev.*, 84:43–51, 1951.

[125] P.A. Cerenkov. Visible luminescence of pure fluids induced by gamma rays. *Dokl.Akad.Nauk Ser.Fiz.*, 2:451–454, 1934.

[126] Shirley Weishi Li and John F. Beacom. First calculation of cosmic-ray muon spallation backgrounds for MeV astrophysical neutrino signals in Super-Kamiokande. *Phys.Rev.*, C89:045801, 2014.

[127] S. Abe et al. Production of Radioactive Isotopes through Cosmic Muon Spallation in KamLAND. *Phys.Rev.*, C81:025807, 2010.

[128] D. Reyna. A Simple parameterization of the cosmic-ray muon momentum spectra at the surface as a function of zenith angle. 2006.

[129] E.V. Bugaev, A. Misaki, Vadim A. Naumov, T.S. Sinegovskaya, S.I. Sinegovsky, et al. Atmospheric muon flux at sea level, underground and underwater. *Phys.Rev.*, D58:054001, 1998.

[130] P. Antonioli, C. Ghetti, E.V. Korolkova, V.A. Kudryavtsev, and G. Sartorelli. A Three-dimensional code for muon propagation through the rock: Music. *Astropart.Phys.*, 7:357–368, 1997.

[131] H. Bethe. Zur Theorie des Durchgangs schneller Korpuskularstrahlen durch Materie. *Ann. Phys.*, 397:325–400, 1930.

[132] D. F. Maune, C. H. Lloyd, and G. C. Guenther. *DEM User Applications*, pages 367–394. American Society for Photogrammetry and Remote Sensing, Maryland, 2001.

[133] Joseph F. Dracup. Geodetic Surveying 1940-1990. 1995.

[134] S. Dutch. Converting utm to latitude and longitude (or vice versa), September 2003. http://www.uwgb.edu/dutchs/usefuldata/utmformulas.htm.

[135] C. Mariani. DUSEL (Deep Underground Science and Engineering Laboratory) and LBNE (Long Baseline Neutrino Experiment). *Nucl.Phys.Proc.Suppl.*, 217:344–346, 2011.

[136] J. Heise. The Sanford Laboratory at Homestake and the Path to DUSEL. *Nucl.Phys.Proc.Suppl.*, 229-232:526, 2012.

[137] N. Abgrall, E. Aguayo, F.T. Avignone, A.S. Barabash, F.E. Bertrand, et al. A search for bremsstrahlung solar axions using the Majorana low-background BEGe detector at Kimballton (MALBEK). 2014.

[138] S. MacMullin, G.K. Giovanetti, M.P. Green, R. Henning, R. Holmes, et al. Measurement of airborne fission products in Chapel Hill, NC, USA from the Fukushima Dai-ishi reactor accident. *J.Environ.Radioact.*, 112:165–170, 2012.

[139] P. Finnerty, S. MacMullin, H.O. Back, R. Henning, A. Long, et al. Low-Background gamma counting at the Kimballton Underground Research Facility. *Nucl.Instrum.Meth.*, A642:65–69, 2011.

[140] UNLP Electronics Lab. Manufacturing of Polystyrene Based Scintillators. http://www2.fisica.unlp.edu.ar/ veiga/scintillators.html.

[141] Team Neutrino (Double Chooz collaboration). OV Electronics and Test (In Preparation).

[142] Hamamatsu Photonics. Photomultiplier Tube Assembly H8804. http://www.hamamatsu.com/resources/pdf/etd/H8804_TPMH1333E01.pdf.

[143] P. Barrillon et al. MAROC2 Data Sheet. http://elec-in2p3.lal.in2p3.fr/micro/maroc.

[144] J. F. Ziegler. Terrestrial Cosmic Rays, 1996. http://domino.research.ibm.com/tchjr/journalindex.nsf.

[145] G. E. Manger. Porosity and Bulk Density of Sedimentary Rocks. *Geological Survey Bulletin 1144-E*, 1963. http://pubs.usgs.gov/bul/1144e/report.pdf.

[146] M. Ambrosio et al. Vertical muon intensity measured with MACRO at the Gran Sasso Laboratory. *Phys.Rev.*, D52:3793–3802, 1995.